Study of the Θ^+ via $\gamma d \to K^+K^-pn$ reaction with high statistics data at SPring-8/LEPS

Yuji Kato

Department of physics
Osaka University

March, 2012

Study of the Θ^+ via $\gamma d \to K^+K^-pn$ reaction with high statistics data at SPring-8/LEPS

（SPring-8/LEPSにおける、高統計データでの $\gamma d \to K^+K^-pn$ を用いた Θ^+ 粒子の研究）

Yuji Kato

Abstract

We have searched for the Θ^+ in $\gamma d \to K^+K^-$ reaction at the SPring-8/LEPS facility. The high energy photon beam with E_γ = 1.5-2.4 GeV has been produced by laser backward Compton scattering from 8 GeV electons in the strage ring of SPring-8. In 2002-2003, an experiment with liquid deuterium target was performed and a narrow peak corresponds to the Θ^+ with a statistical significance of 5.1 σ was observed. To confirm the result, an experiment with almost the same detector setup was performed in 2006-2007. For this experiment, a two laser injection system was developed to increase the beam intensity, and the tagger rate of 2 Mcps at the maximum was achieved. The data with about 2.6 times more statistics has been collected. In the analysis of the new data, the blind analysis technique, which was not used in the analysis of previous data, is used to remove the artificial bias. The $M(nK^+)$ distribution for the new data does not show a strong narrow peak structure. The statistical significance of the peak is 1.6-1.9 σ depending on the fitting range. The peak position is 1513 $\pm$ 5 MeV/c^2, which is lower than the result of the previous data (1524 $\pm$ 2 MeV/c^2). To check the consistency between two data sets, the χ^2 of the fitting in the space of mean and height of the Gaussian is investigated. At the closest point, the χ^2 of the fittings are deviated almost 3 σ from both of data sets. Previous result is not reproduced. Summed data shows a statistical significance of 3.6-3.8 σ with a peak position of 1518, 1519 $\pm$2.0 MeV/c^2 depending on the tuning of the momentum scale factor and fitting range. For the previous data, the peak structure is seen even when we select the quasi-free KK production from proton events by using pulse height information of the trigger counter, which suggest that part of the peak structure seen in the previous data comes from statistical fluctuation. Furthermore, after rejecting the KKp events, a enhancement at the signal region is seen for the new data and the summed data.

Acknowledgments

I would like to express my sincere gratitude to my supervisor, Prof. Takashi Nakano to give me an opportunity to work on an exciting subject and his continuous encouragement

I would like to gratefully acknowledge Prof. Masaru Yosoi's help. He taught me a lot of experimental techniques. He also give me an opportunity to work on the new TPC experiment. I really appreciate Dr. T. Hotta's help to taught me a lot of experimental techniques especially about the tagging counter. He also prepared very nice computer system. I would like to express my acknowledge to Dr. N. Muramatsu who taught me a lot of analysis techniques and gave me an opportunity to work on the development of the laser system. I would like to express my gratitude to M. Sumihama who supported my analysis work. I thank Prof. H. Fujimura and Dr. M. Niiyama for giving me an opportunity to work on the TPC experiment. I thank Dr Y. Ohashi for his dedicated works to maintain the LEPS beam-line. I thank Dr S. Date for his works on the analysis of electron beam conditions.

I would like to thank my collaborators, Mrs D.S. Ahn, Prof. W.C. Chang, Prof. M. Fujiwara, Prof. K. Hicks, Dr. K. Horie, Dr. T. Ishikawa, Prof. H. Kawai, Dr. T. Matsumura, Dr. T. Mibe, Prof. M. Nomachi, Prof H. Shimizu, Dr. Y. Sugaya, Dr. T. Yorita, Dr. M.Uchida, Dr. T.Ohta, Mr Y. Nakatsugawa, Dr. Y. Morino, Dr. Kohri, Dr. J.Y. Chen, Dr. S.H. Hwang, Mr Y. Kon, Mr M. Oka, Dr. C.J. Yoon, Dr. K.Kino, Mr Y. Nozawa, Ms N. Tomida, and Y. Kasamatsu. Without their helps, this work can not be completed. I especially appreciate Dr. M. Miyabe and Mr T. Sawada for their great encouragement.

I would like to thank continuous encouragement and support from my family, Kazuaki Kato, Tomiko Kato, Issei Kato, Satomi Kato, Akari Kato, and Ryo Kato.

Contents

Chapter 1

Introduction

1.1 The pentaquark baryon, Θ^+

In 2003, the LEPS collaboration reported an evidence for a baryon with a strangeness quantum number S=+1 and charge +1, now called Θ^+, in $\gamma C \to K^+K^-X$ reactions [1]. This work was motivated by theoretical prediction of narrow width and low mass for the pentaquark state using chiral quark soliton model by Diakonov et al. [2]. Figure 1.1 shows the Fermi-motion corrected missing mass of K^- taken from [1]. A narrow peak around 1.54 GeV/c^2, which corresponds to the Θ^+, is seen. As the strange quantum number of the Θ^+ is +1, Θ^+ contains $\bar{s}$ quark. To conserve the baryon number, minimal quark content of the Θ^+ is $uudd\bar{s}$. Therefore, the Θ^+ is a genuine pentaquark state. Since the first report by LEPS, the studies for the Θ^+ has been widely performed from both experimentally and theoretically. The Θ^+ has been attracted attention not only because it is a new type of baryon, but also it has two features, namely a low mass and a narrow width. The mass of the Θ^+ is measured to be 1520-1550 MeV/c^2. A naive consideration from the constituent quark model tells us that the sum of the mass of constituent quark is about 1900 MeV when $m_{u,d}$ is assumed to be 350 MeV/c^2 and m_s is assumed to be 500 MeV/c^2. This is much larger than the measured value. The width of the Θ^+ is measured to be at least less than 1 MeV/c^2 from several experiments as written in later section. The value is too narrow to be explained by current knowledge of the hadron physics. Therefore, the Θ^+ has a possibility to bring us new knowledge about the hadron physics. At an early stage, the LEPS result had been supported by several experiments. However, the situation became soon controversial because a number of experiments with a high statistics and a good mass resolution reported negative results. Therefore, the most important work for experimental side is to confirm whether the Θ^+ exists or not. From the next section, the overview of the studies for the Θ^+, which is the background of the aim of this thesis, is presented.

1.2 Theoretical works for the Θ^+

As written in the previous section, it is a challenge for theorists to explain the low mass and the narrow width of the Θ^+. Huang and Zhang calculated the mass of the Θ^+ by using conventional constituent quark model [3]. They tried several combinations of spin and parity for the Θ^+. The states of $1/2^-$ in which all the quarks and anti-quark are in s-wave is found

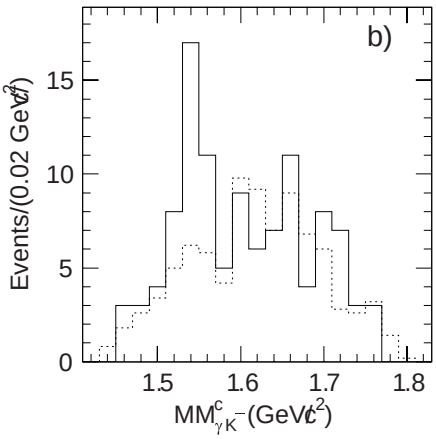

Figure 1.1: The Fermi-motion corrected missing mass of K^- taken from [1]. Solid histogram is the event from CH2. The dotted histogram is background spectrum obtained by the events from the liquid hydrogen target.

to give the lowest mass. However, the calculated mass was about 150 - 300 MeV higher than the experimental value. Furthermore, they also remarked that it is very difficult to explain the narrow width of the Θ^+ by conventional quark model because there exists KN fall-apart decay. Their studies shows that something new is necessary to explain the features of the Θ^+. In this section, some theoretical models which tried to explain the features of the Θ^+ are introduced.

Before the first evidence of the Θ^+ reported by LEPS collaboration, Diakonov et al. predicted that the mass of the Θ^+ with spin parity of $1/2^+$ was around 1530 MeV/c^2 and the width was less than 15 MeV/c^2 by using the chiral quark soliton model [2]. In the chiral quark soliton model, a baryon is viewed as a object filled by mean field of the $q\bar{q}$ pairs, which is valid in the large N_c limit. They explained the narrow width of the Θ^+ as the cancellation of leading order and two subsequent orders in $1/N_c$ expansion of the amplitude.

In [4], Diakonov also argued that the existence of the Θ^+ can be verified from three baryon resonances, $N(1535)$, $N(1440)$, and $\Lambda(1405)$ by using mean field approach. He explained the $N(1440)$ and the $\Lambda(1405)$ as a quark quark excitation in the mean field: $\Lambda(1405)$ as a $1/2^-$ excitation of the s quark and N(1440) as a 0^+ (or 1^+) excitation of u,d quarks. The existence of the excited $1/2^-$ state implies that the state can be also filled by a s quark in the s-quark shell. The state is identified as $N(1535, 1/2^-)$, which decays dominantly into ηN. On the other hand, the Θ^+ is identified as the excitation of the s quark in the s-quark shell into the 0^+ (or 1^+) state of the u,d quarks. These arguments are illustrated in Fig. 1.2, which is taken from [4]. The idea is similar to the Gamov-Teller resonance, which is familiar in the nuclear physics. The Gamov-Teller resonance changes both isospin and total spin simultaneously. In this idea, the isospin corresponds to the strangeness and the total spin corresponds to the one quark excitation. The mass of the Θ^+ can be calculated as 1440+1535-1405 = 1570 MeV/c^2, which is rather close to the measured value.

Jaffe and Wilczek tried to explain the structure of the Θ^+ as two spin zero, color and flavor $\bar{3}$ diquarks ($2 \times [ud]$) and one anti-quark ($\bar{s}$) [5]. The two diquarks must be combined into color 3 to compose color singlet state with an anti-quark. Therefore, the color part of two diquarks

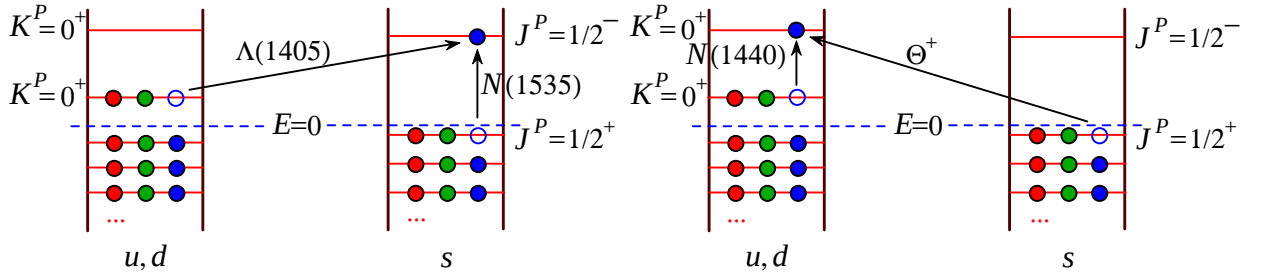

Figure 1.2: Left: One quark excitation corresponds to $\Lambda(1405)$ and $N(1535)$. Right: One quark excitation corresponds to $N(1440)$ and Θ^+.

are antisymmetric. Because a diquark is a Bose particle, the flavor and orbital part of two diquarks must be antisymmetric. The flavor part is symmetric because two diquarks have the same quark content. Therefore, the orbital part must be antisymmetric. Thus, they assigned the spin and parity of the Θ^+ as $1/2^+$ (spin is selected to be $1/2$ to make the mass low). The low mass of the Θ^+ is qualitatively explained by an attractive interaction between two quarks in the color $\bar{3}$. They remarked that the narrow width of the Θ^+ may be explained by relatively weak coupling of the K^+n state to the $(2\times[ud]\bar{s})$ state because the color, spin and spatial wave functions are different. The two diquarks with flavor symmetric and one anti-quark form a $8\bigoplus\bar{10}$ multiplet while only the $\bar{10}$ multiplet exists for chiral soliton model. The quark contents of the $8\bigoplus\bar{10}$ multiplet is shown in the left panel of the Fig. 1.3. They assigned the Roper resonance, N(1440) as $2\times[ud]\bar{d}$ of this multiplet. Furthermore, they predicted that the Ξ state is lighter than Σ state. The comparison of mass relation between the diquark model and the chiral soliton model is shown in the right panel of Fig. 1.3.

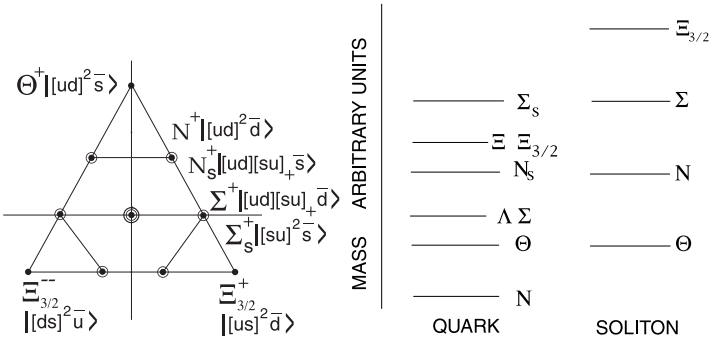

Figure 1.3: Left: The quark content of the $8\bigoplus\bar{10}$ multiplet taken from [5]. Right: Relative masses of $8\bigoplus\bar{10}$ multiplet compared with chiral soliton model taken from [5].

Kishimoto and Sato tried to explain the Θ^+ as a bound state of the $K\pi N$ [6]. The mass of the $K\pi N$ system is roughly 30 MeV/c^2 larger than that of the Θ^+. They pointed out that no precise data for the low energy πK scattering exists and assumed that a bound state is realized by the attractive interaction of the πK system. This assumption leads to the further prediction that there exists a bound state of the πK system (they called the bound state as X). They assumed that three particles are in an s-wave to realize the lowest energy and assigned

the spin-parity of the Θ^+ to be $1/2^+$. A nice point of the three body bound state is that the narrow width of the Θ^+ can be naturally explained. Since the Θ^+ decays into KN, the pion has to be absorbed. To conserve the spin and parity, both πN system and the Kaon with respect to πN system must be excited to the p-state simultaneously. This means that the Θ^+ has a d-wave component. However, such component is thought to be small. Rough estimation shows that the width is approximately 1 MeV/c^2.

Hyodo et al. studied the S-wave scattering of the baryon and meson system in exotic channels using chiral unitary approaches [7]. In this model, the $\Lambda(1405)$ is explained as dynamically generated state by the meson-baryon scattering with low energy interactions governed by the chiral symmetry [8]. They showed that the interactions for most of the exotic channels are repulsive, and the strength of the attractive interaction is not strong enough to generate an exotic states.

1.3 Experiments

After the first evidence of the Θ^+, considerable numbers of experiments are performed to confirm the existence of Θ^+. In this section, current status of experimental studies are reviewed except for photo-production experiments. Because the photo-production experiments are subject of this thesis, they are described in section 1.4 in detail. A review paper for the relatively old experimental search of the Θ^+ can be found in [9].

1.3.1 The formation experiment, $K^+n \to \Theta^+$

The $K^+n \to \Theta^+$ reaction is particularly important for the study of the Θ^+. Because the reaction is a reverse process of the decay of the Θ^+, the width of the Θ^+ can be determined from its production cross section. In general, the production cross section σ is determined from the decay width, Γ, and its branching ratios for initial and final channels, B_i and B_f, as

$$\sigma = B_i B_f \frac{\pi\Gamma}{2}\sigma_0. \tag{1.1}$$

The σ_0 is given as

$$\sigma_0 = \frac{2J+1}{(2s_1+1)(2s_2+1)}\frac{4\pi}{k^2}, \tag{1.2}$$

where J, s_1 and s_2 is the total spin of resonant particle, decay particles, respectively, and k is the CM momentum. For the $K^+n \to \Theta^+$ reaction, the σ_0 is 68 mb by taking the mass of Θ^+ to be $1540MeV/c^2$ and assuming that total spin (J) of the Θ^+ is 1/2. The branching ratio B_i = B_f is 1/2 which is valid for either I = 0 or I = 1. Finally, equation 1.1 can be written as

$$\sigma = 26.8\,(mb/MeV)\,\Gamma. \tag{1.3}$$

The DIANA collaboration at ITEP searched for the Θ^+ using K^+ beam and a bubble chamber filled with liquid Xenon via the charge exchange reaction, $K^+Xe \to K^0_s pXe'$. They continuously worked for this subject to improve the statistics and analysis and they reported three papers [10] [11] [14]. In [10], they analyzed 1112 events of the reaction $K^+Xe \to K^0_s pXe'$. They applied the cut condition $\theta_p < 100^0$ and $\theta_K < 100^0$ and $cos\Phi_{pK} < 0$, where θ_p and θ_K are

the emission angle of the proton and K^0 with respect to the K^+ direction in the laboratory frame and in order to reject the events which p or K^0_s is $cos\Phi_{pK}$ is the azimuthal angle between the proton and K^0, in order to reject the events which p or K^0 is re-scattered in nucleus. The pK^0_s invariant mass distribution showed a narrow peak at $1539 \pm 2.0\ MeV/c^2$. The width of the peak was consistent with that expected from experimental resolution. The statistical significance of the peak was 4.4σ from $S/\sqrt{B}$. The width of the Θ^+ was obtained from ratio of resonant and non-resonant events at the peak [12]. They interpolated the old result of K^+d charge reaction cross section [13] and obtained the cross section of non-resonant charge exchange reaction at the peak. The decay width of the Θ^+ was obtained to be $0.9 \pm 0.3 MeV/c^2$. In [12], they also analyzed old K^+d scattering and they obtained the upper limit for the width of the Θ^+ to be 1-4 MeV/c^2. In [11], they increased the statistics from 1112 to 2131 events. They refined the cut conditions to reject the re-scattered events by using the information of beam momentum and effective target mass information. The pK^0_s invariant mass distribution again showed a narrow peak at $1537 \pm 2\ MeV/c^2$ whose width is consistent with experimental resolution. The statistical significance of the peak was 7.3, 5.3, 4.3 σ from $S/\sqrt{B}$, $S/\sqrt{S+B}$, $S/\sqrt{S+2B}$, respectively. They also refined the way to measure the decay width. In [10], they assumed that the rejection factors of the cut to reject the re-scattering events were the same for both resonant and non-resonant process. However, because the width of the Θ^+ is narrow (the life time is long), almost of the Θ^+ decay outside the nucleus. They obtained the rejection factor of cut condition for non-resonant events by Monte-Carlo simulation. The decay width was obtained to be $0.36 \pm 0.11\ MeV/c^2$. In [14], they further refined the cut condition to reject re-scattered events and increased the statistics by 11%. The pK^0_s invariant mass distribution again showed a narrow peak at $1537 \pm 2\ MeV/c^2$ whose width is consistent with experimental resolution. The statistical significance of the peak was 8.0, 6.0 σ from $S/\sqrt{B}$, $S/\sqrt{S+B}$, respectively. The decay width was obtained to be $0.39 \pm 0.10\ MeV/c^2$.

The Belle collaboration also studied the $K^+n \to \Theta^+$ reaction using secondary pK^0_s pairs which were produced by the interaction between materials of the inner part of the detector and particles produced in e^+e^- annihilation [15]. Since they did not reconstruct a projectile, it was not possible to identify the charge exchange reaction event by event. They obtained the contribution of the charge exchange reaction in a pK^0_s sample from the decay chain of $D^{*-} \to \bar{D}^0\pi^-$, $\bar{D}^0 \to K^+\pi^-$ for events where a K^+ interacts elastically in the detector material. They did not observe an evidence of the Θ^+ and gave the upper limit (90% CL) for the width of the Θ^+ to be $0.64\ MeV/c^2$, which is barely consistent with the result obtained by DIANA. In [15], Belle collaboration also reported a negative result of the Θ^+ search in the production channel. This part will be explained in section 1.3.3.

Summary of the formation experiments is given in table 1.3.1. Both DIANA and Belle collaboration measured the width for the Θ^+ to be less than 1 MeV/c^2.

Table 1.1: Summary of the formation experiments.

Reference	Group	Reaction	Result	Limit	Mass(MeV)
[14]	DIANA	$K^+Xe \to K^0pXe'$	positive	-	1537± 2.0
[15]	Belle	$K^+A \to K^0pA'$	negative	Width< 0.64 MeV/c^2	–

1.3.2 High energy experiment

There are several positive evidences for the Θ^+ in high energy experiments [16]-[22]. Among them, the evidence reported by the SVD collaboration [22] is very strong. The study in [22] is an improved study of [21]. In [21], they searched for Θ^+ via $pA \to K^0_S pX$ reaction using the proton beam with a momentum of 70 GeV/c at IHEP. They rejected the events which have more than five charged tracks to reduce the combinatorial background. They also applied two kinematic cut conditions, $cos(pK^0) < 0$ and $P_{K^0_s} \leq P_p$. The former cut was applied to reduce the background from misidentified proton and latter cut was applied to reduce the background from Σ^{*+}. After applying the cuts , the pK^0_s invariant distribution showed a peak at $1526 \pm 3(stat) \pm 3(syst)$. In [22], they used new algorithms for the reconstruction of K^0_s tracks which decay inside the vertex detector. The number of K^0_s tracks was increased by a factor of 3-4 by new algorithms. After applying the cut conditions $3\,GeV < P_{proton} < 10\,GeV$ and $4 < N_{tracks} <= 7$, the pK^0_s invariant mass distribution again showed a peak. They also newly analyzed a data set in which a K^0_s decays outside the vertex detector. The pK^0_s invariant mass distribution for this data set again showed a peak at $1523.6 \pm 3.1 MeV/c^2$. They estimated the statistical significance for combined result to be 8.7, 8.0, 5.9 σ from $S/\sqrt{B}$, $S/\sqrt{S+B}$, $S/\sqrt{S+2B}$, respectively. Figure 1.4 shows the pK^0_s invariant mass distribution for two data sets taken from [22].

There are a number of high energy experiments which report negative results for the Θ^+ search [23]-[36]. Many of them are with high statistics and a good mass resolution and clearly observe a large number of well known resonances. The ratio of the $\Lambda(1520)$ and Θ^+ cross section (R_{Λ^*}) is often used for the upper limit because $\Lambda(1520)$ is narrow and easily reconstructed, and the mass of the $\Lambda(1520)$ is close to that of the Θ^+. In many experiments, R_{Λ^*} is set to be less than a few percent.

The SPHINX experiment [27], which was performed with the same beam with that of SVD [22], reported a negative result. However, the SVD experiment found the Θ^+ in very small x_F region, while SPHINX does not have the acceptance in the region.

Summary of the high energy experiments is given in table 1.2.

1.3.3 Low energy hadron beam experiment

An experiment which uses a low energy hadron beam is a good probe to study the Θ^+ from two reasons. One is that the cross section is high for strong interaction process. The other is that the experiment is suitable to study the production mechanism because the process is rather simple for low energy region, where minimal number of particles are produced in the final state.

The KEK E522 collaboration searched for the Θ^+ via $\pi^- p \to K^- X$ using the 1.87 and 1.92 GeV/c π^- beam at the KEK-PS [38]. The K^- missing mass distribution showed a small bump at 1530.6 MeV/c^2 for the 1.92 GeV/c π^- beam while no structure was seen in 1.87 GeV/c π^- beam. However, the statistical significance of the bump was 2.5-2.7 σ, which is not sufficient to claim the bump as a evidence of the Θ^+. The upper limit for the production cross section was set to be 1.8, 3.9 μb for the beam momentum of 1.87, 1.92 GeV/c, respectively. It should be noted that J-PARC E19 collaboration performed an experiment to search for Θ^+ with the same reaction and beam momentum with an improved statistics and an improved

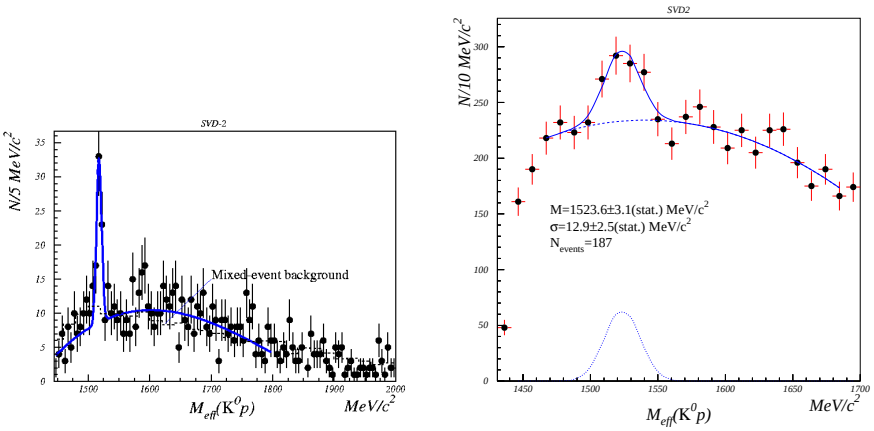

Figure 1.4: The pK_s^0 invariant mass distribution taken from [22]. Left plot is for the events which K_s^0 decays inside the vertex detector. Right plot is for the events which K_s^0 decays outside the vertex detector.

mass resolution. Although the result has not been published yet, they presented a negative result in several places.

The KEK E559 collaboration searched for the Θ^+ via $K^+p \to \pi^+X$ using the 1.2 GeV/c K^+ beam at the KEK-PS [37]. The π^+ missing mass distribution shows no peak structure. The upper limit for the production cross section $d\sigma/d\Omega$ was set to be 3.5 $\mu b/sr$.

The COSY-TOF collaboration searched for the Θ^+ via $pp \to \Sigma^+K^0p$ using 2.95 GeV/c proton beam and TOF detector [39]. The pK_s^0 invariant mass distribution showed a peak at 1530 $\pm$ MeV/c^2. They repeated the experiment with a higher statistics by a factor of 4-8 depends on the analysis method and with slightly higher beam momentum (3.059 GeV/c) [40]. Then, the pK_s^0 invariant mass distribution did not show any peak structure. They explained the inconsistency between two results as small fluctuation of the peak and underestimation of the background in the first result [39]. The upper limit for the production cross section was set to be $\sigma < 0.15\ \mu b$.

The theoretical study of these results will be discussed in section 1.4 together with the theoretical study of the photo-production experiment because they are closely related.

Belle collaboration reported the result of Θ^+ search via $\pi, K, pA \to K_s^0pX$ reaction using interaction between materials of the inner part of the detector and secondary particles produced from e^+e^- annihilation [15]. The momentum of the secondary particles are relatively low. For example, the averaged momentum of the Kaon is approximately 0.6 GeV/c. The pK_s^0 invariant mass distribution did not show any peak structure while the pK^- invariant mass showed a clear peak corresponds to $\Lambda(1520)$. The upper limit for the production cross section was set to be R_{Λ^*} <0.02. Summary of the low energy hadron beam experiments is given in table 1.3.3.

Table 1.2: Summary of the high energy experiments

Reference	Group	Reaction	Result	Limit	Mass(MeV)
[16]	νBC	$\nu A \to K^0_s pX$	positive	–	1533 ± 5
[17]	HERMES	$e^+ d \to K^0_S pX$	positive	–	1526 ± 3
[18]	ZEUS	$e^+ p \to K^0_S pX$	positive	–	1522 ± 3
[19]	JINR	$p(C_3H_8) \to K^0_s pX$	positive	–	1545 ± 12
[22]	SVD-2	$pA \to K^0_S pX$	positive	–	$1523 \pm 2 \pm 3$
[23]	BES	$e^+e^- \to J/\Psi \to \bar{\Theta}\Theta$	negative	$< 1.1 \times 10^{-5}$ B.R.	-
[24]	BaBar	$e^+e^- \to \Upsilon(4S) \to pK^0X$	negative	$< 1.0 \times 10^{-4}$ B.R.	-
[25]	Belle	$e^+e^- \to B^0\bar{B}^0 \to p\bar{p}K^0X$	negative	$< 2.3 \times 10^{-7}$ B.R.	-
[26]	HERA-B	$pA \to K^0_S pX$	negative	R_{Λ^*} <0.02	-
[27]	SPHINX	$pC \to \Theta^+ X$	negative	R_{Λ^*} <0.1	-
[28]	HyperCP	$\pi, K, pCu \to K^0_S pX$	negative	$< 0.3\%$ K^0p	-
[29]	CDF	$p\bar{p} \to K^0_S pX$	negative	R_{Λ^*} <0.03	-
[30]	FOCUS	$\gamma BeO \to K^0_S pX$	negative	R_{Λ^*} <0.02	-
[31]	PHENIX	$Au + Au \to K^- \bar{n} X$	negative	(not given)	-
[32]	ALEPH	$e^+e^- \to K^0_s pX$	negative	R_{Λ^*} <0.07	-
[33]	COMPASS	$\mu^+ A \to K^0_s pX$	negative	–	-
[34]	DELPHI	$e^+e^- \to K^0_s pX$	negative	R_{Λ^*} <0.5	-
[35]	E690	$pp \to K^0_s pX$	negative	R_{Λ^*} <0.005	-
[36]	LASS	$K^+p \to K^+n\pi^+$	negative	–	-
[34]	L3	$\gamma\gamma \to K^0_s pX$	negative	R_{Λ^*} <0.1	-

1.4 Photo-production

In this section, the photo-production of the Θ^+, which is the subject of this thesis, is discussed both from an experimental point of view and from a theoretical point of view.

1.4.1 Experiments at an early stage

As written in the beginning of this chapter, the first evidence of the Θ^+ was reported by LEPS collaboration in $\gamma C \to K^+K^-X$ reaction with a photon energy of 1.5-2.4 GeV [1]. A plastic scintillator, which was used as a trigger counter put just behind the liquid hydrogen target, was used as a target. The events originated from ϕ meson photo-production was eliminated

Table 1.3: Summary of the low energy hadron beam experiments.

Reference	Group	Reaction	Result	Limit	Mass(MeV)
[38]	KEK E522	$\pi^- p \to K^- X$	negative	$\sigma < 1.8\,\mu b, \sigma < 3.9\,\mu b$	–
[37]	KEK E559	$K^+p \to \pi^+X$	negative	$d\sigma/d\Omega < 3.5\,\mu b/sr$	–
[40]	COSY-TOF	$pp \to \Sigma^+K^0p$	negative	$\sigma < 0.15\,\mu b$	–
[15]	Belle	$\pi, K, pA \to K^0_s pX$	negative	R_{Λ^*} <0.02	-

by removing the events with the K^+K^- invariant mass from 1.0 to 1.04 GeV/c^2. About 85% of the events were removed by this cut. The simple missing mass of K^- assuming that the target is a neutron at rest ($MM_{\gamma K^-}$) did not give a good mass resolution because of the Fermi motion of the nucleons inside the nuclei. The Fermi-motion corrected missing mass ($MM^c_{\gamma K^-}$) was given as

$$MM^c_{\gamma K^-} = MM_{\gamma K^-} - MM_{\gamma K^+ K^-} + Mn, \tag{1.4}$$

where $MM^c_{\gamma K^-}$ is the Fermi motion corrected missing mass of K^-, $MM_{\gamma K^-}$ is the missing mass of K^- assuming that the target is a neutron at rest, $MM_{\gamma K^+ K^-}$ is the missing mass of the K^+ and K^- assuming that the target is a neutron at rest, Mn is neutron mass, respectively. The validity of the correction was checked by $\gamma C \to K^+\Sigma^- X \to K^+\pi^- nX$ reaction with a detection of K^+ and π^-. The $MM^c_{\gamma K^-}$ showed a narrow peak at $1.54 \pm 0.01\, GeV/c^2$.

Soon after the first evidence by the LEPS collaboration, SAPHIR collaboration at ELSA and CLAS collaboration at Jlab reported positive results of the Θ^+ search. The SAPHIR collaboration searched for the Θ^+ in $\gamma p \to nK^+K^0_s$ reaction with a photon energy of from production threshold to 2.8 GeV [41]. They selected the forward going K^0_s by a cut condition $cos\theta_{K^0_s} > 0.5$. After the cut, nK^+ invariant mass showed a narrow peak at $1540 \pm 4 \pm 2\, MeV/c^2$.

The CLAS collaboration searched for the Θ^+ in $\gamma d \to K^+K^- pn$ reaction with a photon energy of 2.474-3.115 GeV [42]. They detected K^+K^-p by the CLAS detector and the neutron was reconstructed by the missing mass technique. Two kinematic cuts are applied. One is $P_n > 0.08\, GeV/c$ to reject the events which neutron is a spectator. The other is $P_{K^+} < 1.0\, GeV/c$ because the K^+ track from the decay of the Θ^+ rarely exceeds this value. The nK^+ invariant showed a narrow peak at $1.542 \pm 0.005\, GeV/c^2$.

The CLAS collaboration searched for the Θ^+ also in $\gamma p \to \pi^+K^-K^+n$ reaction with a photon energy of 3.00-5.47 GeV [43]. They applied a kinematic cut of $cos\theta_{\pi^+} > 0.8$ and $cos\theta_{K^+} > 0.6$, where $cos\theta_{\pi^+}$ is the center-of-mass angle between a π^+ and a photon, $cos\theta_{K^+}$ is the center-of -mass angle between a K^+ and a photon, respectively. The first one was applied to enhance the t-channel π^+ exchange of the N^* production which decays into Θ^+ and K^-. The second one was applied to reduce the background from meson resonance production. After applying the cut conditions, the nK^+ invariant mass distribution showed a peak at $1550 \pm 10\, MeV/c^2$. Furthermore, after selecting the Θ^+ region in nK^+ invariant mass, the nK^+K^- invariant mass showed a excess near 2.4 GeV/c^2, suggesting a N^* which decays into K^- and Θ^+.

1.4.2 The high statistics experiments by the CLAS collaboration

The results written above supported the existence of the Θ^+. However, the situation soon became controversial. The CLAS collaboration performed a series of high statistics and high resolution experiments which are devoted to the Θ^+ search and reported the negative results. In [44], they reported the results of Θ^+ search in $\gamma p \to \bar{K}^0K^+n$ with a photon energy of 1.6-3.8 GeV. The nK^+ invariant mass distribution did not show any structure. This result is clearly in disagreement with that reported by SAPHIR [41]. For better comparison, the same cut condition as [41], $cos\theta^{CM}_{\bar{K}^0} > 0.5$, was applied and the photon energy was limited to 2.6 GeV in [44]. The nK^+ invariant mass again did not show any structure. The nK^+ invariant mass distributions for two groups are shown in Fig. 1.5. The number of $\Lambda(1520)$ seen

in K^+ missing mass was 57000±5500 for CLAS data while 630 ± 90 for SAPHIR data. The expected nK^+ invariant mass resolution is 3-4 MeV/c^2 for CLAS data while 10 MeV/c^2 for SAPHIR data. Because the quality of data is much better for CLAS's one, it is hard to believe the result reported by SAPHIR collaboration. In [44], CLAS collaboration also reported the negative results for Θ^+ search in $\gamma p \to \bar{K}^0 K^0 p$ reaction with a photon energy of 1.6-3.8 GeV. The acceptance for this reaction is complementary to that for the $\gamma p \to \bar{K}^0 K^+ n$ reaction. By combining two reaction modes, the upper limit for the cross section was set to be 0.7 nb (95% confidence level).

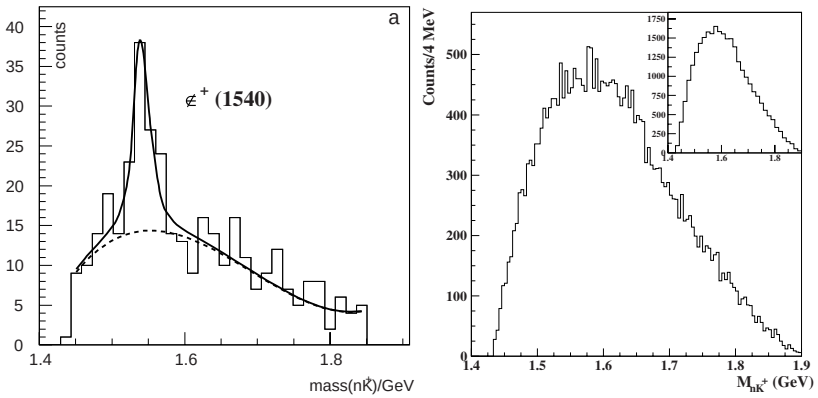

Figure 1.5: The nK^+ invariant mass distributions. Left plot is taken from [41] and right plot is taken from [44]. The inset for right plot shows the same spectrum with binning used in the left plot.

In [45], they reported the result of the Θ^+ search in $\gamma d \to K^+ K^- pn$ reaction with a photon energy of 0.8-3.6 GeV. This is an improved study of their previously published result [45] with an order of magnitude higher statistics. The nK^+ invariant mass did not show any structure. Figure 1.6 shows the comparison of two results under the same cut conditions and the same photon energy range. The previously observed peak was not reproduced in the new data. The upper limit for the cross section was set to be 3 nb (95 % confidence level).

In [46], they reported the result of the Θ^+ search in $\gamma d \to \Lambda n K^+$ reaction with a photon energy of 0.8-3.6 GeV [46]. They detected K^+, π^-, proton and the invariant mass of $p\pi^-$ was required to be close to the mass of the Λ. The neutron was reconstructed by the missing mass technique. Figure 1.7 shows the nK^+ invariant mass distribution without kinematic cuts (top) and after kinematic cuts on photon energy ($E_\gamma < 1.6\, GeV$) and neutron momentum ($p_n > 0.2\, GeV/c$). The photon energy cut was applied because theoretical calculation shows that $\gamma d \to \Lambda \Theta^+$ decreases rapidly with increasing photon energy. The neutron momentum cut was applied to remove the events which neutron is a spectator. The nK^+ distribution did not show any structure for both conditions. The upper limit for the cross section was set to be 5-25 nb (95% confidence level).

Very recently, the CLAS collaboration reported a evidence of the Θ^+ in the $\gamma p \to K^0_s K^0_L p$ reaction [47]. The data set is the same as [44]. They restricted the mass of the K^0_s and K^0_L to be close to the ϕ meson to increase the sensitivity by using the interference between ϕ meson production and Θ^+ production. After applying a cut condition of $t_\Theta \leq -0.45\, GeV/c^2$, where

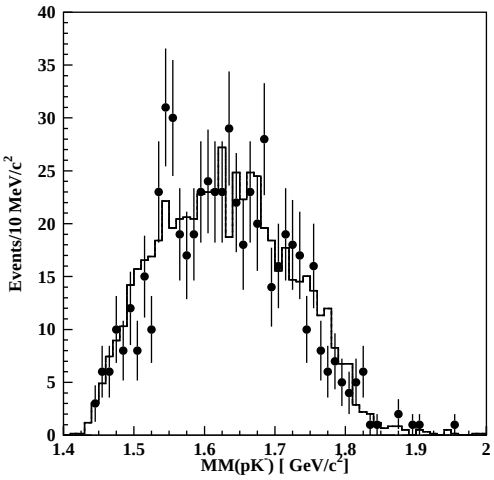

Figure 1.6: Comparison of the two nK^+ invariant mass distribution reported by CLAS collaboration. Points are previously published result [42] and histogram is new result [45] normalized (by a factor of 1/5.92) to get the same total number of counts.

t_Θ is the momentum transfer of the K^0_s, a narrow peak at $1.543 \pm 0.001\ GeV/c^2$ is seen. The statistical significance which was obtained as the log likelihood ratio of the signal+background hypothesis ti the hypothesis with background only corresponds to 5.9 σ.

Note that a dedicate experiment for the confirmation of their previously published positive result in $\gamma p \to \pi^+ K^- K^+ n$ reaction [43] has not been performed.

1.4.3 New result by the LEPS collaboration

The LEPS collaboration reported the further evidence of the Θ^+ in $\gamma d \to K^+ K^- pn$ reaction with a photon energy of 2-2.4 GeV [48] with a data taken in 2002-2003. The statistics is improved by a factor of 6 when compared with previously published LEPS result [1]. The detail of the analysis will be written in chapter 4. Figure 1.8 shows the nK^+ invariant mass distribution. The peak is seen at $1524 \pm 0.002 + 0.003\ GeV/c^2$. The width of the peak was consistent with the expected mass resolution. The Θ^+/K^+K^- of $(0.8 \pm 0.1) \times 10^{-2}$ was consistent with that of $(1.1 \pm 0.2) \times 10^{-2}$ obtained by the previous measurement. The statistical significance was obtained to be 5.1 σ by the shape analysis (described in chapter 4). The differential cross section was measured to be 12.2 nb/sr assuming constant matrix element.

As written in the previous section, CLAS collaboration also searched for the Θ^+ in the same reaction and reported the negative result [45]. However, two results can not be compared directly because several experimental conditions and analysis procedures are different. The LEPS spectrometer has the acceptance in $\theta\ < 20^\circ$ [49] while the CLAS has the acceptance in $\theta\ > 20^\circ$ [50]. The θ is a angle between a γ beam and a negative charged particle in the laboratory frame. Therefore, the acceptance for two experiments are almost exclusive. The photon energy ranges 2.0-2.4 GeV for LEPS experiment while 0.8-3.6 GeV for CLAS exper-

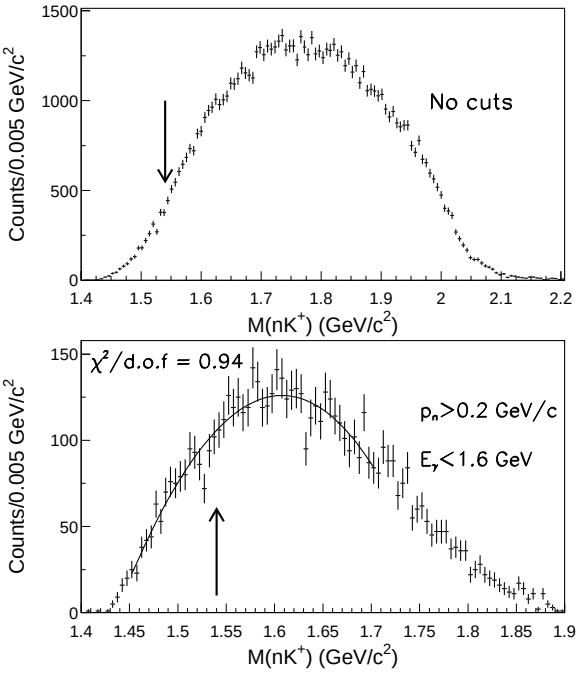

Figure 1.7: The nK^+ invariant mass distribution taken from [46]. Top: No kinematic cuts are applied. Bottom: Kinematic cuts written in the text are applied.

iments. The LEPS analyzed the quasi-free events while the CLAS required the re-scattering of the spectator proton in order to detect the proton. The ϕ events are removed by the cut condition of $M(K^+K^-) > 1.03$ (photon energy dependent) (LEPS) and $M(K^+K^-) > 1.07$ (CLAS). The difference of the photon energy and the angle range suggest that strong photon energy or angle dependence exist for the differential cross section. Therefore, to clarify the situation, more detailed studies like the measurement of differential cross section are necessary.

Finally, the results of the photo-production experiments are summarized in table 1.4.3.

Reference	Group	Reaction	Result	Limit	Mass(MeV)
[1]	LEPS	$\gamma C \to K^+K^-X$	positive	–	1540 ± 10
[41]	SAPHIR	$\gamma p \to K^0K^+n$	(positive)	–	$1540 \pm 4 \pm 2$
[43]	CLAS	$\gamma p \to \pi^+K^+K^-n$	positive	–	1550 ± 10
[44]	CLAS	$\gamma p \to \bar{K}^0K^+n$, $\gamma p \to \bar{K}^0K^0p$	negative	$\sigma < 0.7\,nb$	–
[45]	CLAS	$\gamma d \to K^+K^-pn$	negative	$\sigma < 3.0\,nb$	–
[46]	CLAS	$\gamma d \to \Lambda K^+n$	negative	$\sigma < 5 - 25\,nb$	–
[47]	CLAS	$\gamma p \to K^0_sK^0_Lp$	positive	–	1543 ± 1
[48]	LEPS	$\gamma d \to K^+K^-pn$	positive	–	$1524 \pm 2 + 3$

Table 1.4: Summary of the photo-production experiments.

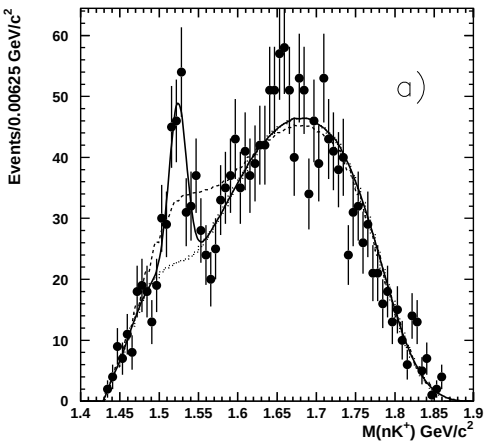

Figure 1.8: The nK^+ invariant mass distribution for new LEPS experiment [48].

1.4.4 Discussions about the production mechanism

As written in the previous section, the CLAS collaboration reported the negative result of the Θ^+ search in $\gamma p \to \bar{K}^0 K^0 \Theta^+$ reaction [44]. The Feynman diagrams corresponding to the Born term for this reaction are shown in Fig. 1.9. Note that these diagrams are common for $\gamma p \to \bar{K}^0 \Theta^+$ and $\gamma n \to K^- \Theta^+$ reactions. For the t-channel process, K exchange is forbidden because no electric charge exists at the $\gamma K^0 \bar{K}^0$ vertex. Only the K^* exchange via the magnetic coupling to the photon is allowed. Therefore, the negative result by CLAS indicates that the $pK^*\Theta^+$ coupling is very small if the Θ^+ exists. This indication is consistent with the negative results of the Θ^+ search in $\pi^- p \to K^- X$ [38] and $K^+ p \to \pi^+ X$ [37] reaction. For both reactions, the K exchange is forbidden because the spin and the parity can not be conserved simultaneously at the $\pi K^+ K^-$ vertex. Only the K^* exchange is allowed. For $K^+ p \to \pi^+ X$ reaction, the K exchange in u-channel is possible. However, the experimental setup in [37] does not have the acceptance in the backward region, where the u-channel process dominates. From these considerations, we can conclude that the $pK^*\Theta^+$ coupling is very small.

For $\gamma n \to K^- \Theta^+$ reaction, in addition to the Feynman diagrams shown in Fig. 1.9, the Feynman diagrams shown in Fig. 1.10 contribute. For the t-channel, the K^+ exchange is allowed. Furthermore, the contact term, which only exists in charge exchange process, contributes. The size of the $K^+ n \Theta^+$ coupling is constrained by the decay width of the Θ^+. Because the width of the Θ^+ is very narrow (at least less than 1 MeV/c^2), the $K^+ n \Theta^+$ coupling is also small. Diakonov pointed out that, in such a small $nK^+\Theta^+$ coupling, it was hard to see the Θ^+ in normal photo-production process and interference with $\Lambda(1520)$ or ϕ meson was necessary [51]. However, Nam et al. suggest that if the spin of the Θ^+ is 3/2, the cross section of the $\gamma n \to K^- \Theta^+$ reaction is large even for narrow width of the Θ^+ because of the large contribution from the contact term [52]. Large contribution from the contact term leads to the asymmetry of the photo-production cross section between neutron and proton target. The same argument can be applied to the $\Lambda(1520)$ photo-production because the spin

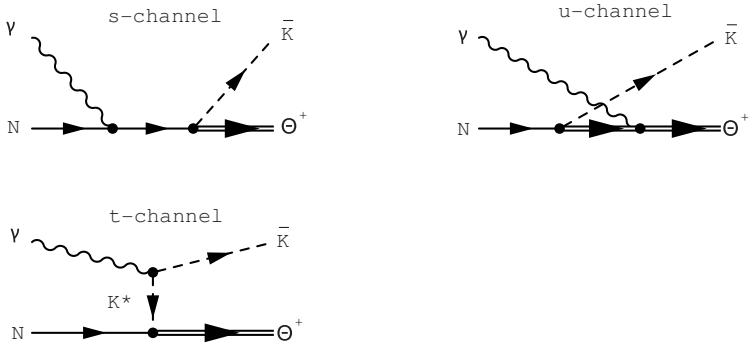

Figure 1.9: The Feynman diagrams of the Born terms for the $\gamma p \to \bar{K}^0\Theta^+$ and $\gamma n \to K^-\Theta^+$ reactions.

of the $\Lambda(1520)$ is 3/2. For the case of the $\Lambda(1520)$ photo-production, the cross section for a proton target is larger than that of a neutron target because the contact term contributes to the charge exchange process. The asymmetry of the cross section for the $\Lambda(1520)$ photo-production is experimentally confirmed by the LEPS collaboration [53].

Figure 1.10: The Feynman diagrams of the Born terms for the $\gamma n \to K^-\Theta^+$ reaction in addition to the diagrams shown in Fig. 1.9.

1.5 Aim of this thesis

In 2006-2007, the LEPS collaboration took new data with almost the same setup as previously published result [48] with about 2.6 times higher statistics to clarify the situation for the existence of the Θ^+. To obtain a high intensity photon beam, a two laser injection system has been developed. Blind analysis is applied to confirm the previous positive result. Once the peak is confirmed, the measurement of the differential cross section is also possible with high statistics data.

In this thesis, the result of the Θ^+ search in $\gamma d \to K^+K^-pn$ reaction with this new data is presented. The experimental setup, details of the analysis, and the result of the Θ^+ search are presented.

Chapter 2

Experiment

The experiment was performed at the SPring-8/LEPS facility. The SPring-8/LEPS facility provides a linear-polarized photon beam with a high intensity and a large degree of polarization. The linear-polarized photons are produced by the backward-Compton-scattering process of laser photons from circulating 8-GeV electrons in the storage ring. Since the energy of the electron beam in SPring-8 is 8 GeV, the photon beam with a few GeV energy can be produced.

The LEPS magnetic spectrometer has been used to detect Kaons in the $\gamma n \to K^- \Theta^+ \to K^- K^+ n$ and $\gamma p \to K^+ \Lambda(1520) \to K^+ K^- p$ reactions. The Kaons tracks are identified by measuring momenta and time-of-flights. The SPring-8/LEPS facility and the LEPS spectrometer are described in detail in this chapter.

2.1 SPring-8 facility

The SPring-8 (Super-Photon ring-8 GeV) is a third-generation synchrotron-radiation (SR) facility which has been completed in 1997. Third-generation facilities are optimized to get a high-brightness SOR light-source by using insertion devices, mainly undulators. There are three third-generation SR facilities with $E_e > 5$ GeV, in the world. They are ESRF (Grenoble), APS (Argonne) and SPring-8 (Japan). SPring-8 is the largest and brightest. The energy of circulating electrons in SPring-8 is 8 GeV.

The accelerator complex of SPring-8 is composed of an injector linac, a booster synchrotron, and a low-emittance and high-brightness storage ring. Fig. 2.1 shows the schematic view of the accelerator complex. Electrons are generated at an electron gun and are accelerated to an energy of 1 GeV in the injector linac with a length of 140 m. A 1 GeV electron beam is transported to the booster synchrotron with a 396 m circumference, and are accelerated up to 8 GeV. The 8-GeV electron beam is injected from the synchrotron into the storage ring with a 1436 m circumference and stored.

The 8-GeV electrons circulate in the storage ring with a frequency of 0.2088 MHz. The time interval of the successive bunches for electrons is 1.966 nsec. There are 2436 bunches on the circle in the storage ring. Electrons are filled in some bunches with various filling patterns. The maximum current of the 8 GeV electron beam is 100 mA. The electron beam has a small emittance of $\varepsilon = 6$ nm·rad with the average beam widths of $\sigma_x = 75$ μm and $\sigma_y = 25$ μm in the horizontal and vertical directions.

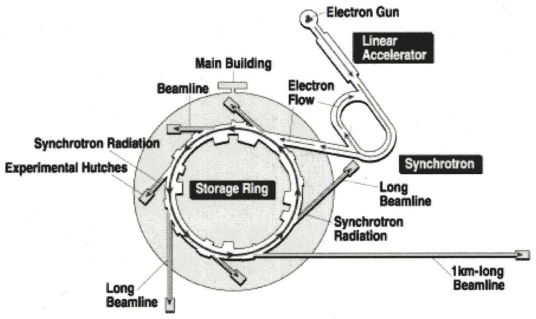

Figure 2.1: Schematic view of the accelerator complex of SPring-8.

2.2 LEPS facility

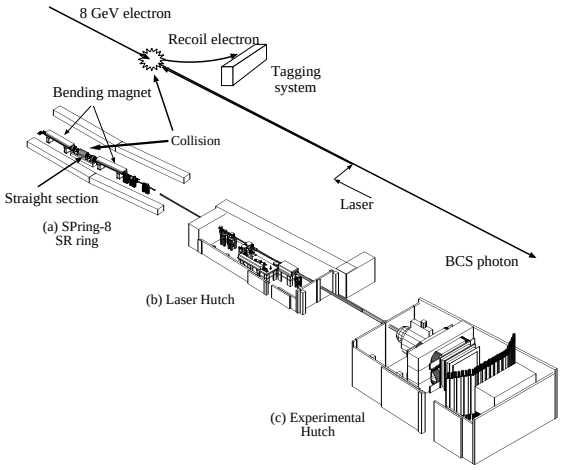

Figure 2.2: Schematic view of the LEPS facility at SPring-8. The facility consists of three parts;(a) Laser-electron collision part in the storage (SR) ring, (b) Laser hutch for a laser injection, and (c) Experimental hutch. A schematic explanation of the collision between an electron and a laser photon in backward-Compton scattering is inserted in the figure.

At the Laser-Electron-Photon facility at SPring-8 (LEPS), a multi-GeV photon beam is produced by the backward-Compton-scattering (BCS) process of laser photons from the circulating 8-GeV electrons.

The schematic view of the LEPS beam line is shown in Fig. 2.2. The beam line consists of three parts; (a) Laser-electron collision part in the storage (SR) ring, (b) Laser hutch for laser injection, and (c) Experimental hutch where a spectrometer is placed. The BCS process is illustrated in the figure. Laser photons which are optimized in the laser hutch are injected to the storage ring. We have a 7.8 m long straight section between two bending magnets in the storage ring as shown in Fig. 2.2. In this straight section, the BCS process takes place if a laser

photon collides with a 8-GeV electron. Photons produced by the BCS process are provided to the experimental hutch and irradiate a target. The recoil electrons are detected by a tagging system placed at the exit of the bending magnet to measure the photon beam energy. A series of experiments by using the BCS photon beam started in 2000. The BCS process and devices to produce a linear-polarized photon beam are described in this section.

2.2.1 Backward Compton scattering

The general properties of the backward-Compton-scattering process in the laboratory system are described in this section. Fig. 2.3 shows the kinematic values of the backward-Compton-scattering process. If a laser photon with an energy k_1 strikes an electron with a high energy E_e with a relative angle $\theta_1 \simeq 180°$, it is scattered with a scattering angle of θ_2. If $E_e \gg k_1$, the scattered photon is directed strongly in the backward direction due to the Lorentz boost. The scattered photon (BCS photon) gains an enormous energy from the electron by

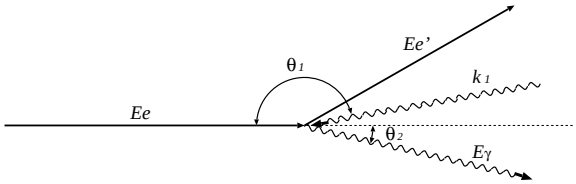

Figure 2.3: Kinematic variables of the backward-Compton-scattering process in the laboratory frame.

the Fitzgerald-Lorentz effect in the recoil process. The energy of a BCS photon E_γ is denoted as

$$E_\gamma = k_1 \frac{1-\beta cos\theta_1}{1-\beta cos\theta_2 + \frac{k_1(1-cos\theta)}{E_e}} \tag{2.1}$$

where β is an incident electron velocity in unit of the speed of light and $\theta = \theta_2 - \theta_1$. Assuming $\gamma = E_e/m_e \gg 1$, $\beta \simeq 1$, $\theta_1 \simeq 180°$ and $\theta_2 \ll 1$, Eq. (2.1) can be rewritten as

$$E_\gamma = \frac{4E_e^2 k_1}{m_e^2 + 4E_e k_1 + \theta_2^2 \gamma^2 m_e^2}, \tag{2.2}$$

where m_e is the electron mass of 0.511 MeV and $\gamma \sim 16,000$ at $E_e = 8$GeV. The maximum energy of a BCS photon (Compton edge) is obtained at $\theta_2 = 0°$:

$$E_\gamma^{max} = \frac{4E_e^2 k_1}{m_e^2 + 4E_e k_1}. \tag{2.3}$$

The differential cross section of the BCS process is written as a function of the BCS photon energy [55]:

$$\frac{d\sigma}{dE_\gamma} = \frac{2\pi r_e^2 a}{E_\gamma^{max}}(\chi + 1 + cos^2\alpha) \tag{2.4}$$

$$a = \frac{m_e^2}{m_e^2 + 4E_e k_1} \tag{2.5}$$

$$\chi = \frac{\rho^2(1-a)^2}{1-\rho(1-a)} \tag{2.6}$$

$$cos\alpha = \frac{1-\rho(1+a)}{1-\rho(1-a)} \tag{2.7}$$

$$\rho = \frac{E_\gamma}{E_\gamma^{max}} \tag{2.8}$$

where $\gamma_e = 2.818$ fm is the classical electron radius. Fig. 2.4 shows the differential cross sections for the BCS process between 8 GeV incident electrons and laser photons with a wavelength 355 nm. Photons with the sub-GeV energy can be efficiently obtained by the BCS process.

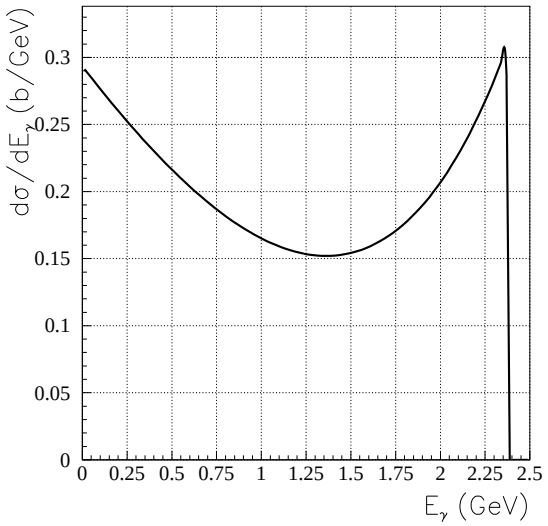

Figure 2.4: Differential cross sections of the BCS process with the 8 GeV incident electron beam for laser photons with a wavelength of 355 nm.

The linear (circular) polarized BCS photons can be made by using linear (circular) polarized laser photons. When a laser photon is polarized, the polarization is transferred to a BCS photon. The degree of polarization (P_γ) of a BCS photon is proportional to that of a laser photon (P_{laser}) [55]. The linear polarization is given by

$$P_\gamma = P_{laser}\frac{(1-cos\alpha)^2}{2(\chi+1+cos^2\alpha)}. \tag{2.9}$$

The circular polarization is given by

$$P_\gamma = P_{laser}\frac{(2+\chi)cos\alpha}{(\chi+1+cos^2\alpha)}. \tag{2.10}$$

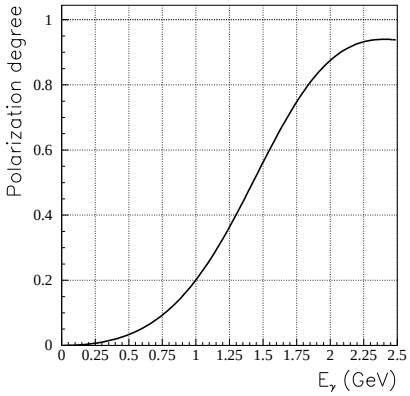

Figure 2.5: Polarization of the BCS photon as a function of E_γ by using the 8 GeV incident electron beam when the laser photon is 100% polarized. The wavelength of the laser photon is 355 nm. (a):Linear polarization and (b):Circular polarization.

Fig. 2.5 shows the linear and circular polarizations of a BCS photon as a function of E_γ by using the 8 GeV incident electron beam when the polarization of a laser photon is 100%. The wavelength of laser photons is 355 nm. The degree of polarization is maximum at the Compton edge ($\theta_2 = 0°$). The spin-flip amplitude for highly relativistic electrons vanishes, and scattered photons almost retain the initial laser polarization at the Compton edge. In the case of the linear polarization, the maximum polarization is obtained as $P_\gamma = P_{laser}\frac{2a}{1+a^2}$ from Eq. (2.9). The linear polarization is about 94% at the maximum energy when the incident electron with $E_e = 8$ GeV and a 355 nm laser with 100% polarization are used.

In the present experiment, a linear-polarized photon beam was produced by a laser with a wavelength of 355 nm. The size of the BCS photon beam with $E_\gamma = 1.5$ GeV $\sim$ 2.4 GeV was obtained to be $\sigma_x \sim 3.5$ mm and $\sigma_y \sim 2.0$ mm. The size difference between σ_x and σ_y is due to the emittance of the 8-GeV electron beam.

2.2.2 Laser operating system

Figure 2.6 shows the schematic view of the laser system. For this experiment, two laser injection system is developed to increase LEP beam intensity (compare with Fig. 2.9 of [57]). The laser itself is also changed.

In the previous experiment, An ultra violet Ar laser was used. The typical power of the laser was 5 W. The laser oscillates with a multi-line mode, and the wave length ranges from 333 to 364 nm. On the other hand, in this experiment, two solid-state lasers (Coherent Paladin) are used as a photon source. The typical power of the laser is 8 W, which is larger than Ar laser. The laser oscillates with a single line mode with a wave length of 355 nm. The maximum LEP beam energy is about 2.385 GeV. The size of the laser beam is 1mm ϕ. The laser beam is vertically polarized. The beam intensity of 2.0 Mcps was achieved at the maximum. The energy spectrum of the LEP beam measured by Tagging system for two data sets are shown in 2.7. The difference of the binning for two data sets is due to the different Tagging systems

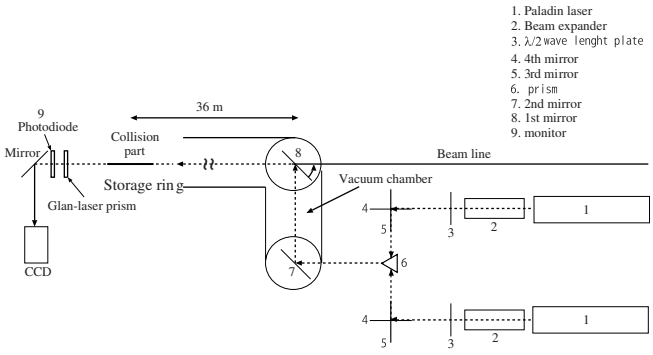

Figure 2.6: Schematic view of the laser operating system

for two data sets as written in section 2.3.

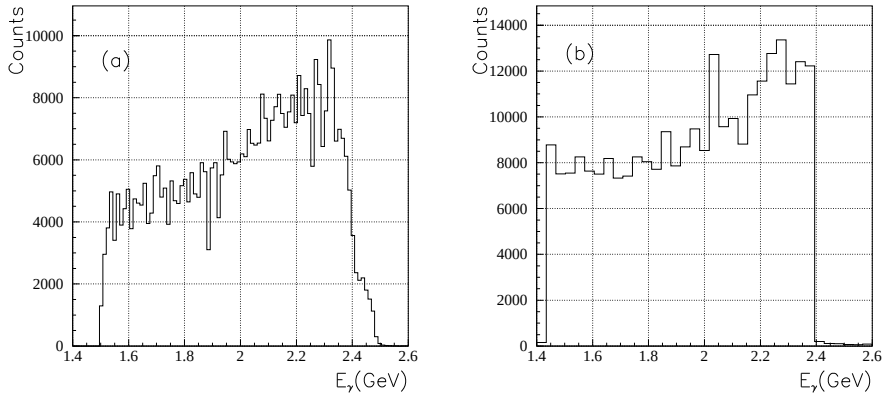

Figure 2.7: The energy spectra of LEP beam. (a) For previous experiment. (b) For this experiment.

The laser beams travel about 36 m before they collide with electron beam. The beam expanders are used to tune the beam size at the collision point. The beam expanders enlarge and focus the laser beams by a concave lens and a convex lens made of UV grade quartz. The magnification factor of the expander is 28 (laser beam size after the expander is 28 mm).

The polarization of the laser beams are controlled by the $\lambda/2$ plates. Since the laser beams are vertically polarized, the optic axis of the $\lambda/2$ plates are set to be 0 degree when vertically polarized photons are used and set to be 45 degree when horizontally polarized photons are used. The polarization of the laser was changed once a day. In the previous experiments, the $\lambda/2$ plate was put just after the laser. Then, the damage to the $\lambda/2$ plate was observed and the transmission ratio became worse. To avoid the damage, $\lambda/2$ plates with large size (50 mmϕ) are put after the beam expander where the power density is much lower. The transmission ratio of the $\lambda/2$ plates did not change during the experiment.

Four mirrors and one prism is used to guide the laser beam to the storage ring. The angle of 4th and 3rd mirrors are controlled by pulse motors to tune the direction of the laser beams.

The 4th and 3rd mirrors are made of quartz with a size of 80 $\phi\times$ 12 t (mm). Two laser beams are reflected by both sides of the prism and guided to the 2nd mirror. Prism is made of quartz. Figure 2.8 shows the schematic view of the prism. The 2nd mirror and 1st mirror are put inside the vacuum chamber. They are made of Si base with aluminum coating which have good heat conductivity. Size of 2nd mirror is 100 $\phi \times$ 19 t (mm) and that of 1st mirror is $100\phi \times 6t(mm)$. 1st mirror is made thin because LEP beam pass it. 1st mirror is cooled by water circulation.

The polarization of the laser photons is measured by using laser photons which pass through the collision part. A Glan-laser prism is used as a polarimeter to measure the polarization. The Glan-laser prism has a special axis. Only photons with the polarization parallel to this axis can pass through the prism. By rotating the prism and measuring the intensity of the laser beam after the prism, the intensity distribution of the laser beam is obtained as a function of the rotation angle ϕ. The intensity is measured by a photo-diode (HAMAMATSU S1406-05). Fig. 2.9(a) and (b) show the intensity distribution measured by the photo-diode for vertically and horizontally polarized laser photons. The data is fitted by a function of sinϕ. The polarization angle and degree are determined by this fitting. The laser beam is optimized to have the maximum polarization.

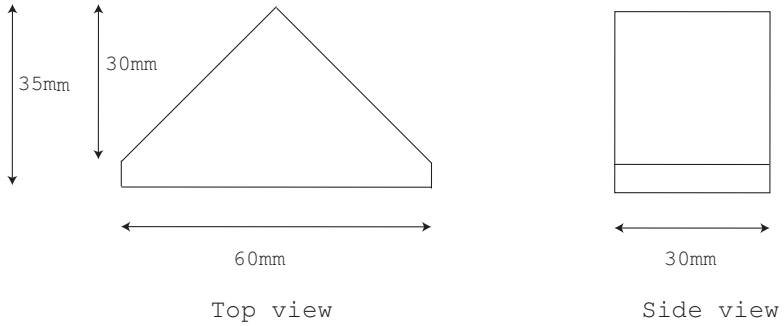

Figure 2.8: Schematic view of the prism

2.3 Tagging system

The energy E_γ of the BCS photon beam is determined by the recoil electron energy $E_{e'}$ as

$$E_\gamma = E_e - E_{e'}. \tag{2.11}$$

The energy of the 8-GeV circuiting electron E_e was calculated on the basis of measured field distributions of magnets in the storage ring. The energy was determined as 7.975 $\pm$ 0.003 GeV [54]. The energy $E_{e'}$ is measured by a tagging system located in the storage ring. Since an electron scattered by the BCS process looses its energy, it is relatively strongly bent and deviates from the normal orbit in the 8-GeV ring when it passes through the bending magnet placed at the end of the straight section (see Fig. 2.2). The tagging system is installed at the exit of the bending magnet to detect the recoil electrons.

Until 2003, a tagging system consists of a silicon strip detector (SSD) and a plastic scintillator hodoscope is used at the LEPS experiment [57]. Although the position resolution of SSD

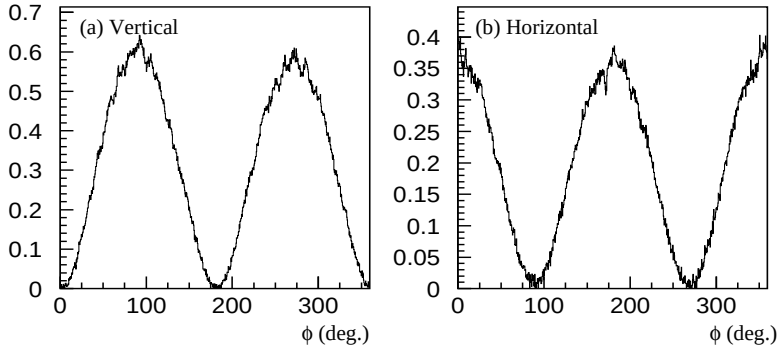

Figure 2.9: Intensity distribution of the laser beam measured by the photo-diode for (a) vertically polarized laser photons and for (b) horizontally polarized laser photons. The distribution is fitted by a function of sinϕ. The line is the fitting function.

is very good (pitch size is 0.1 mm), the timing resolution of the SSD is not good (several μs). As the tagging rate is about 1Mcps, it is likely that SSD can not select an electron track which corresponds to an event. To incorporate with high beam intensity, a tagging system consists of scintillating fibers (TAG-SF) and plastic scintillator hodoscopes (TAG-PL) has been developed and replaced with old tagging system since 2004.

Fig. 2.10 shows the structure of the tagging system. The tagging system is placed at the outside of a beam vacuum pipe for the 8 GeV electron beam. The tagging system covers a region 4.0 - 6.6 GeV in the energy of recoil electrons. This energy region corresponds to the energy of the BCS photons 1.4 - 3.0 GeV. The lower limit of 1.4 GeV is due to the fact that the tagging system can't be positioned closer to the nominal orbit of the 8 GeV electrons.

A hit position of an electron track is measured by the TAG-SF. The TAG-SF consists of two layers (TAG-SFF and TAG-SFB). Each fiber layer consists of 55 fiber bundles. Each fiber bundle is made of six fibers with the cross section of $1 \times 1\ mm^2$. A schematic view of the fiber is shown in Fig. 2.11. There exist 4.2 % inefficient region in one fiber. Two layers are arranged with an overlap of 0.5 mm to cover the inefficient region of the one layer. The signal from fiber bundles are read by PMT (HAMAMATSU R5900-00-M4, H6568-10).

The trigger of the tagging system is cleaned up by taking a coincidence of the TAG-SF and the TAG-PL. TAG-PL consists of 2 layers of 5 plastic scintillation counters. The size of the plastic scintillator is 10.0 mm high, 7.4 mm wide, and 3.0 mm thick. The plastic scintillator which is closest to the 8-GeV electron beam has the width of 5.5 mm. The plastic scintillators are arranged with an overlap of 2.7 mm. The signal of the TAG-PL is read through the photo-multiplier-tube (HAMAMATSAU H3164-10).

2.3.1 Beam line setup

The BCS photon beam travels from the collision point to the experimental hutch through the laser hutch. Fig. 2.12 illustrates the setup of the beam line. There are some materials in the

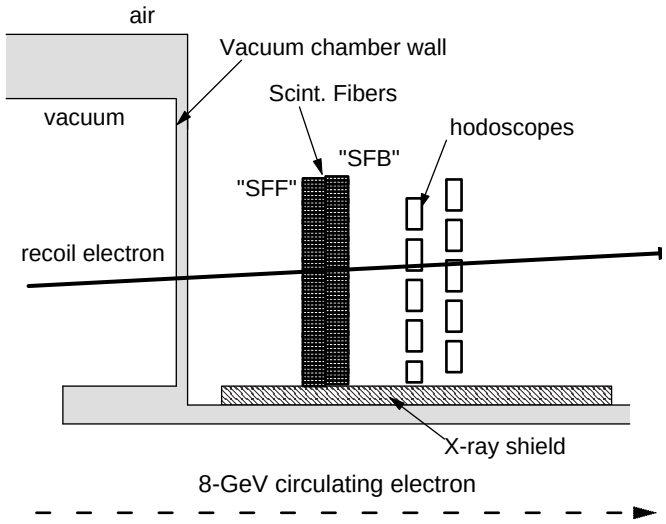

Figure 2.10: Schematic view of the tagging system

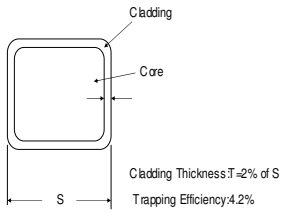

Figure 2.11: Schematic view of the fiber

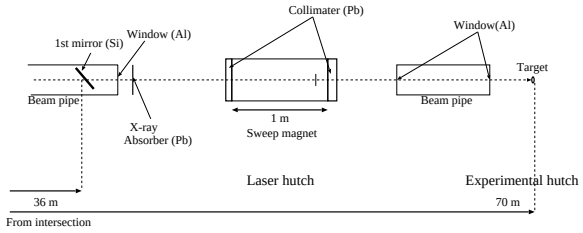

Figure 2.12: Schematic view of the LEPS beam line setup.

path of the photon beam. They are the first mirror, aluminum windows of the beam pipes and a X-ray absorber. When the photon beam hits these materials, some of photons convert to e^+e^- pairs. The materials and their conversion rate to e^+e^- pairs are summarized in Table 2.1. The first mirror is made of silicon with a thickness of 6 mm. Since the mirror is tilted by 45° to inject laser photons into the storage ring, the effective thickness is thus $6 \times \sqrt{2}$ mm. Capton sheets are used as windows of beam pipes, the exit of a beam pipe from the SR ring, and the enter and exit of a beam pipe which connects the laser hutch and experimental hutch. An Al plates is used in total in the beam line. A lead absorber with a thickness of 2.0 mm is placed after the beam pipe from the SR ring to absorb X-rays. The detectors of a spectrometer are protected with this absorber from a radiation damage. The thickness of 2.0 mm is determined by the operation of the detectors and the radiation safety. The conversion rate of the photon beam is 32.5 % in total. The intensity of the photon beam is reduced by about 32.5 % before it arrives at a target in the experimental hutch. The transmission of the photons from the reaction point to the target was measured by the tagging counter and gamma counters. The electron with a energy of around 6.7 GeV, which corresponds to the photon energy of around

1.3 GeV, hits the wall of the shield and create electro magnetic shower. Although the shower events hits Tagging counter, these event are discarded at the analysis. The measured effective transmission including the effect of shower is around 53 %.

Table 2.1: Materials inserted in the beam line.

	Material	Radiation length (mm)	Thickness (mm)	Conversion rate (%)
First mirror	Si	93.6	$6\times\sqrt{2}$	6.77
Vacuum windows	Al	89.0	0.55×3	0.44×3
Absorber	Pb	5.6	2.0	24.25

The e^+e^- pairs created in the materials should be removed before a target. To remove the e^+e^- pairs, we use a sweep magnet located in the laser hutch. Fig. 2.13 shows the structure of the sweep magnet. The size of the iron yoke is 176 mm high, 560 mm wide, and 1000 mm long. Two permanent magnets are installed in the iron yoke. The size of each magnet is 35 mm high, 58 mm wide, and 1000 mm long. They are faced with a gap of 44 mm. The strength of the magnetic field is 0.6 T at the center. The e^+e^- pairs produced at the first mirror, the aluminum window, the X-ray absorber and the residual gas in the beam pipe are removed from the beam line by the sweep magnet. Lead collimaters are placed at the upstream and downstream positions of the sweep magnet. The thickness of the upstream (downstream) collimaters is 50 (150) mm. The upstream (downstream) collimaters have a hole with a diameter of 20 (25) mm. The e^+e^- pairs with a momentum below 2.1 GeV/c are blocked by the downstream collimator. The other e^+e^- pairs with a momentum above 2.1 GeV/c pass through the hole of the downstream collimator.

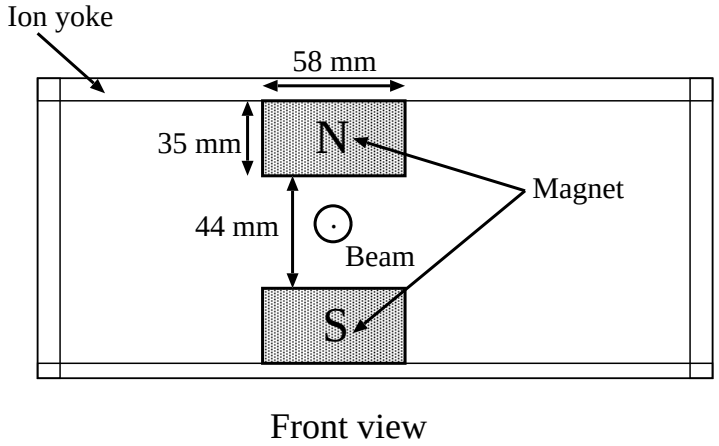

Figure 2.13: Structure of the sweep magnet.

2.4 LEPS spectrometer

The LEPS spectrometer is located in the experimental hutch to identify charged particles produced at the target. Fig. 2.14 shows the LEPS spectrometer. The incidence direction of

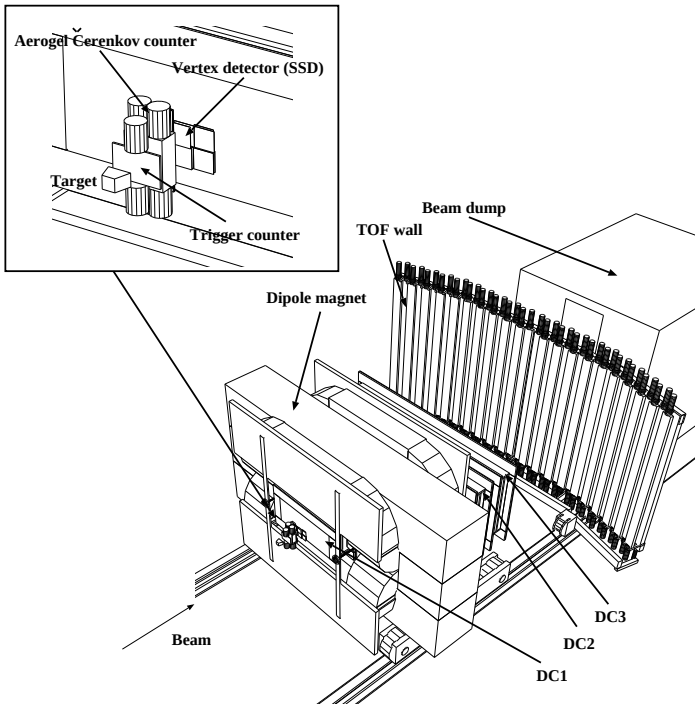

Figure 2.14: Overview of the LEPS spectrometer.

the photon beam is displayed in the figure. The LEPS spectrometer consists of an upstream-veto counter, a trigger counter, a silica-aerogel Čerenkov counter, a vertex detector (silicon strip detectors), a dipole magnet, three drift chambers (DC1, DC2 and DC3), and a TOF wall. Charged particles produced at the target are defined by the trigger counter. The silica-aerogel Čerenkov counter is used to eliminate the e^+e^- background events. The vertex detector and three drift chambers are used as tracking devices with the dipole magnet to measure momenta of charged particles. A time-of-flight is measured by using the TOF wall. A beam dump is placed behind the spectrometer for the purpose of a radiation shielding.

2.4.1 Trigger counter (TRG)

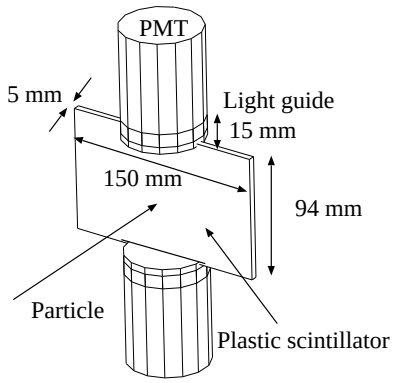

Figure 2.15: Trigger counter.

A trigger counter (TRG) is a plastic scintillation counter located at the position of 15 cm downstream of the center of the target cell to identify the event signals from charged particles produced at the target. Fig. 2.15 shows the schematic drawing of the trigger counter. The size of the plastic scintillator (BC-408) is 94 mm high, 150 mm wide, and 5 mm thick. Two 2-inch-diameter fine-mesh PMT's (HAMAMATSU H6614-01) are coupled to the upper and lower sides of the plastic scintillator through light guides with a thickness of 15 mm. The trigger counter is used as a reference counter to measure the time-of-flight with the RF signals.

2.4.2 Silica-aerogel Čerenkov counter (AC)

Main background events are the e^+e^- pairs produced at the LH_2 target and at the TRG in a measurement of hadronic reactions. The cross section of the e^+e^- pair production in LH_2 is 21 mb which is two orders of magnitude larger than that of hadronic reactions of about 0.15 mb. The cross section of the e^+e^- pair production in a plastic scintillator is 380 mb while that of hadronic reactions is about 2.0 mb.

A silica-aerogel Čerenkov counter (AC) was used to reject the e^+e^- events at the trigger level. The index of refraction of the silica aerogel radiator used in the present experiment is 1.03. Fig. 2.16 shows the relation between momentum and velocity (β) of e^+e^-, pion and Kaon. When a particle with a velocity $\beta > 1/n$ passes through a transparent material with a refractive index n, Čerenkov lights are emitted. The Čerenkov thresholds for e^+e^-, pion and Kaon are 0.002 GeV/c, 0.57 GeV/c and 2.0 GeV/c, respectably. Čerenkov lights are collected at the photo cathode of a PMT. The signal is used as a veto signal in the trigger logic.

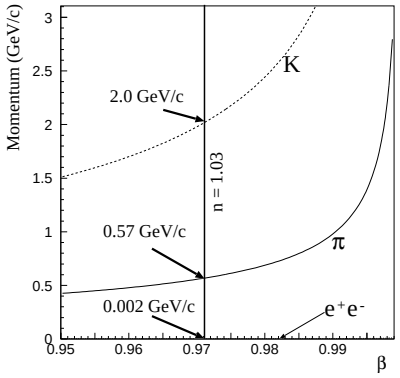

Figure 2.16: Relation between momentum and β for e^+e^-, π and K. A particle with $\beta > 1/n$ emits Čerenkov lights. The line corresponding to an index of 1.03 is shown in the figure.

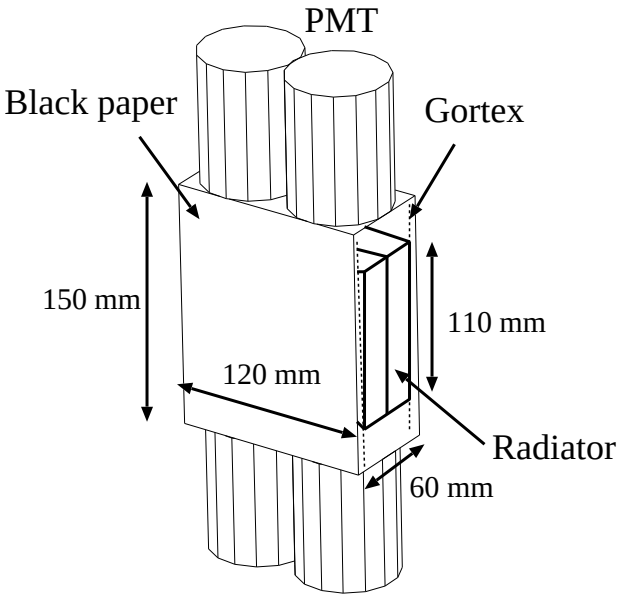

Figure 2.17: Silica aerogel Čerenkov counter (AC).

The AC is installed just behind the trigger counter to detect both an electron and a positron simultaneously. Because the e^+e^- pairs emerge with a small angle ($< 0.12°$), the e^+e^- pairs can be detected efficiently. The structure of the AC is shown in Fig. 2.17. The size of the counter box is 150 mm high, 120 mm wide, and 60 mm thick. The box is made of a black paper. The size of the silica aerogel radiator is 110 mm high × 110 mm wide, and 25 mm thick. The two sheets of radiators are inserted into the AC box as shown in Fig. 2.17. To collect Čerenkov lights emitted in the radiators, Gortex (white sheet) is used as a random reflector. The inside the AC box except for the photocathodes is covered with Gortex. The reflectivity of Gortex is about 95% [70]. The collected lights are read by four 2-inch fine-mesh PMT's (HAMAMATSU H6614-01) which are coupled to the upper and lower sides of the box. The AC efficiency to detect the e^+e^- pairs is about 99.9 %.

2.4.3 e^+e^- Blocker

The e^+e^- pairs produced at the target and the TRG spread out mostly in the median plane by the magnetic field in the dipole magnet because they emerge with a small angle. Some of electrons or positrons with a low energy come out beyond the acceptance of the beam dump which is located behind the spectrometer, and hit directly thin walls of the experimental hutch. This causes a problem in terms of radiation safety. The e^+e^- blocker is used in the dipole magnet to block low energy particles. The schematic view of the e^+e^- blocker is shown in Fig. 2.18. The e^+e^- blocker with two lead bars is placed 20 cm downstream of the center of

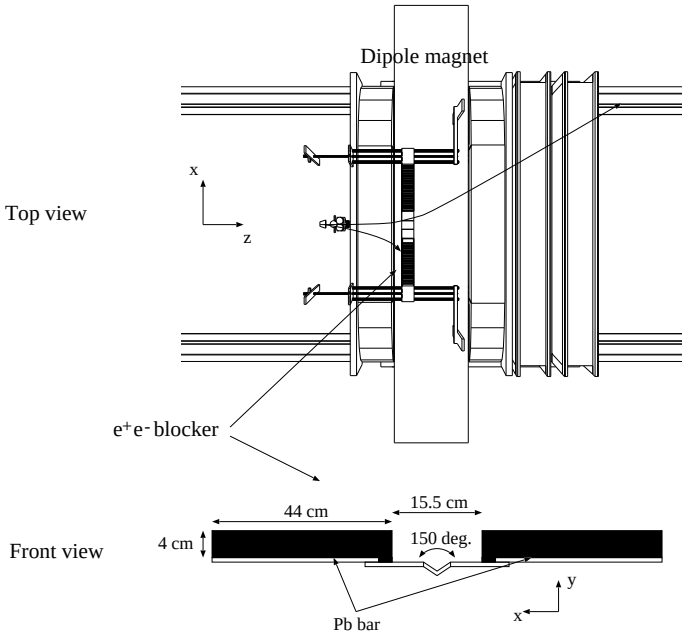

Figure 2.18: Drawing of the e^+e^- blocker.

the dipole magnet. The size of each Pb bar is 4 cm high, 44 cm wide, and 10 cm thick. The gap distance between two Pb bars is 15.5 cm. The e^+e^-'s with above 1 GeV/c momentum can go through the gap. The gap distance can be changed by using the small pieces of the Pb blocks. The e^+e^- pair emerges mostly asymmetrically in energy. In most cases, one of pairs is blocked by the blocker, while the other survives and escapes through the 15.5 cm gap and is stopped by the beam dump. The Pb bars are supported by two thin channels with a 0.2 cm thickness. A V-shaped thin bar (SUS) with a thickness of 0.5 cm connects a thin channel with one another in the center. The V-shape structure opens at 150° and has 1.5 cm in depth to let the photon beam pass through (see Fig. 2.18). The blocker is put down by the weight itself and the center in the y-direction is -7 mm.

2.4.4 Vertex detector (SVTX)

A vertex detector (SVTX) is used to determine a trajectory of a charged particle with drift chambers and determine a vertex point with a high precision by the track position close to the target. The SVTX is placed just after the AC. Fig. 2.19 shows the front view of the SVTX. The SVTX consists of two layers of silicon strip detectors (SSD's). One of layers is used to measure a x-position and the other is used to measure a y-position. The strip pitch is 0.12 mm and the thickness is 0.3 mm. The SVTX has a rhombic-shaped hole for the beam path which is 10 mm $\times$ 10 mm in size.

VLSI chips (VA) [56] are used as a readout circuit of the SSD's. Silicon strips and the VA chip are mounted on a printed circuit board called hybrid board. The hybrid board is connected to a repeater card which contains level converters for logic signals, buffer amplifier for analog output signals, and adjustable bias supplied for the VA chip. The VA ship is controlled by a VME board. Analog signals from the VA chip are sent to a flash ADC module through the repeater card. The analog signal from the silicon strip is read out only when the trigger signal is made.

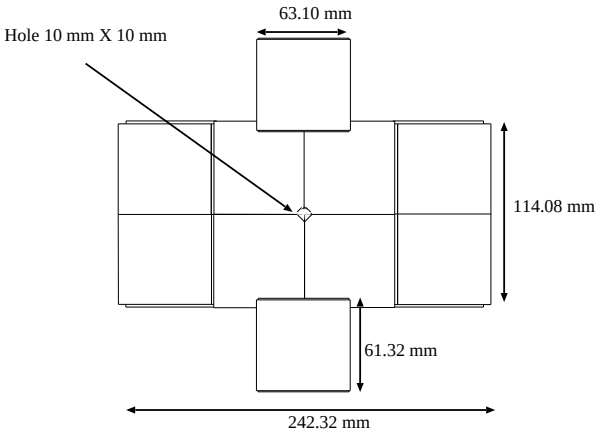

Figure 2.19: Front view of the SVTX.

2.4.5 Drift chambers

A tracking of a charged particle is performed by using hit information from the SVTX and three MWDC's (multi wire drift chambers). DC1 is located upstream of the dipole magnet. It has the active area of 600 mm $\times$ 300 mm. Fig. 2.20 shows a drawing of field, shield and sense wires in DC1. DC1 has 6 planes, x1, x2, u1, u2, v and x3. The x3 wires are made additionally because a charged particle begins to be spread out by the magnetic field in DC1. Sense wires of x1-x2 and u1-u2 are positioned with a 6 mm spacing and wires of x3 and v are positioned with a 12 mm spacing. The field wires are arranged in a hexagonal shape. The shield wires are positioned along the windows to shape the electric field. The inclination angle of the u and v wires is 45° with respect to the horizontal plane. DC2 and DC3 are installed downstream of the dipole magnet and have the active area of 2000 mm $\times$ 800 mm. Both DC2 and DC3 have 5 planes, x1, x2, u1, u2 and v. The design of DC2 and DC3 is the same as DC1 as shown

in Fig. 2.20, but there is no x3 wires in DC2 and DC3. Sense wires of x1-x2 and u1-u2 are positioned with a 10 mm spacing, and the wires of v are positioned with a 20 mm spacing. The u and v direction are inclined by 30° with respect to the vertical plane. The material of the sense wires is gold-plated tungsten (Au-W) and the wire diameter is 25 and 30 μm for DC1 and DC2, DC3, respectively. The field and shield wires are made of Au-BeCu with a diameter of 100 μm. The windows are made of mylar with a thickness of 125 μm. The design parameters of the DC's are shown in Table 2.2. The gas mixture used to operate the DC's is 70 % argon and 30 % isobutane. The efficiency is more than 98% and is typically 99%.

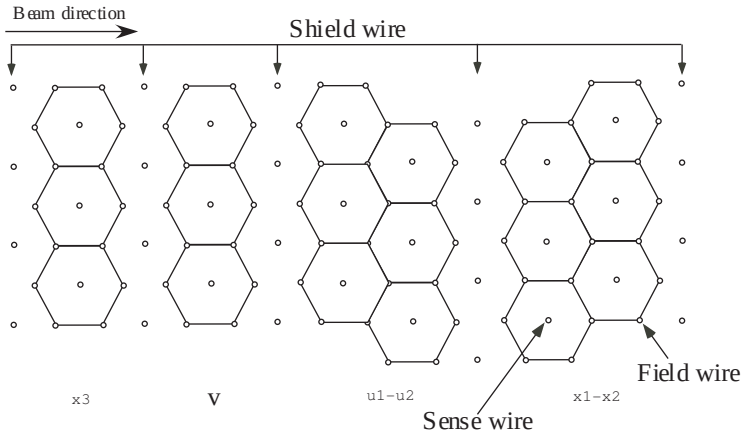

Figure 2.20: Drawing of field, shield and sense wires in the multi wire drift chamber, DC's.

Table 2.2: Design parameters of the MWDC's. The location of the center of each DC is along the z-axis. The location of z=0 is defined as the center of the dipole magnet.

	Coordinate	Orientation	Number of sense wire	Wire spacing (mm)	Active area x × y (mm^2)	Location z (cm)
DC1	x1-x2	0°	48	6	600 × 300	-466.0
	u1-u2	45°	48	6		
	v	135°	48	12		
	x3	0°	48	12		
DC2	x1-x2	0°	104	10	2000 × 800	860.5
	u1-u2	120°	78	10		
	v	60°	79	20		
DC3	x1-x2	0°	104	10	2000 × 800	1260.5
	u1-u2	120°	78	10		
	v	60°	79	20		

2.4.6 TOF wall

Time-of-flights of charged particles are measured by a TOF wall. The TOF wall is placed downstream of the DC3 with a full angular coverage of the LEPS spectrometer. Fig. 2.21 shows

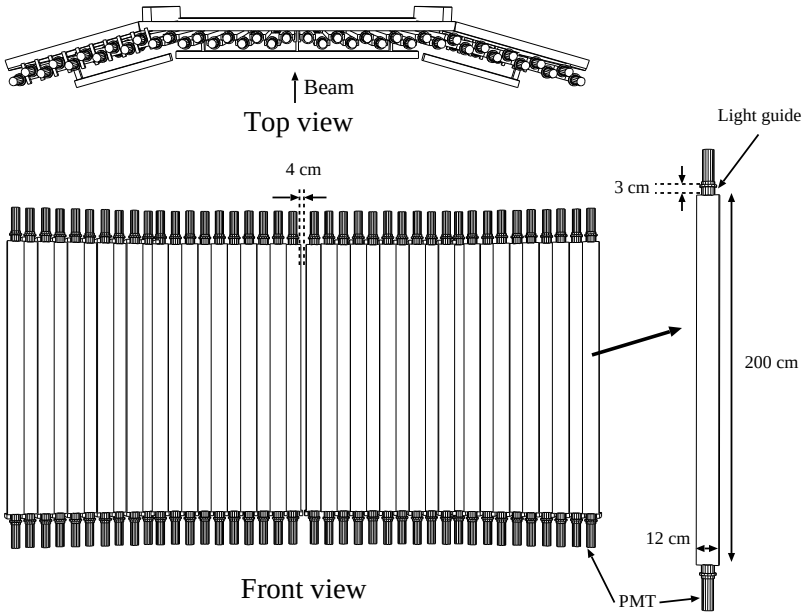

Figure 2.21: Drawing of the TOF wall.

a schematic view of the TOF wall and drawing of a TOF counter. The TOF wall consists of 40 plastic scintillator bars (BC-408). The size of a plastic scintillator bar (TOF counter) is 200 cm long, 12 cm wide, and 4 cm thick. Two 2-inch PMT's (HAMAMATSU H7195) are attached to both sides through a light guide with a thickness of 3 cm. Each bar is overlapped with adjacent bars by 1 cm. Sideway bars are aligned in the planes tilted by $\pm$ 15 degrees as shown in the top view of Fig. 2.21. Ten bars are arranged in the right side and ten bars are placed in the left side. A 4-cm gap between the two TOF counters at the center allows for the photon beam to pass through. The TOF wall is movable on the rails between 1.5 and 4.5 m away from the center of the dipole magnet. In the present experiment, the z-position of the TOF wall was set at 3151.5 mm away from the center of the dipole magnet.

2.4.7 Dipole magnet

A dipole magnet is used as a momentum analyzer magnet to bend charged particles. The magnet is placed at the center of the spectrometer. The magnet has an aperture with 55 cm high and 135 cm wide. The length of the pole along the beam is 60 cm. Fig. 2.22 shows the

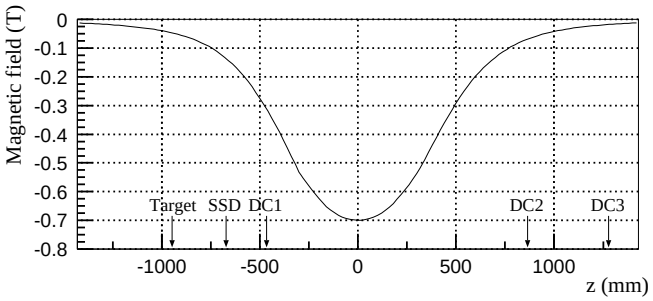

Figure 2.22: Distribution of the magnetic field B_y as a function of the z-position at x=0 and y=0. The position of z=0 corresponds to the center of the dipole magnet.

distribution of the magnetic field B_y along the y-direction as a function of the z-axis at x=0 and y=0. We used the TOSCA simulation program to obtain the distribution. The magnetic field was measured with a hole probe and the measured distribution was compared with the result obtained by the TOSCA simulation. They show a good agreement and then we used the distribution of the magnetic field obtained by TOSCA in the tracking. The direction of the magnetic field is from down to up. The strength of the magnetic field is 0.7 T (1.1 T) at the center when the current is set at 800 A (1510 A). The current was set at 800 A for the present experiment.

2.4.8 RF signal

The 508 MHz radio frequency (RF) system is used in the 8-GeV storage ring to recover the energy loss of circulating electrons due to synchrotron radiation. A time interval of the successive bunches of the RF to accelerate the electrons is 1.966 nsec. The RF signal is used to determine a start timing for the time-of-flight measurement. Fig. 2.23 shows a circuit diagram for the RF signals. The prescaler modules are 17K32 508-MHz 30 bit counters made by DIGITAL LABORATORY. The RF signals are prescaled with a factor 1/87. Three output logic signals are made. Two output signals are read by the FASTBUS TDC 1875S module and are used in the time-of-flight measurement. One output signal is delayed by 86 nsec relative to the other signal. The RF logic signal and the delayed signal are prepared to prevent the event loss due to the dead time of the trigger timing. The other signal from the prescaler with a factor 1/87 is read by the prescaler module with a prescale factor of 1/28. Three output signals are made. The two output signals are delayed by 1.8 μsec and 3.6 μsec relative to the other signal. These three signals are read by the FASTBUS TDC 1877A module. The data was used to study the accidental rate in the tagging system.

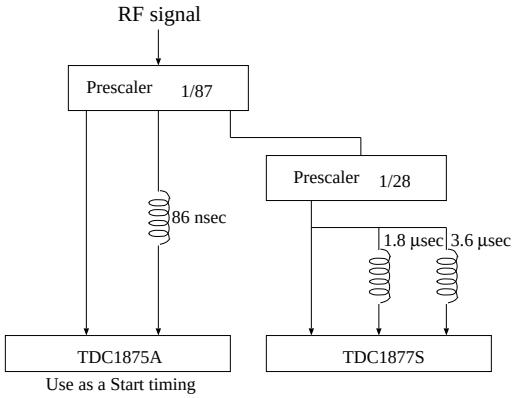

Figure 2.23: Circuit diagram for RF signals

2.5 The target

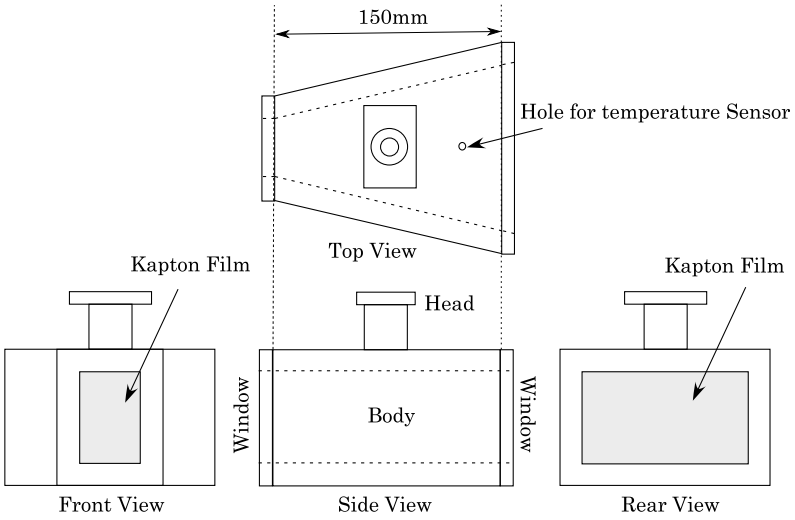

Figure 2.24: A schematic view of the target cell

A 150mm-long liquid hydrogen and deuterium target [59] was used in the experiment. The shape of the target cell is shown in Fig. 2.24. The inner size of the cell is about 660 cm^3. and The target cell was made of copper with a thickness of 8 mm. The entrance and exit windows of the target cell were made of Capton films with a thickness of 125 μm. The target was located at the 995 mm upstream of the center of the dipole magnet. The shape of the target cell was designed so that the target cell did not cut the acceptance of the charged particle spectrometer even when the reaction took place at the upstream of the target cell.

2.6 Electronics and Triggers

We used four types of modules to collect ADC and TDC data from the detectors. LeCroy

Table 2.3: Readout modules (digitizers) for detectors

Detector	ADC	TDC	used as trigger
TAG-PL	FERA	FASTBUS 1875A/1877S	TAG
TAG-SF	-	FASTBUS 1877S	TAG
UPveto	FERA	FASTBUS 1875A	UPveto
TRG	FERA	FASTBUS 1875A	TRG
AC	FERA	FASTBUS 1875A	AC
SVTX	Flash ADC	-	-
DC's	-	FASTBUS 1877S	-
TOF	FERA	FASTBUS 1875A	TOF (M≥1)
RF	-	FASTBUS 1875A/1877S	-

4300B FERA (Fast Encoding & Readout ADC) modules are used in the CAMAC system to read analog signals from the hodoscopes in the tagging system, the upstream-veto counter, the TRG, the AC and the TOF counters. The gate width of FERA modules was set 150 nsec. Flash ADC modules are used in the VME system to read analog signals from the silicon strip detectors in the SVTX. LeCroy FASTBUS 1877S TDC modules are used in the FASTBUS system to read the discriminated signals from the TAG-SFF and TAG-PL and the drift timing from the DC1, DC2 and DC3. The FASTBUS 1877S TDC module provides the time resolution of 0.5 nsec/channel and the 1 μsec dynamic range. LeCroy FASTBUS 1875A TDC modules are used in the FASTBUS system to read the discriminated signals from the TAG-PL, upstream-veto counter, the TRG, the AC and the TOF counters, and RF signals. The FASTBUS 1875A TDC module provides the timing resolution of 0.025 nsec/channel with the 100 nsec dynamic range. The modules used for a signal readout are summarized in Table 2.3.

Fig. 2.25 shows a readout diagram for the TAG, the upstream-veto counter, the TRG, the AC and TOF counters, and logic circuits for the trigger. The signals from the DC's and SSD's, and RF signals are not used in the trigger logic.

1. In the tagging system, OR signals from the TAG-PL and OR signals of TAG-SF are made. Then the AND signal of them are used in the trigger logic.

2. A logic signal from the upstream-veto counter is used as a veto signal.

3. A coincidence signal from both the PMT's of the TRG is used in the trigger logic. The coincidence signal supplies the common start for the FASTBUS 1875A TDC module and the common stop for the FASTBUS 1877S TDC module. The width of the coincidence signal was set 25 nsec.

4. An OR signal by four PMT's of the AC is used to make a veto signal for a trigger logic.

5. In the TOF system, a mean timing of the logic signals from the two PMT's of a TOF counter is made by a mean timer module (CAMAC C561). The signal from the mean timer module is read by the majority logic unit module 4532 (CAMAC). The signal of the multiplicity ≥ 1 was used in the trigger logic.

The hardware trigger signal was formed from the logic signals from the TAG, the UPveto, the TRG, the AC and the TOF counters. The UPveto and AC signals are used as veto signals. Fig. 2.26 shows a diagram of the trigger logic. We used two kinds of triggers defined as

$$\text{Hadron } trig. = TAG \cdot \overline{UPveto} \cdot TRG \cdot \overline{AC} \cdot TOF, \quad (2.12)$$

$$e^+e^- trig. = TAG \cdot \overline{UPveto} \cdot TRG \cdot TOF. \quad (2.13)$$

One is a hadron trigger to detect hadronic events with the AC veto signal. The other is an e^+e^- trigger to detect e^+e^- events without the AC veto signal. Since the rate of the e^+e^- trigger is too high to be taken by the DAQ system, the e^+e^- trigger signals are prescaled to be about 20% of the rate of the hadron trigger. The trigger timing is determined by the timing of the TRG and make the ADC gate signal, and TDC common start and stop signals.

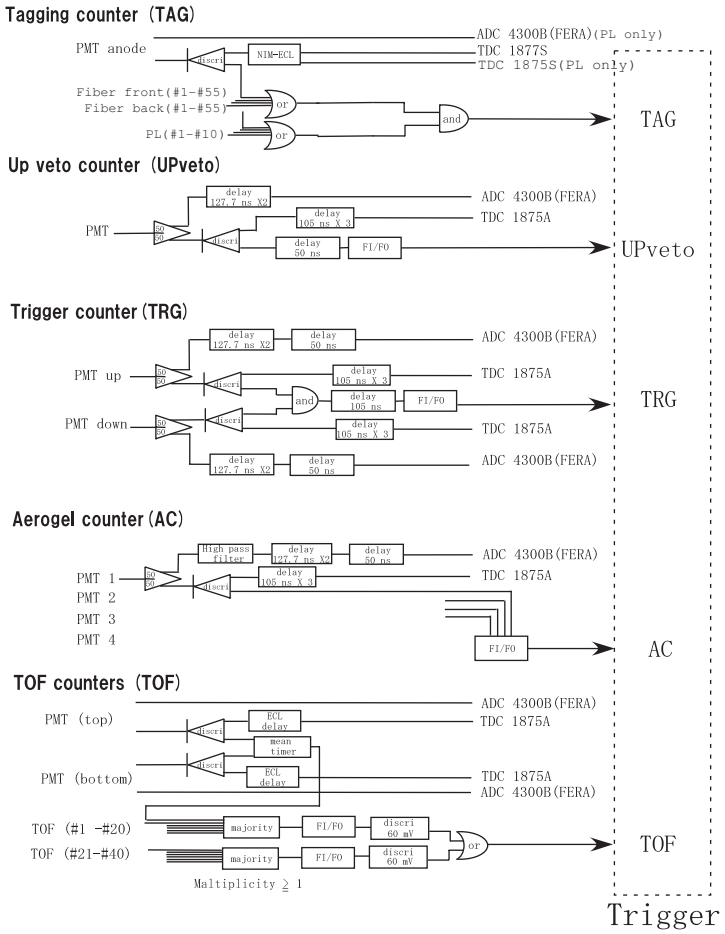

Figure 2.25: Diagram of the readout circuits for triggers.

2.7 Data summary

The experiment was performed from 2nd June in 2006 to 19th July in 2007. The total beam time was about 220 days. The data was taken with liquid hydrogen/deuterium (LH2/LD2)

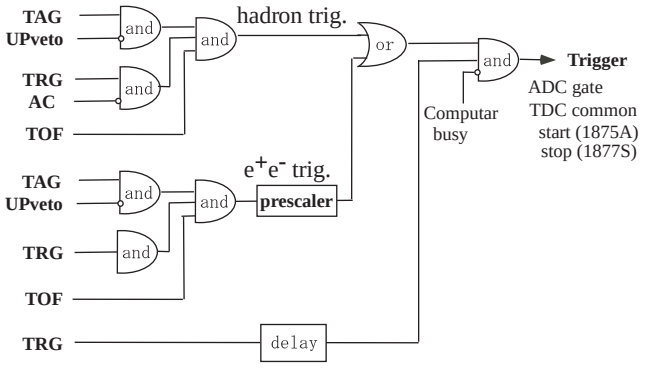

Figure 2.26: Diagram of the trigger logic for the hadron events.

target and lineally polarized photon beam. The averaged rate of the Tagger trigger was 1.5 MHz for vertically polarized beam and 1.2 MHz for horizontally polarized beam. The total number of accepted trigger and the total number of photons irradiated to the target for each target/polarization is summarized in table 2.4. Note that the number of photon is obtained by multiplying the transmission ratio from the collision point to the target (0.526) to the dead time corrected number of the Tagger trigger [60]. The data with no magnetic field and hadron trigger was taken in Dec in 2009 to perform the alignment of SVTX and DCs (section 3.3.4).

	Total number of trigger accepted	Total number of photons at the target
LH2(Hori/Vert)	$1.39 \times 10^8 / 1.15 \times 10^8$	$8.36 \times 10^{11} / 6.68 \times 10^{11}$
LD2(Hori/Vert)	$5.71 \times 10^8 / 5.56 \times 10^8$	$3.22 \times 10^{12} / 3.34 \times 10^{12}$

Table 2.4: Data summary

Chapter 3

Detector calibration

3.1 Difficulties of the calibration in the Θ^+ search.

The reaction of the interest is quasi-free production of the Θ^+ from neutron and its decay into the nK^+, $\gamma n \to K^-\Theta^+ \to K^-K^+n$. In this reaction, K^- has a larger momentum than the K^+ because K^- is produced at the initial vertex while K^+ is produced from the decay of the Θ^+. Therefore, the momentum calibration of the negative charged particles are important.

For the calibration of the positive charged particles, there are several good 'anchor' reactions such as $p(\gamma, K^+)\Lambda, \Sigma$ and $p(\gamma, \pi^+)n$. In the past calibrations of the momentum of the charged particles (including detector alignment) and photon energy largely relied on the $p(\gamma, K^+)\Lambda$ reaction. However, there is no good 'anchor' reaction for the calibration of negative charged particles. Therefore, we could be confident about the momentum calibration of the negative charged particles. To overcome the difficulty, new calibration method has been developed. Several corrections for the timing and xt-curve of the DCs are applied. The alignment of the DCs and SVTX has been done with reaction independent method by using no magnetic field run. The way to solve left-right ambiguity has been modified. The photon energy and global scale of the momentum has been determined with checking several reactions simultaneously. In this chapter, detail of these works are described. The evaluation of the detector performance and comparison of two data sets are also described.

3.2 Program codes

3.2.1 Analysis code: LEPSana

Raw data are processed by an analysis code called LEPSana, which has been developed by the LEPS collaboration. The digitized ADC and TDC data of the detectors are processed and the BCS photon beam energy, momenta, positions and masses of charged particles are extracted. The output of the program are written in NTUPLE format [62] and further analysis is done by processing output NTUPLE files in the physics analysis workstation (PAW) [63]. The calibration of the detectors and the determination of the parameters have been done beforehand.

3.2.2 Monte Carlo simulation code: g3leps

The acceptance of the LEPS spectrometer, the resolution of the physical values are studied by a Monte Carlo simulation (MC) code, g3leps. The g3leps has been developed by the LEPS collaboration, and which is based on the CERN library [64] including GEANT 3.21 [65]. It simulates a generation of particles from the specific reaction, processes during passage of the particles through the experimental apparatus taking into account decay in flight, energy loss, multiple scattering of the particles. The GHEISHA package was used to simulate hadronic interactions. The measured resolution and efficiency of the silicon strip vertex detector (SVTX) and the drift chambers, timing resolution of the TOF wall counters are implemented in g3leps. A realistic beam shape of the polarized BCS photon beam, and its resolution are implemented. Generated data of the events by the simulation code are analyzed in the exactly same way as the real data by the LEPSana. The output of the program are also written in NTUPLE format [66].

3.3 Drift chambers and SVTX

In this section, several modifications of the calibration method for DCs and SVTX from previous method [58] are described.

3.3.1 Corrections for the drift time

Time walk effect of the trigger counter

The trigger timing of LEPS experiment is determined by the TRG. The timing of the discriminated signal depends on the pulse height. The timing of an output signal becomes early as a pulse height becomes large (time walk). The time walk of the TRG affects the timing of all the counters including DCs with the same magnitude. The effect of the time walk of the TRG to DCs can be removed by subtracting the TDC of the RF from TDC of DCs because the timing resolution of the RF is very good (12ps). Figure 3.1 shows the TDC of one specific wire of DC with and without subtraction of the TDC of the RF. Note that the early timing corresponds to large TDC channel because TDC module 1877S is operated with common stop mode. The tail component near t0 is reduced by the subtraction of the TDC of the RF.

Hit position at the sense wire dependence

The distance from the hit position at the sense wire to the preamplifier depends on the hit position. Figure 3.2 shows the TDC spectrum of DC2. Black histogram is for Y position at DC2$\leq$-250 mm and red one is for Y position at DC2$\geq$250 mm, respectively. Clear difference of the t0 position is seen. The preamplifier is put at the top of DCs. Therefore, the t0 timing is earlier for latter case. The correction of the drift time is applied by assuming that the velocity of the signal is equal to the speed of light.

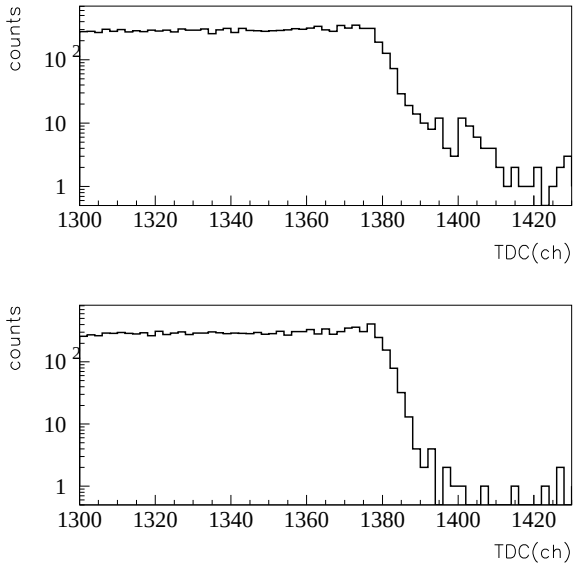

Figure 3.1: TDC of one specific wire of the DC1. Top plot is before subtracting the TDC of the RF and bottom plot is after subtracting the TDC of the RF.

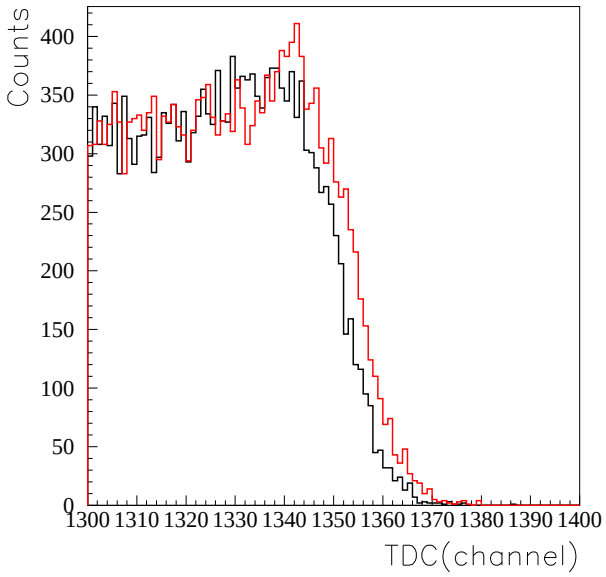

Figure 3.2: TDC of the DC2X1 plane. Black histogram is for $YDC2 \leq -250$ and red one is for $YDC2 \geq 250$, respectively.

Time of flight

The arrival timing of a charged particles at the DCs depends on its velocity. The distance from the TRG to the DC3 is about 2000 mm. Therefore, the time difference between a charged particle which has the same velocity as the photon and a charged particle which has the same momentum with mass (a Kaon with the momentum of 0.5 GeV/c) is around 2.5 ns. 2.5 ns corresponds to the drift distance of around 0.125 mm which is not small enough to be ignored. Figure 3.3 shows the TDC spectrum of the DC3 for low ($p \leq 0.8$) and high ($p \geq 1.2$) momentum protons. Clear difference of the t0 position is seen. The drift time is corrected by using the time of flight measurement.

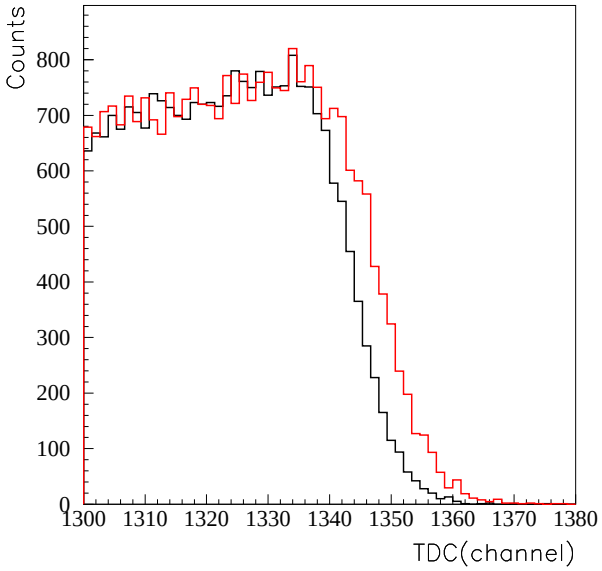

Figure 3.3: TDC of the DC3X1 plane. Black histogram is for proton tracks with $p \leq 0.8$ and red one is for proton tracks with $p \geq 1.2$, respectively.

Improvement of the position resolution by the timing corrections

Figure 3.4 shows the residuals of DC. Black line is with timing correction and red line is without timing correction. The plane which residual is plotted is not used in the tracking. For red lines, timing correction is implemented for the plane other than residual is plotted. Therefore, the difference of the residual purely comes from the position resolution of the plane which residual is plotted. Clear improvement of the position resolution is seen. σ of each histogram is summarized in table 3.1. The smearing of the position by ignoring these timing correction is around 100 μm.

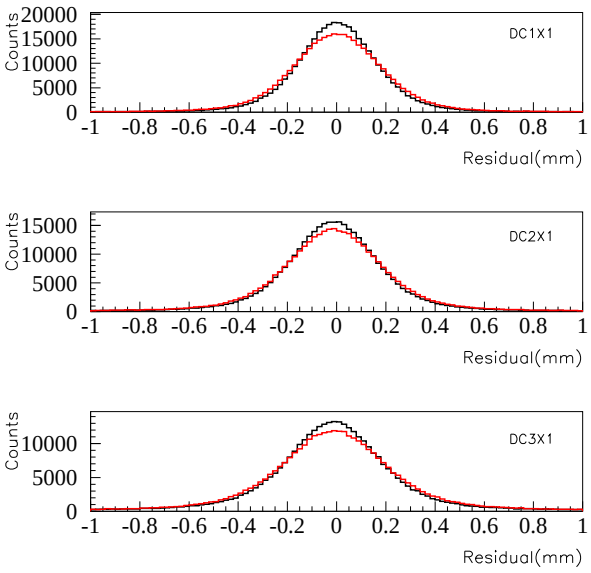

Figure 3.4: Residuals. Black line is with timing corrections and red line is without timing corrections. The plane which residual is plotted is not used in the tracking.

	$\sigma_{w/o}$ (mm)	σ_w (mm)	$\sqrt{\sigma_{w/o}^2 - \sigma_w^2}$ (mm)
DC1X1	0.191	0.169	0.090
DC2X2	0.213	0.194	0.088
DC3X2	0.245	0.221	0.107

Table 3.1: Summary of σ of residuals shown in Fig.3.4. σ_w is σ for the residuals with timing corrections. $\sigma_{w/o}$ is σ for the residuals without timing corrections.

3.3.2 xt-curve

A relation between a drift time and a drift distance is called xt-curve. In this section, several modifications for the calibration of the xt-curve is described.

Difference of the xt-curve between left and right

Figure 3.5 shows a schematic view of the charged tracks which pass through a left side or a right side of a sense wire. As shown in the figure, the distance from a shield wire is different for two tracks. Therefore, the difference of the xt-curve between left and right is expected. Furthermore, the difference is expected to depends on the incident angle of the charged particles because the difference of the distance from a shield wire becomes large as the incident angle becomes large. These expectations are checked by real data.

Figure 3.6 shows the mean of the residual of DC2X as a function of the drift distance for left and right. The xt-curve determined by existing method (the same xt-curve is used for left and right) is used. The incident angle dx/dz is $0.1 \leq dx/dz \leq 0.2$. The definition of the residual in Fig. 3.6 is

$$res_L = L_m - L_t, \tag{3.1}$$

where L_m is the measured drift length and L_t is the drift length estimated by a track. res_L is used when we check xt-curve or t0 of DCs. Another choice of the residual(res_x) is

$$res_x = x_m - x_t, \tag{3.2}$$

where x_m is measured x-position and x_t is estimated x-position by a track. res_x is used when we check alignment etc. res_x and res_L is the same when a charged track passes through a right side of a sense wire. The sign of res_x and res_L is opposite when a charged track passes through a left side of a sense. As shown in the bottom left plot of Fig. 3.5, the difference of the mean of the residual of left and right is not flat as a function of the drift distance. The fact indicates that the xt-curve is different for left and right (note that if the difference is not zero but it is flat as a function of the drift distance, it indicates that the mean of the res_x is not zero). Figure 3.7 shows the same plots as Fig. 3.6 but the angle dx/dz is $0.2 \leq dx/dz \leq 0.3$. The difference of left and right becomes larger as expected.

Symmetry properties of xt-curve

From the wire configuration of the DCs, following symmetry properties of the xt-curve are expected.

1. The xt-curve is the same for left-X1 with the incident angle=θ and right-X2 with the incident angle=θ. Note that the electric voltage for X1 and X2 (also for U1 and U2) is the same for whole run period.

2. The xt-curve is the same for left-X1 with the incident angle=θ and right-X1 with the incident angle=$-\theta$.

From bottom left plot of Fig. 3.6, The difference of the mean of the residual between left and right is symmetric for DC2X1 and DC2X2. The fact is consistent with symmetry property

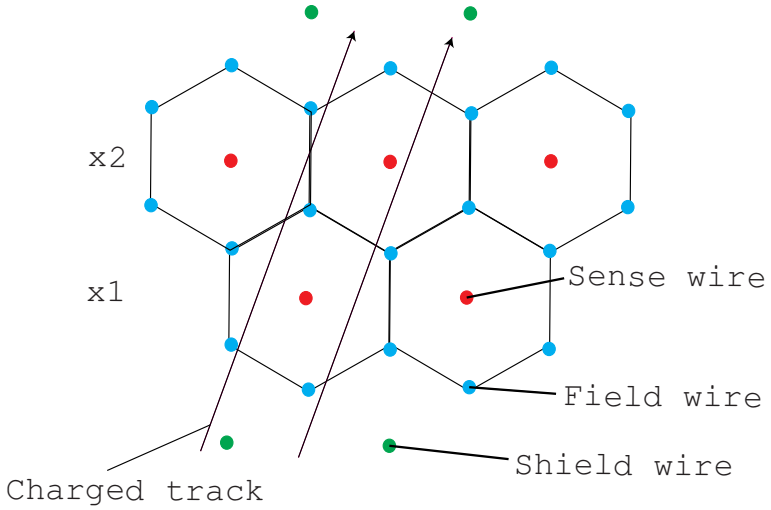

Figure 3.5: A schematic view of the charged tracks which pass through the DC.

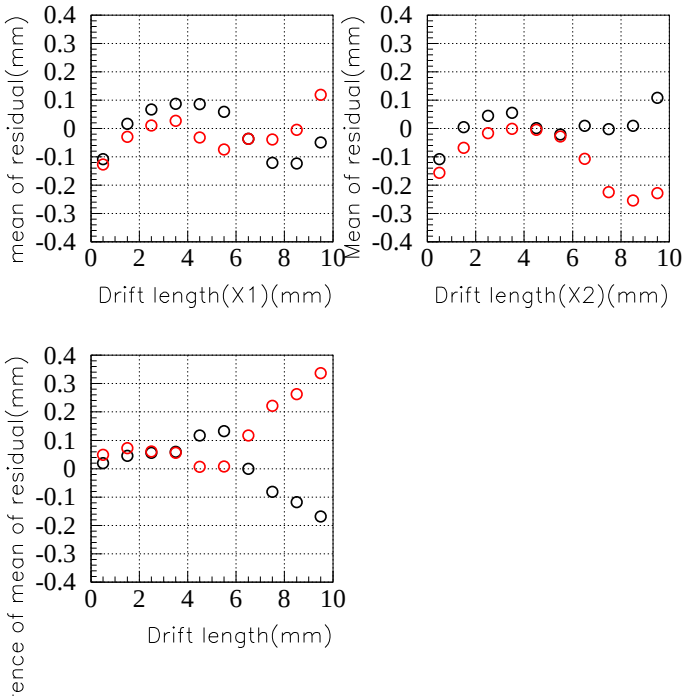

Figure 3.6: Top left: The mean of the residual of DC2X1 plane as a function of the drift distance. Black points are for left and red points are for right. Top right: The mean of the residual of DC2X2 plane as a function of the drift distance. Black points are for left and red points are for right. Bottom left: The difference of the mean of the residual of left and right as a function of the drift distance. Black points are for DC2X1 plane and red points are for DC2X2 plane. The angles dx/dz of charged particles are $0.1 \leq dx/dz \leq 0.2$. DC2X1 and DC2X2 planes are not used in the tracking.

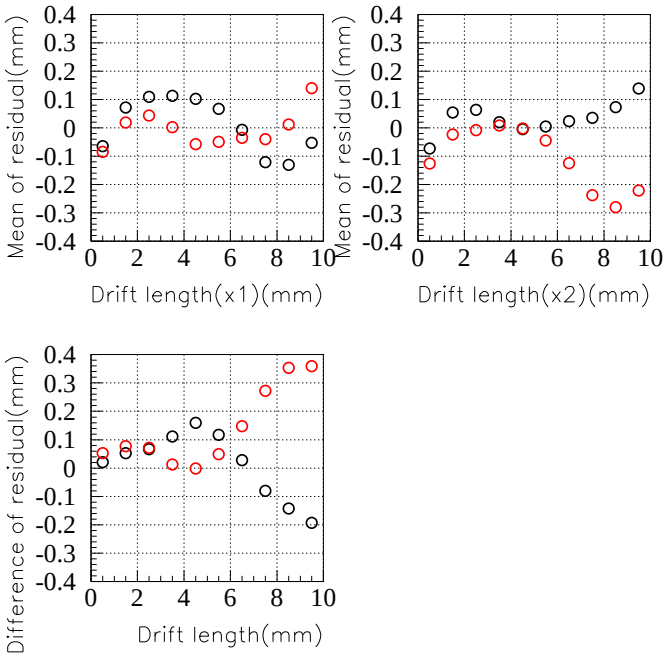

Figure 3.7: The same figure as Fig. 3.6 but the incident angle dx/dz is 0.2≤dx/dz≤0.3.

1. Figure 3.8 shows the same plot as Fig. 3.6 but the angle dx/dz is -0.2≤dx/dz≤-0.1. The difference of the mean of the residual between left and right is opposite when compared with Fig. 3.6. The fact is consistent with symmetry property 2. By combining property 1 and 2, the xt-curve is the same for left-X1 with the incident angle=θ, right-X1 with the incident angle=$-\theta$, right-X2 with the incident angle=θ, and left-X2 with the incident angle=$-\theta$.

Actual xt-curve determination procedure

The tracking is applied without the plane which we want to determine the xt-curve. The drift distance of the plane is estimated by the track as a function of the drift time. The xt-curve for each incident angle, left-right, and plane are determined individually. The xt-curve is defined as

$$x_{drift} = c_1 t_{drift} + c_2 t_{drift}^2 + c_3 t_{drift}^3 + c_4 t_{drift}^4, \tag{3.3}$$

where x_{drift} is the drift distance and t_{drift} is drift time and c_1, c_2, c_3, and c_4 is the parameters for the xt-curve. Then, the average of the xt-curves are taken for the angle, left-right and planes whose xt-curves are expected to be same from symmetry properties.

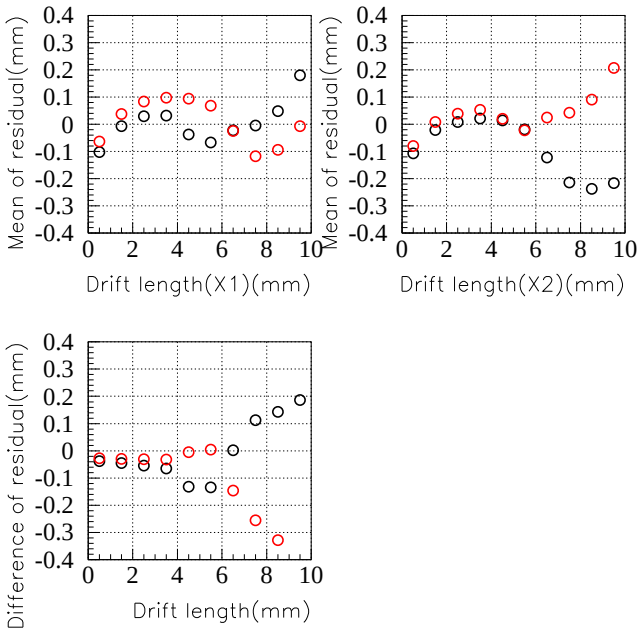

Figure 3.8: The same figures as Fig. 3.6 but the incident angle dx/dz is -0.2≤dx/dz≤-0.1.

3.3.3 Position resolution of DCs

The method to obtain the position resolution of DCs

Existing method to obtain the position resolution uses the line fitting of SVTX-DC1 or DC2-DC3. However, the line fitting is an approximated way because magnetic field exist. Therefore, new method to obtain the position resolution is developed. The width of the residual of X1 plane in the tracking when both X1 and X2 planes are not used in the tracking (σ_{res}) is written as

$$\sigma_{res} = \sqrt{\sigma_{x1}^2 + \sigma_{track}^2}. \tag{3.4}$$

where σ_{x1} is the intrinsic resolution of X1 plane which we want to obtain and σ_{track} is the width come from the track. Figure 3.9 shows the scatter plot of the residual of DC2X1 and DC2X2 planes. Both planes are not used in the tracking. Clear correlation is seen. The origin of the correlation is incorrect estimation of the position at the planes by a track which is common to both planes. Therefore, by taking the difference of the residual of X1 and X2 planes event by event, the contribution to the width from tracks can be removed.

The width of the difference (σ_{diff}) can be written as

$$\sigma_{diff} = \sqrt{\sigma_{x1}^2 + \sigma_{x2}^2} \tag{3.5}$$

where σ_{x2} is the intrinsic resolution of X2 plane.

By assuming that the position resolution is the same for X1 and X2 planes, σ_{diff} can be

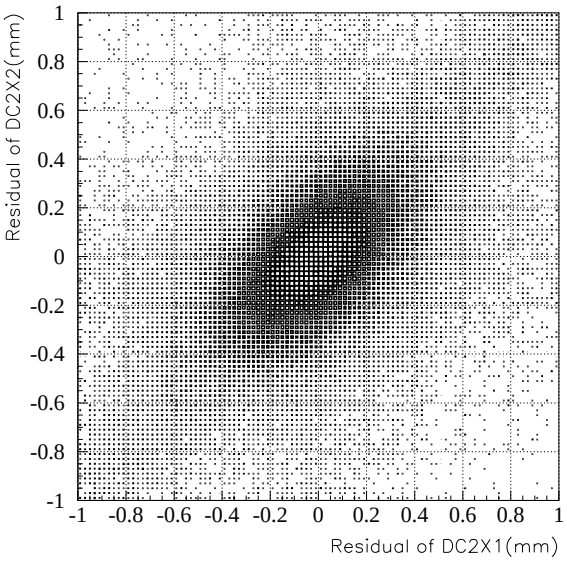

Figure 3.9: Scatter plot of the residual of DC2X1 and DC2X2 planes. Both planes are not used in the tracking.

written as

$$\sigma_{diff} = \sqrt{2}\sigma_{x1}. \tag{3.6}$$

The intrinsic resolution is obtained by dividing σ_{diff} by $\sqrt{2}$. Note that the position resolution of v-plane can not be obtained by the method because one chamber has only one v-plane. The position resolution of v-plane is obtained by estimating σ_{track} from simulation and subtract it from σ_{res}.

Comparison of the two methods

Table 3.2 shows the comparison of the position resolutions obtained by two methods. Note that xt-curve is old one (left and right is the same). The resolution of DC1 is overestimated for old method. This is because DC1 is closer to dipole magnet than DC2 and DC3 and effect of ignoring dipole magnet is large. The performance of the DCs can not be fully derived if the position resolution used to obtain the χ^2 of the tracking is not correct. Figure 3.10 shows the $MMp(\gamma, K^+)X$ spectrum for new and old position resolution. Only the position resolution to obtain χ^2 of the tracking is different. The missing mass resolution is improved by around 3% by using the position resolution obtained by new method.

Position resolution by using new xt-curve

Table 3.3 shows the position resolution of DCs by using new xt-curve.

The position resolution of DC2X1 plane as a function of the incident angle (dx/dz) is shown in Fig. 3.11. The incident angle dependence of the position resolution is small.

plane	Resolution (old method) (mm)	Resolution (new method) (mm)
DC1X1	0.214	0.160
DC1X2	0.208	0.160
DC1X3	0.218	0.173
DC1U1	0.194	0.158
DC1U2	0.184	0.158
DC1V	0.228	0.225
DC2X1	0.172	0.188
DC2X2	0.171	0.188
DC2U1	0.181	0.192
DC2U2	0.181	0.192
DC2V	0.303	0.329
DC3X1	0.190	0.210
DC3X2	0.189	0.210
DC3U1	0.201	0.198
DC3U2	0.187	0.198
DC3V	0.274	0.311

Table 3.2: Position resolution of DCs for two methods.

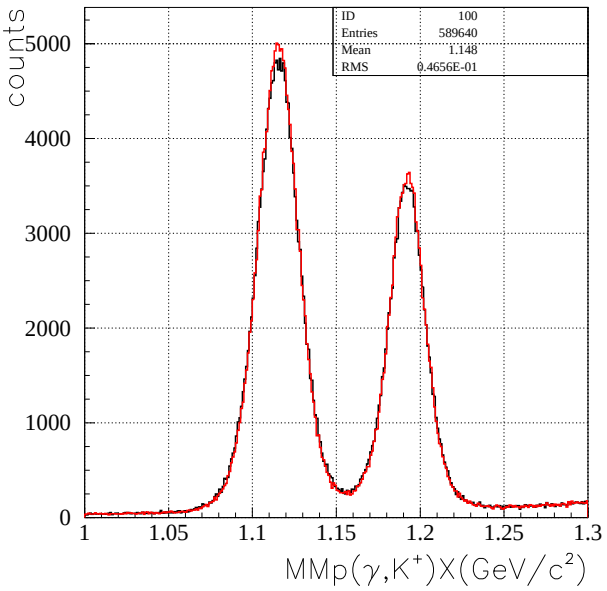

Figure 3.10: $MMp(\gamma, K^+)X$ spectrum. Black: Position resolution obtained by old method is used. Red : Position resolution obtained by new method is used. Old xt-curve is used for both spectrum.

Plane	Resolution (mm)
DC1X1	0.143
DC1X2	0.143
DC1X3	0.145
DC1U1	0.141
DC1U2	0.141
DC1V	0.178
DC2X1	0.146
DC2X2	0.146
DC2U1	0.147
DC2U2	0.147
DC2V	0.331
DC3X1	0.153
DC3X2	0.153
DC3U1	0.146
DC3U2	0.146
DC3V	0.258

Table 3.3: Position resolution of DCs by using new xt-curve.

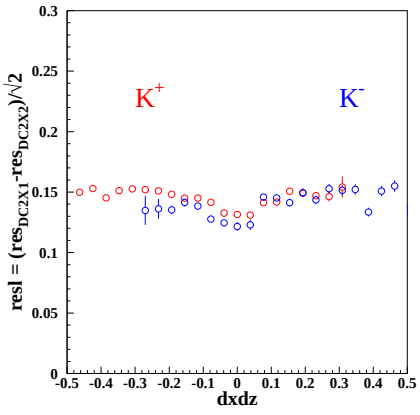

Figure 3.11: Position resolution of the DC2X1 plane as a function of dx/dz.

3.3.4 Alignment of SVTX and DCs

Problems on the existing alignment method

The layer of the SVTX used to measure the x-direction consists of eight modules. The configuration of the SVTX module ID is shown in Fig. 3.12. Since each module is mounted individually, the alignment should be done for each module. In the existing method, the alignment of the each SVTX module had been done using $\gamma + p \rightarrow K^+\Lambda$ reaction. The SVTX is aligned for the peak position of the missing mass $MMp(\gamma, K^+)\Lambda$ to be close to the PDG value of the mass of the Λ. However, there are several problems on this method.

Figure 3.13 shows the peak position of MMp(γ,K^+)Λ as a function of the y position of the SVTX (y0). A strong y0 dependence is seen when hits in SVTX are not used in the tracking. The y0 dependence disappeared when the hits in SVTX are included. Figure 3.14 shows the mean of the residual of SVTX (x-direction) for each module (the configuration of the SVTX module is shown in Fig. 3.12) and for each charge. The SVTX hits are not used in the tracking. The sign of the mean of the residual is opposite for top (1-4) and bottom (5-8) modules. To cancel out the y0 dependence, the correction from SVTX is opposite for top and bottom modules. The mean of the residual is different for positive and negative charged particles.

The alignment method is not reasonable because the y0 dependence itself is not related with the SVTX. Furthermore, as the SVTX positions are determined by the missing mass of positive charged particles (K^+), the momentum calibration for the negative charged particles may not be correct (we are interested in high momentum K^- events).

A strong y0 dependence indicates that a drift chamber is rotated in the z-axis. When a drift chamber is rotated in the z-axis, deviation of the x-position (δx) is written as

$$x' = xcos\theta - ysin\theta \simeq x - y\theta \tag{3.7}$$

$$\delta x = x - x' \simeq y\theta \tag{3.8}$$

where θ is a rotation angle.

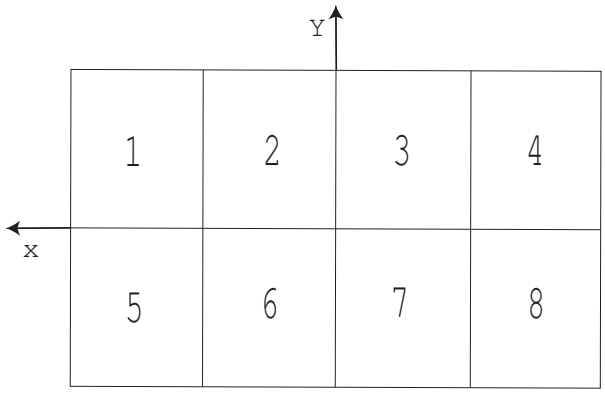

Figure 3.12: The Configuration of the SVTX module. The numbers show the module ID.

There is another problem on the SVTX alignment. Figure 3.15 shows the peak position of $MMp(\gamma, K^+)\Lambda$ as a function of x position of SVTX (note that scale of y-axis is smaller than

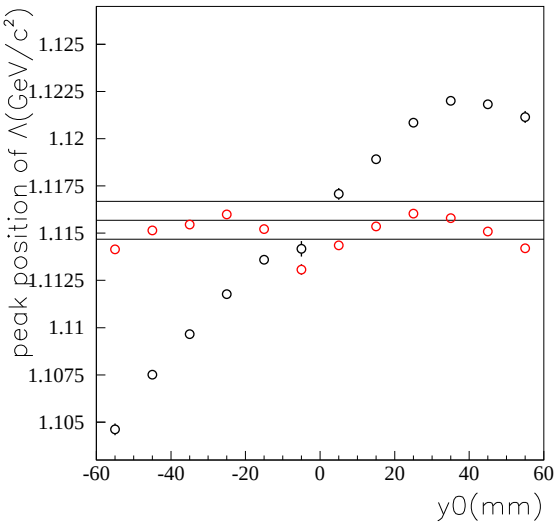

Figure 3.13: The peak position of $MMp(\gamma, K^+)\Lambda$ as a function of the y position of the SVTX. Black points show the result without the SVTX hits. Red points show the result with the SVTX hits. Horizontal lines show the PDG value of the mass of $\Lambda \pm 1 MeV/c^2$.

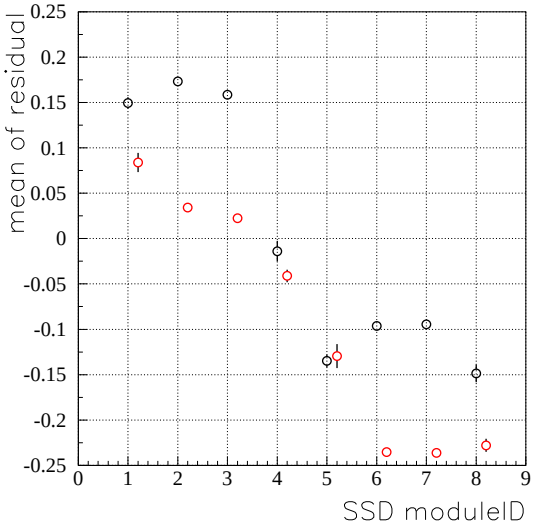

Figure 3.14: The mean of the residual of the SVTX (x-direction) as a function of the SVTX module ID. The hits in SVTX are not used in the tracking. Black points are for K^+ tracks and red points are for K^- tracks.

that of the y0 dependence). When the SVTX is included in the tracking, the peak position becomes discontinuous at the boundaries of SVTX modules. Figure 3.16 shows the mean of the residual of the SVTX as a function of the x0. The residual is also discontinuous at the boundaries of the SVTX modules. These behaviors are explained by a z-shift of the SVTX as described in the following section. In summary, following problems exist in the alignment of the SVTX and the DCs.

- The SVTX alignment is done by using K^+ events in $\gamma p \to K^+\Lambda$ reaction The alignment should be done with a reaction independent way.
- The DCs seem to be rotated in the z-axis and the SVTX is aligned to cancel out it. Alignment of the DCs should be corrected by the DCs itself.
- The x0 dependence of the peak position of $MMp(\gamma, K^+)\Lambda$ is discontinuous when the SVTX is included in the tracking. The mean of the residual is also discontinuous.

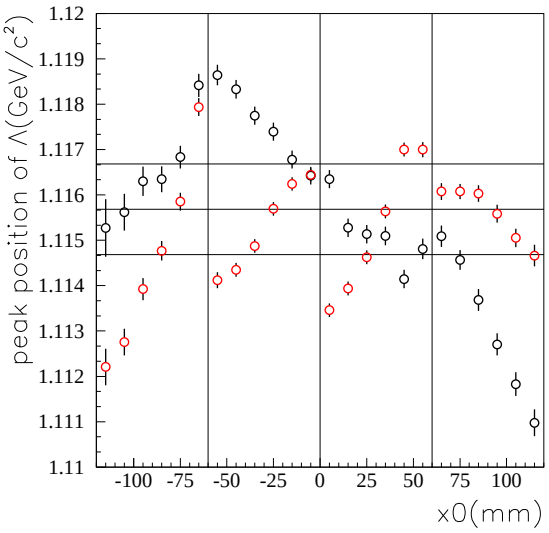

Figure 3.15: The peak position of $MMp(\gamma, K^+)\Lambda$ as a function of the x0. Black points show the result without the SVTX hits. Red points show the result with SVTX hits. Vertical lines show the boundaries of the SVTX modules. Horizontal lines show the PDG value of the mass of $\Lambda \pm 1 MeV/c^2$.

The alignment using no magnetic field data with hadron trigger

To perform the alignment more precisely, the data with no magnetic field, and the hadron trigger were taken in Dec. 2009. No magnetic field data with the e^+e^- trigger were taken in 2006-2007. However, the rotation parameters can not be determined by using e^+e^- data because e^+e^- events hits only center regions. Furthermore, the alignment parameters of the

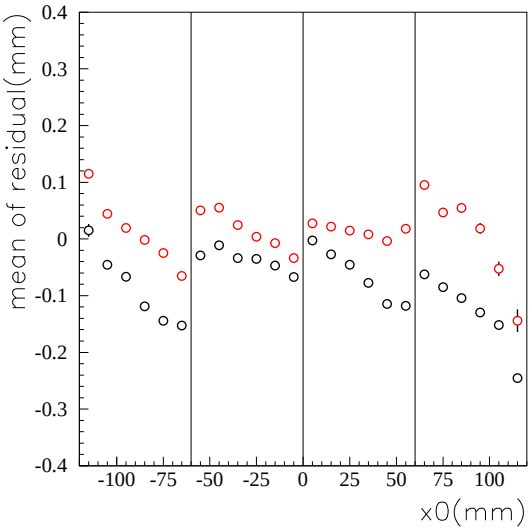

Figure 3.16: The mean of the residual of the SVTX (x-direction) as a function of the x-position of the SVTX (x0). The SVTX hits are not used in the tracking. Black points are for K^+ tracks and red points are for K^- tracks. Vertical lines show the boundaries of SVTX modules.

peripheral SVTX modules can not be determined by using e^+e^- events for the same reason. Therefore, the data with hadron trigger is useful for the alignment. The trigger condition is

$$Tag \cdot \overline{UPveto} \cdot STC \cdot \overline{AC} \cdot TOF \cdot \overline{RATE} \tag{3.9}$$

where RATE is a rate monitor which is placed on the beam line just behinds the TOF wall from 2009. RATE is added to the trigger because in 2009, the index of aerogel Cerenkov counter was 1.01 and veto rate was not good. Figure 3.17 shows the mean of the residual of DC2X1 plane as a function of the y position of DC2. The line fitting is done with DC1 and DC3. A strong and linear y dependence is seen and suggests rotation of DCs.

In general, four detectors are necessary to determine each rotation (and also global alignment) parameter. For example, from Fig. 3.17, it is not clear which chamber is rotated. If SVTX is added, by a tracking of SVTX and DC1, a relative angle between DC2 and DC3 can be determined. Actual parameter determination is done with the following procedure.

- The SVTX alignment is done from the line fitting of DC1,DC2,DC3. The alignment means to determine x,y,z,θ_x,θ_y,θ_z for each module.
- Three combinations of the line fitting are done. Three means 1.SVTX-DC1, 2.SVTX-DC2, 3.SVTX-DC3
- For example, rotation angle of DC1 is determined as $(\theta_2+\theta_3)/2$, where θ_2 is rotation angle determined from case2 and θ_3 is that from case3. rotation parameter of DC2 and

DC3 is determined as the same way. Each rotation angle is obtained from the slope of the y-dependence of the mean of the residual.

- These procedures are iterated until parameters converge.

The relative rotation angle of each detectors can be determined by this method. However, the global rotation angle can not be determined. The rotation angle of the DC3X1 was measured and the result was about 200 μradian. So all the counters are rotated with the same magnitude so that the rotation angle of DC3X1 becomes 200 μradian after applying the method written above. Note that the global rotation parameter does not affect to the momentum measurement. The alignment parameters are summarized in appendix.

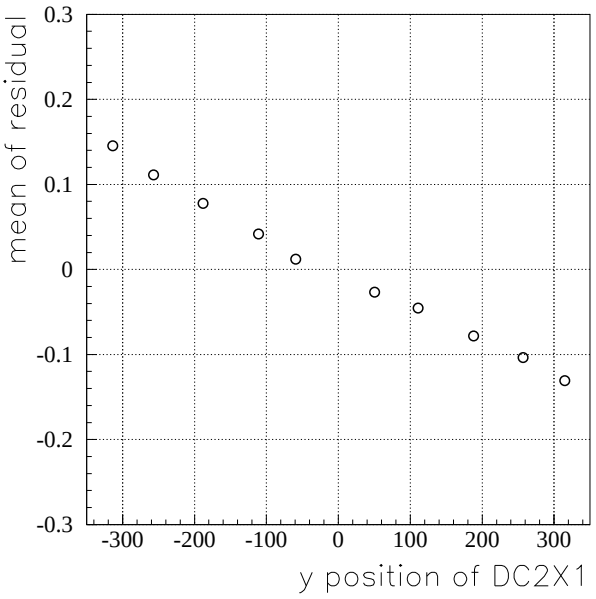

Figure 3.17: The mean of the residual of DC2X1 plane as a function of the y position of DC2 for no magnetic field run. The line fitting is done with DC1 and DC3.

Evaluation of the rotation parameter of DCs

Figure 3.18 shows the y0 dependence of the peak position of $MMp(\gamma, K^+)\Lambda$ after including rotation of DC. The SVTX hits are not used in the tracking. The y0 dependence becomes very small (the linear component is almost completely disappeared). I want to emphasis that to determine the rotation parameters, information of the missing mass is not used at all. A small dependence remained is understood to be due to incompleteness of the magnetic field map, which is described in the following section.

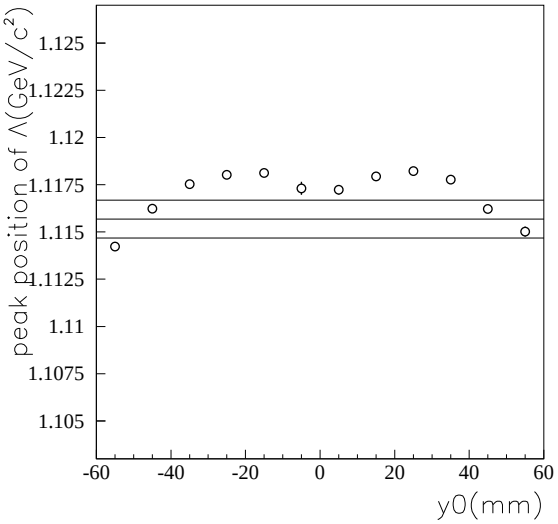

Figure 3.18: The peak position of the $MMp(\gamma, K^+)\Lambda$ as a function of the y0. The SVTX hits are not used in the tracking and the rotation of the DC is included. Horizontal lines show the PDG value of the mass of $\Lambda \pm 1MeV/c^2$.

3.3.5 Evaluation of SVTX alignment parameter

Figure 3.19 shows the mean of the residual of the SVTX as a function of the x0 for the data taken in 2009 (just before the no magnetic field run). The SVTX alignment parameters determined by using the no magnetic field data is used.

Note that the x0 dependence of the mean of the residual is almost 0 for all the x0 region for no magnetic field run as shown in Fig. 3.20. So the plot suggests that there exist some inconsistencies between no magnetic field run and normal run. The mean of the residual is continuous at the boundaries of the SVTX modules. The continuity shows that the relative position of each SVTX module is correct.

Figure 3.21 shows the mean of the residual of the SVTX as a function of the x0 for the data taken in 2006-2007. The SVTX alignment parameters and DC rotation parameters determined by using the no magnetic field data is used. The residual becomes continuous (compare with Fig. 3.16). Although the relative position of each SVTX module does not change between 2006-2007 and 2009B, the slope of the x0 dependence becomes very large when compared with the data taken in 2009B. A large slope of x0 dependence indicates that the z-position of the SVTX is different between two data sets. When z-position is shifted (δz), effective shift of the x-position (δx) is written as

$$\delta x = dx/dz \cdot \delta z \tag{3.10}$$

where dx/dz is the angle at the SVTX. The x0 and the dx/dz is strongly correlated. In fact, the difference of two data sets is explained by a 0.7 mm shift of the z-position of SVTX. Figure 3.22 shows the mean of the same plot as Fig. 3.21 but the z shift of 0.7 mm is implemented.

The discontinuity seen in Fig. 3.16 happened because this z-shift is corrected by x-shift for each module. The z-shift is implemented in 06-07 data. Figure 3.23 shows the x0 dependence of the peak position of $MMp(\gamma, K^+)\Lambda$ after all the alignment items are included. The peak position is continuous at the boundaries of the SVTX module and the dependence itself becomes small comparing with the result of no SVTX case (black points of Fig. 3.15).

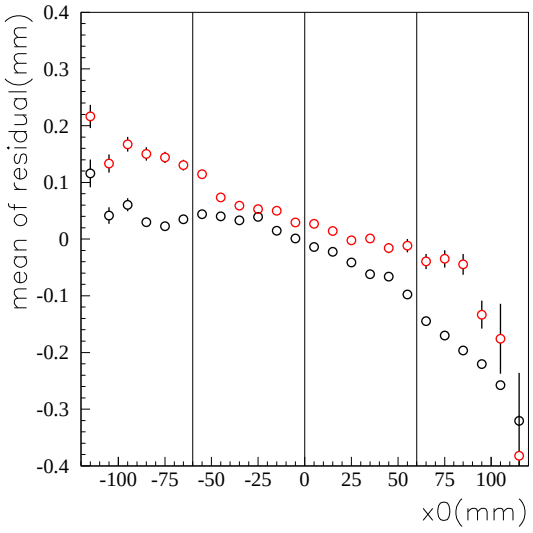

Figure 3.19: The mean of the residual of the SVTX as a function of the x0 for the data taken in 2009B. Black points are for K^+ tracks and red points are for K^- tracks. Vertical lines show the boundaries of SVTX modules.

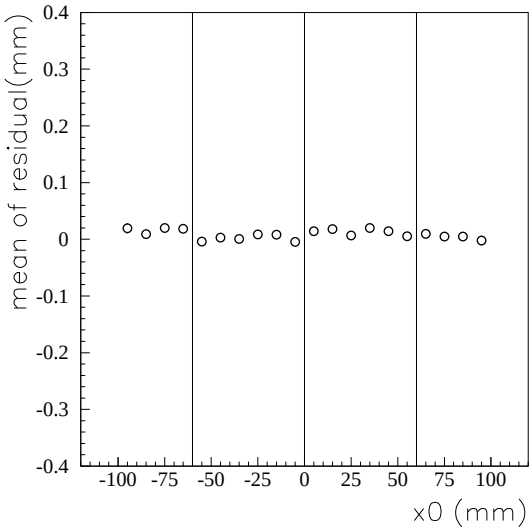

Figure 3.20: The mean of the residual of the SVTX as a function of the x0 for no magnetic field run. Vertical lines show the boundaries of SVTX modules.

3.4 Solving left-right ambiguity with full tracking

It is necessary to determine whether charged particles pass a left side or a right side of a sense wire in DCs (left-right ambiguity). The ambiguity was solved by the line fitting with SSD-DC1 or DC2-DC3 in the existing LEPSana. The line fitting was applied for all the combinations of left-right in each wire. The combination with the minimum χ^2 of the fitting is selected. However, the line fitting is an approximated way because the magnetic field exists.

Figure 3.24 shows the drift distance of DC1X1 for each charge. The dip structures are seen near wires (at zero). The dip structure is seen in all the planes. The dip position is opposite for positive and negative charged particles. The top and bottom plot in Fig. 3.25 show the drift distance of positive charged particles with a low and high momentum, respectively. The dip structure for low momentum particles is larger than that for high momentum particles. The dip structure is caused by the miss-identification of a left-right ambiguity because such planes are removed as outliers and not used in the tracking. The reason of the miss-identification is to ignore the effect of the magnetic field when a left-right ambiguity is solved by using the line

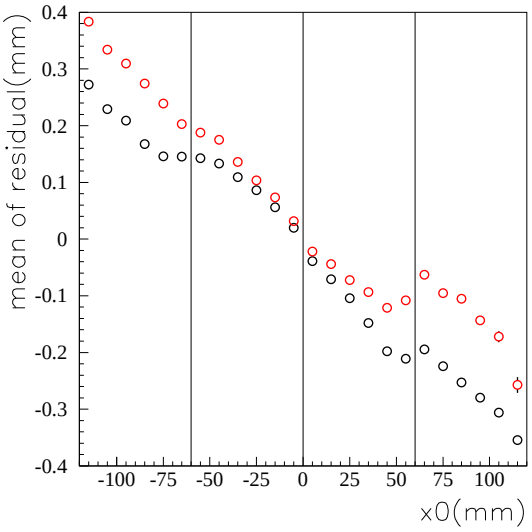

Figure 3.21: The mean of the residual of the SVTX as a function of the x0 for the data taken in 2006-2007. Black points are for K^+ tracks and red points are for K^- tracks. Vertical lines show the boundaries of SVTX modules.

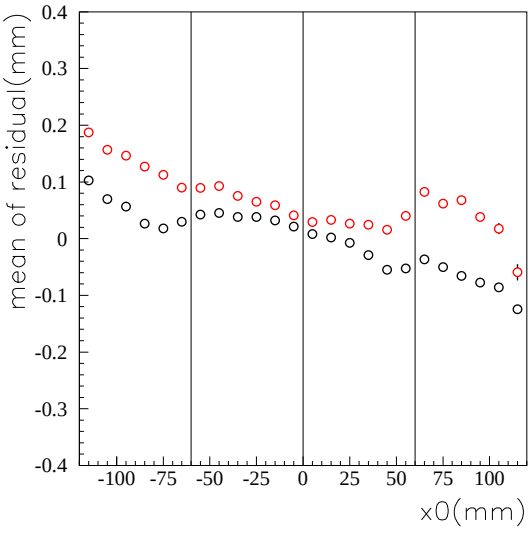

Figure 3.22: The mean of the residual of the SVTX as a function of the x0 for the data taken in 2006-2007. Black points are for K^+ tracks and red points are for K^- tracks. z-shift of 0.7mm is implemented. Vertical lines show the boundaries of SVTX modules.

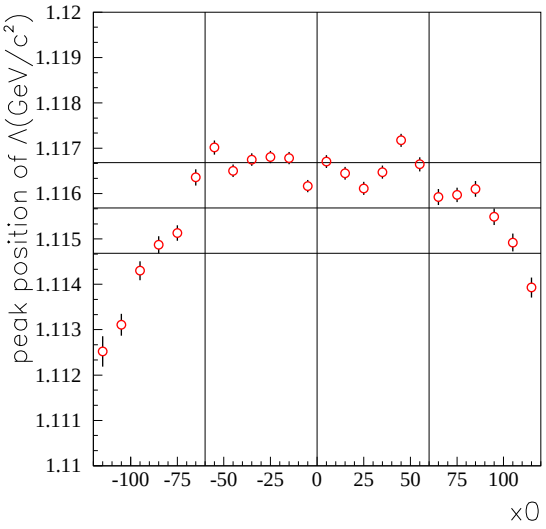

Figure 3.23: The peak position of the $MMp(\gamma, K^+)\Lambda$ as a function of the x0 for the data taken in 2006-2007. The SVTX alignment parameter determined by no magnetic field data is used and z-shift of 0.7mm is also included. Horizontal lines show the PDG value of the mass of $\Lambda \pm 1 MeV/c^2$.

fitting. The effect of the magnetic field is opposite for positive and negative charged particles, and larger for low momentum particles than high momentum particles.

To reduce the miss-identification of the left-right ambiguity, LEPSana is modified to solve the left-right ambiguity with the full-tracking. If the full-tracking is applied for all the combinations, it takes too much computation time. Therefore, we have two steps. In the first step, the line fitting is done for all combinations and select the best combination as existing LEPSana. In the second step, hits with a small drift distance ($\leq$2 mm) are selected, then the full tracking is applied with the opposite sign of the original sign by the line fitting. If χ^2 is smaller for a opposite sign, it is adopted.

Figure 3.26 shows the drift distance for each charge after the modification (compare with Fig. 3.24). The dip structure disappeared. Figure 3.27 shows the comparison of the number of outliers. The number of outliers decreased after the modification.

3.5 Photon energy and momentum of charged tracks

3.5.1 Hit position in the tagger

Selection of the true tagger hits

The hits in TAG-SF and TAG-PL which are associated with the triggered event are selected by the TDC information (TDC 1877S is used at this stage). The hits with the TDC value of t0 $\pm$ 30 channel ($\pm$15 ns) are selected. t0 value of each counter is determined by fitting the peak in

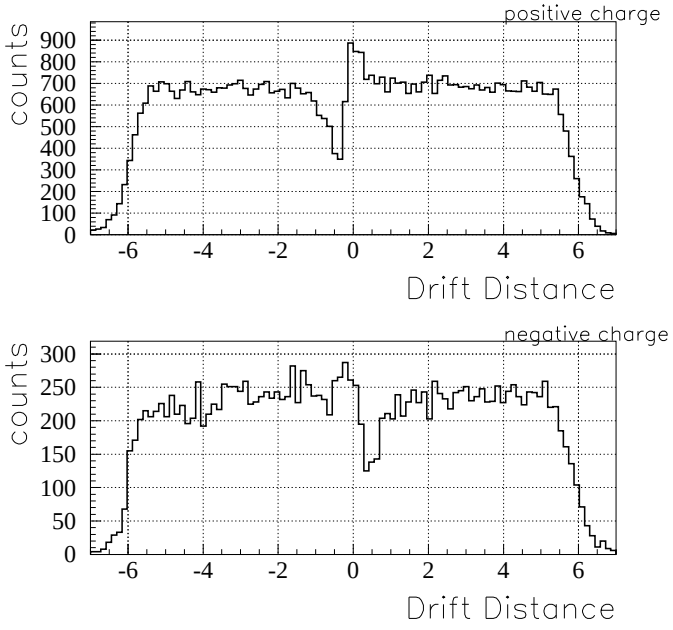

Figure 3.24: Drift distance. Upper plot is for positive charged particles and bottom one is for negative charged particles.

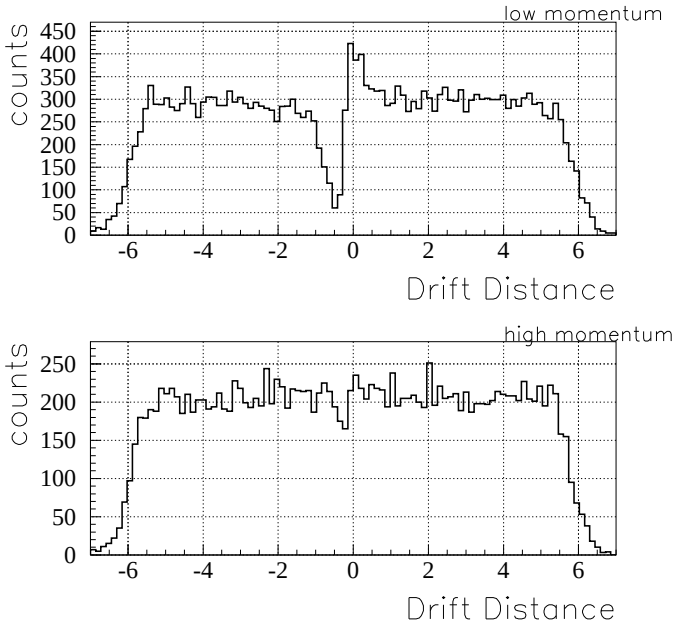

Figure 3.25: Drift distance of positive charged particles. Top plot is for low momentum particles ($p < 0.8$) and bottom one is for high momentum particles ($p > 1.2$).

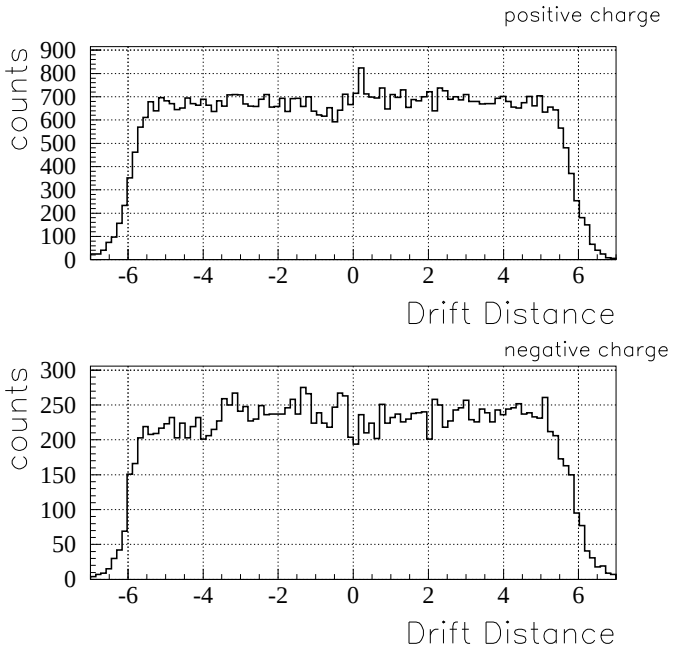

Figure 3.26: Drift distance after the modification of LEPSana. Top plot is for positive charged particles and bottom one is for negative charged particles.

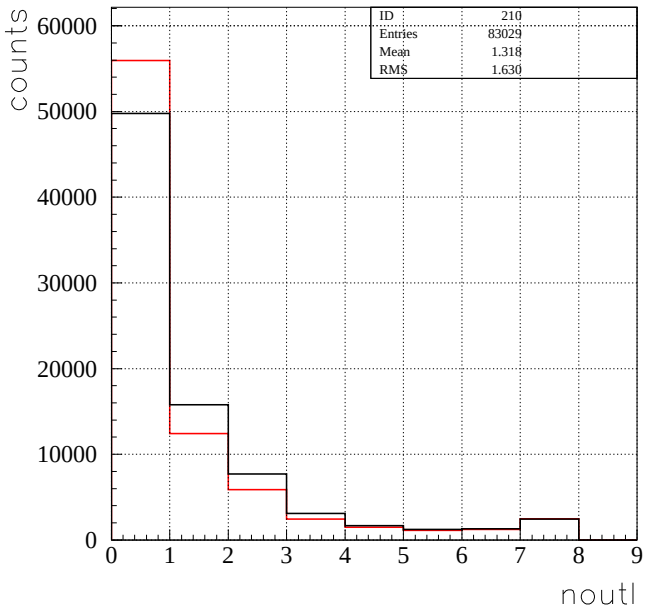

Figure 3.27: The number of outliers. Black histogram is for the old algorithm and red histogram is for modified one.

the TDC distribution which corresponds to associated hits with a Gaussian function. Figure 3.28 shows the TDC-t0 of SFF channel 1. Clear peak which corresponds to the hits associated with the triggered event is seen. Note that the timing information of TAG-PL registered in FASTBUS 1875A is used for further selection when several Tagger tracks remains. This will be described in section 3.5.1.

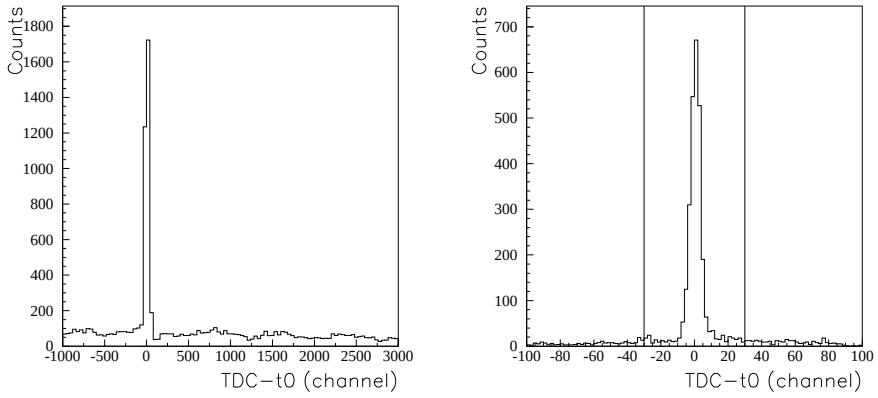

Figure 3.28: Left plot: TDC-t0 for SFF channel 1. Right plot is a zoom plot of the left one. Vertical lines show the cut point.

Clustering of TAG-SF

A cluster is made by combining neighboring fiber hits. The number of fiber hits in one cluster is called cluster size. A fiber hit which does not have neighbor hit is also identified as a cluster whose cluster size is one. Clustering is performed for both TAG-SFF and TAG-SFB individually. The position of the cluster (x_f for TAG-SFF and x_b for TAG-SFB) is calculated as the average of fiber channels in a cluster (for example, hit position of the cluster with channel 1 and 2 is 1.5). Then, the difference of the x_f and x_b is taken for all the combinations of clusters in TAG-SFF and TAG-SFB. If the difference is less than or equal to 2, the clusters are identified as one tagger track which will be converted to the photon energy. If no consistent combination is found, then the cluster which have consistent hit of TAG-PL is identified as a tagger track.

Selection of true Tagger track

Figure 3.29 (a) shows the number of Tagger tracks (ntag) distribution. When the ntag is equal to one, the track is used. When the ntag is equal to zero, the events are discarded. When the ntag is greater than one, further selection criteria using the information of the timing information of TAG-PL registered by TDC module 1875A is performed. The TDC 1875A has a good timing resolution (1 channel corresponds to 25 ps). Therefore, it is possible to select a tagger track which corresponds to the event more precisely. If the TDC of TAG-PL which corresponds to one track is within 80 channel of t0 (2 ns) and the TDCs of TAG-PL which

corresponds to the other track are not within 80 channel of t0, the former hit is selected. The t0 is determined by the fitting of TDC distribution by the Gaussian. The cut boundary of 2 ns corresponds to the timing interval of the electron bunches. If the TAG-PL which corresponds to the tracks are the same (tracks are close), such events are discarded. Furthermore, if several TAG-PL has the TDC within the cut boundary, or no TAG-PL has the TDC within the cut boundary, such events are discarded too. Figure 3.29 (b) shows the TDC of TAG-PL which corresponds to one Tagger hit vs the TDC of TAG-PL which corresponds to the other Tagger hit. Figure 3.29 (c) and (d) show the $MM\gamma(p, K^+K^-)X$ of LH2 data for each ntag conditions. The peak corresponds to the proton is clearly seen also for ntag ≥ 2 events, which means the selection criteria written above works well. About the half of the events with ntag ≥ 2 can be used by this selection criteria.

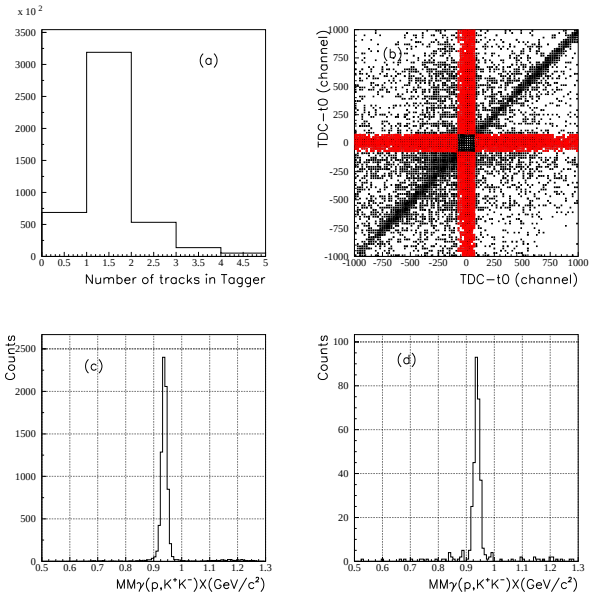

Figure 3.29: (a) Number of tracks in the Tagger. (b)Scatter plot of the TDC of TAG-PL which corresponds to one tagger track vs the TDC of TAG-PL which corresponds to the other track. Red points are events which true track is selected. (c) $MM\gamma(p, K^+K^-)X$ for LH2 data for ntag=1 events. (d) $MM\gamma(p, K^+K^-)X$ for LH2 data for ntag ≥ 2 events.

Selection of the clean Tagger track

Further criteria is applied to clean up events for the Θ^+ search. The consistency between hit position of TAG-SFF and that of TAG-SFB is checked. If the consistency is not good, the events are rejected.

Figure 3.30 shows the $MMp(\gamma, K^+)X$ and $MMp(\gamma, K^+K^-)X$ in LH2 data for events which are rejected or survived by the Tagger cut. The missing mass resolution is clearly worse for rejected events. The rejected events are about 15% of all of the data. The σ of $MMp(\gamma, K^+)\Lambda$ is improved from 12.2 to 12.0 MeV and the σ of $MMp(\gamma, K^+K^-)p$ is improved from 9.5 to 9.2 MeV by rejecting the bad consistency events.

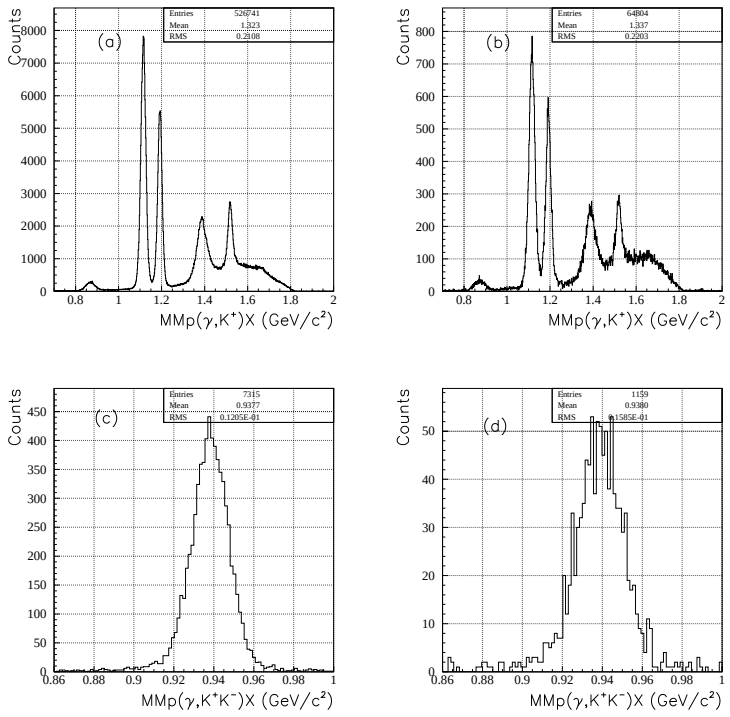

Figure 3.30: (a) $MMp(\gamma, K^+)X$ for the events which are survived by the Tagger cut. (b) $MMp(\gamma, K^+)X$ for the events which are discarded by the Tagger cut. (c) $MMp(\gamma, K^+K^-)X$ for the events which are survived by the Tagger cut. (c) $MMp(\gamma, K^+K^-)X$ for the events which are discarded by the Tagger cut.

3.5.2 Conversion function from a tagger hit position to a photon energy

It is necessary to convert a tagger hit to the photon energy. The reaction $\gamma p \rightarrow K^+\Lambda$ with the detection of the K^+ is used to obtain the conversion function (LH2 data is used). The reaction is selected because it has highest statistics among all the reaction modes in LH2 data and background level is low. The photon energy can be predicted from the K^+ momentum by assuming that missing mass of K^+ is equal to be the mass of Λ ($E_{\gamma(calc)}$) as

$$E_{\gamma(calc)} = \frac{M_\Lambda^2 - M_p^2 - M_K^2 + 2M_p E_{K^+}}{2(M_p - E_{K^+} + p_{K^+}^z)}, \tag{3.11}$$

where M_Λ, Mp is the mass of the Λ and the proton, E_{K^+}, $p_{K^+}^z$ is the energy and z-component of the momentum of the a K^+. The conversion function is determined individually for both TAG-SFF and TAG-SFB. Figure 3.31 shows the $E_{\gamma(calc)}$ as a function of fiber channels. The clusters with cluster size equal to one are used to determine the conversion functions.

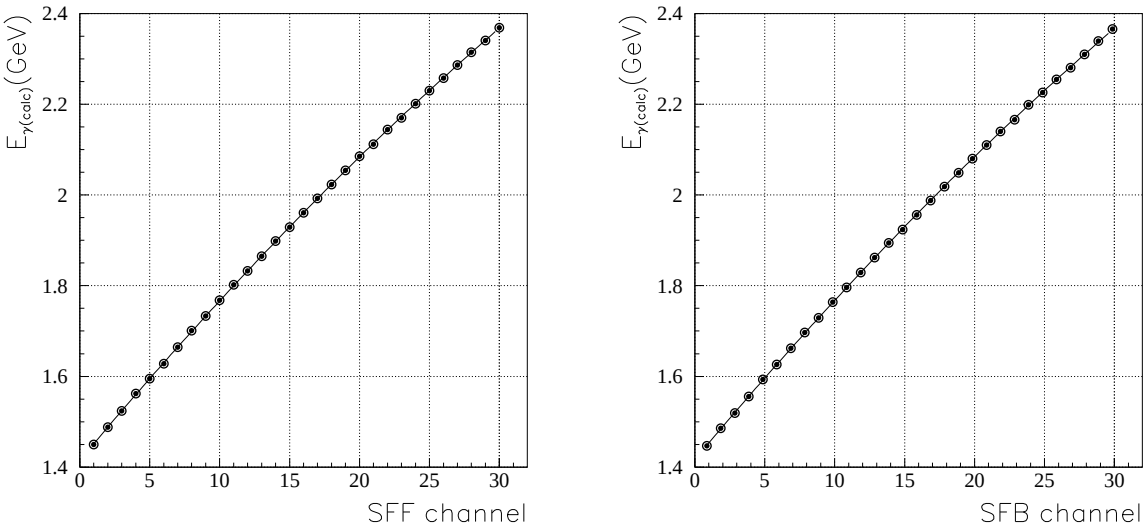

Figure 3.31: ($E_{\gamma(calc)}$) as a function of TAG-SF channel. Fitting function is second order polynomial

The actual photon energy (E_γ) is obtained by taking the average of that obtained by TAG-SFF ($E_{\gamma f}$) and TAG-SFB ($E_{\gamma b}$). However, the energy resolution for the cluster whose cluster size greater than 2 is not good. So, if cluster size of TAG-SFF is less or equal to 2 and that of TAG-SFB is greater than 2, the $E_{\gamma f}$ is identified as E_γ, and vice-verse. Figure 3.32 shows the cluster size of TAG-SFF dependence of $MMp(\gamma, K^+)X$. $E_{\gamma f}$ is used for E_γ. We can see that missing mass resolution become worse when cluster size is larger than 2.

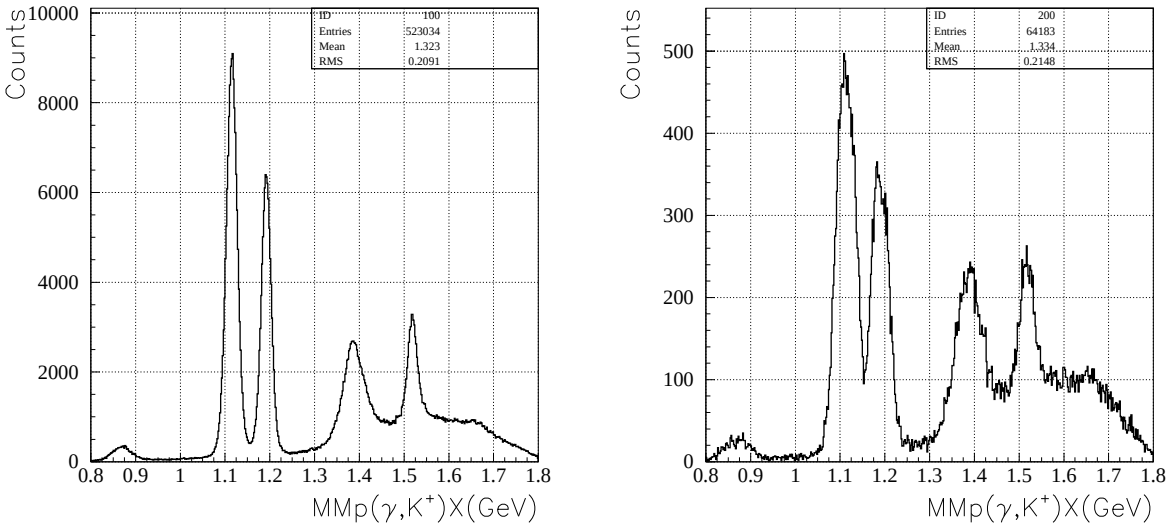

Figure 3.32: $MMp(\gamma, K^+)X$. $E_{\gamma f}$ is used for E_γ. Left plot is for cluster size less than or equal to 2 and right plot is for cluster size greater than 2.

3.5.3 Momentum scale factor

The method to obtain the conversion function written in previous section relays on K^+ momentum. To check the correctness of the measurement of momentum, the peak position of the missing mass for several reaction modes are checked. The modes used are as follows.

- $\gamma p \to \pi^+\pi^- p$ (detect π^+ and π^-) $\to mode1$
- $\gamma p \to K^+K^- p$ (detect K^+ and K^-) $\to mode2$
- $\gamma p \to K^+K^- p$ (detect K^- and p) $\to mode3$

The deviation of the peak position of the missing mass from the PDG value(δMM) is summarized in table 3.4. The δMM for three modes are not small enough. The phenomenological momentum scale factor is multiplied to the momentum in order to adjust the peak positions of missing mass to be close to the PDG value. The momentum scale factor is determined by following procedure.

- Assume a momentum scale factor.
- Determine the conversion function from a tagger hit position to a photon energy using $\gamma p \to K^+\Lambda$ reaction.
- Check the peak position of three modes.

Figure 3.33 shows the result of procedure written above. From this figure, the momentum scale factor is determined to be 1.006.

	Mode1	Mode2	Mode3
δMM (MeV/c^2)	1.5±0.1	-1.6±0.3	-4.5±0.4

Table 3.4: Summary of deviation of the missing mass from PDG value (δMM)

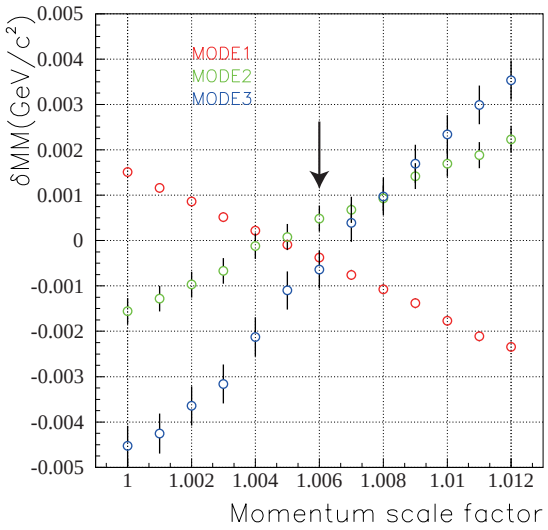

Figure 3.33: The peak position of three modes as a function of momentum scale factor.

3.5.4 Hot fiber

There are several fibers in TAG-SFB which are very noisy (hot fiber). Figure 3.34 shows the ratio of number of events with cluster size=2 to that of cluster size=1 as a function of the fiber channel. The ratio is very large for channel 25, 26, and 27 of TAG-SFB. The reason why ratios are very high for these channels is the threshold of discriminator are set to be too low. The photon energy correspond to these channels is 2.2-2.3 GeV. Figure 3.35 shows the mean of δE_γ defined by

$$\delta E_\gamma = E_\gamma - E_{\gamma(calc)} \tag{3.12}$$

for $\gamma p \to K^+\Lambda$ reaction and $\gamma p \to \pi^+\pi^- p$ reaction. The value δE_γ shows the deviation of the peak position of the missing mass in a photon energy. The value is convenient when we calibrate photon energy. $E_{\gamma(calc)}$ for $\gamma p \to \pi^+\pi^- p$ reaction is written as

$$E_{\gamma(calc)} = \frac{-M_{\pi\pi}^2 + 2M_p(E_{\pi^+} + E_{\pi^-})}{2(M_p - E_{\pi^+} - E_{\pi^-} + p_{\pi^+}^z + p_{\pi^-}^z)}, \tag{3.13}$$

where $M_{\pi\pi}$ is an invariant mass of π^+ and π^- and $E_{pi^{+-}}$ is energy of π^{+-} and $p_{\pi^{+-}}^z$ is the z-component of the momentum of π^{+-}. The mean of δE_γ is deviated from zero for both mode with the same magnitude if $E_{\gamma b}$ is used as E_γ and cluster size of TAG-SFB is 2 for hot fiber region. The $E_{\gamma b}$ is corrected if channel is 25 or 26 or 27 and cluster size is 2. The photon energy resolution for hot fiber region is not good. This will be discussed in later section.

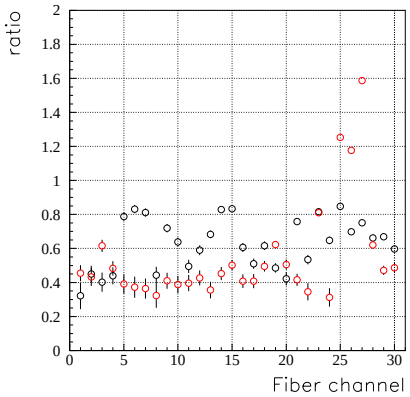

Figure 3.34: The ratio of number of events with cluster size=2 to that of cluster size=1. Black plot is for TAG-SFF and red one is for TAG-SFB.

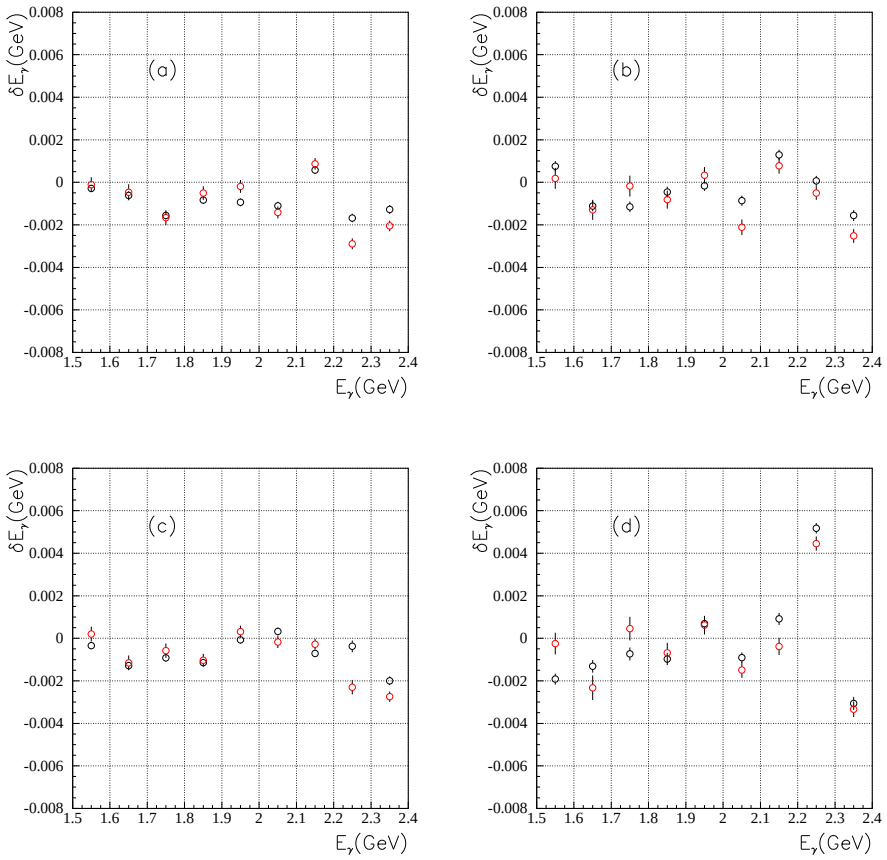

Figure 3.35: Mean of δE_γ as a function of photon energy. (a):$E_{\gamma f}$ is used as E_γ. Cluster size of TAG-SFF is 1. (b):$E_{\gamma f}$ is used as E_γ. Cluster size of TAG-SFF is 2. (c):$E_{\gamma b}$ is used as E_γ. Cluster size of TAG-SFB is 1. (d):$E_{\gamma b}$ is used as E_γ. Cluster size of TAG-SFB is 2. Black plot is for $\gamma p \to K^+\Lambda$ reaction and red plot is for $\gamma p \to \pi^+\pi^- p$ reaction.

3.5.5 Peak position of the missing mass as a function of the photon energy

The peak position of the missing mass as a function of photon energy for various modes in LH2 data are checked.

Figure 3.36 shows the $MMp(\gamma, K^+)X$ and the peak position of Λ, Σ, respectively. Figure 3.37 shows the $MMp(\gamma, \pi^+\pi^-)X$ and the peak position of the proton. Figure 3.38 shows the $MMp(\gamma, K^+K^-)X$ and the peak position of the proton. Figure 3.39 shows the $MMp(\gamma, K^-p)X$ and the peak position of the K^+.

The peak positions are consistent with PDG values for all the photon energy and for all the modes. The fact indicates that the calibration of photon energy and the momentum of charged particles are good.

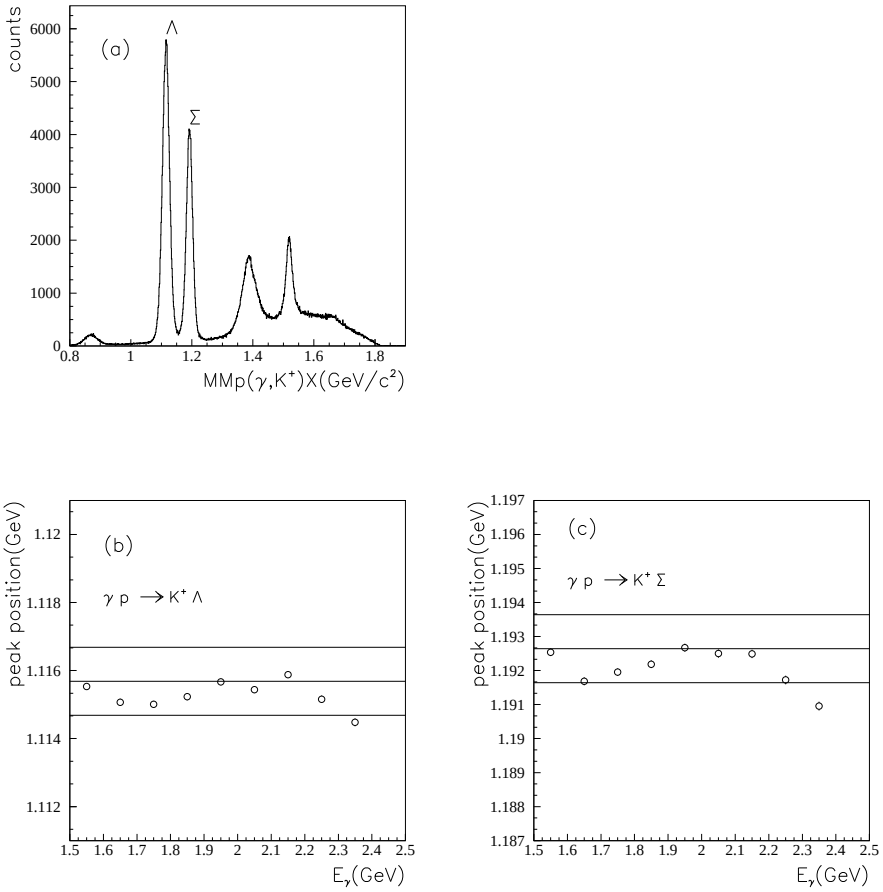

Figure 3.36: (a)$MMp(\gamma, K^+)X$ for LH2 data. (b)Peak position of MMp$(\gamma, K^+)\Lambda$ as a function of the Eγ. Horizontal lines show the PDG value of the mass of the Σ $\pm 1 MeV$. (c)Peak position of MMp$(\gamma, K^+)\Sigma$ as a function of the Eγ. Horizontal lines show the PDG value of the mass of the Σ $\pm 1 MeV$.

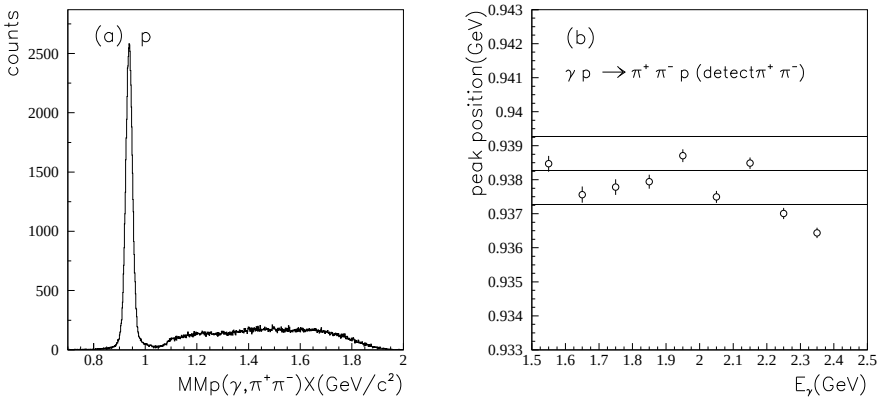

Figure 3.37: (a)$MMp(\gamma,\pi^+\pi^-)X$ for LH2 data. (b)Peak position of MMp$(\gamma,\pi^+\pi^-)p$ as a function of the Eγ. Horizontal lines show the PDG value of the mass of the proton $\pm 1MeV$.

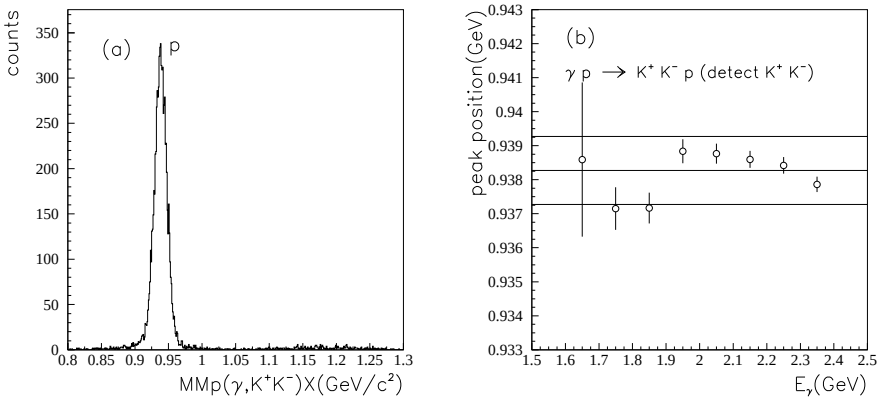

Figure 3.38: (a)$MMp(\gamma,\pi^+\pi^-)X$ for LH2 data. (b)Peak position of MMp$(\gamma,\pi^+\pi^-)p$ as a function of the Eγ. Horizontal lines show the PDG value of the mass of the proton $\pm 1MeV$.

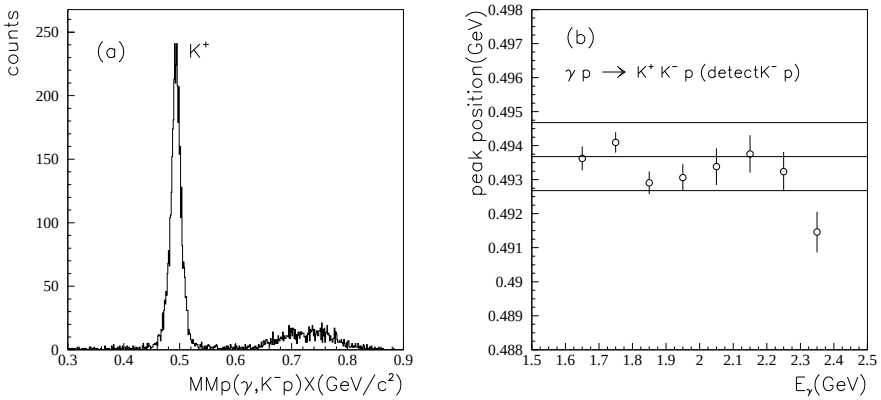

Figure 3.39: (a)$MMp(\gamma,K^-p)X$ for LH2 data. (b)Peak position of MM p$(\gamma,K^-p)K^+$ as a function of the Eγ. Horizontal lines show the PDG value of the mass of the K^+ $\pm 1MeV$.

3.5.6 Photon energy resolution

The photon energy resolution is an important parameter in the LEPS experiment. In this section, the determination of the photon energy resolution is described.

The width of the δE_γ ($\sigma_{\delta E_\gamma}$) is written as

$$\sigma_{\delta E_\gamma} = \sqrt{\sigma^2_{E_\gamma} + \sigma^2_{E_{\gamma(calc)}}}, \tag{3.14}$$

where σ_{E_γ} is the photon energy resolution which we want to obtain and $\sigma_{E_{\gamma(calc)}}$ is the width come from the momentum resolution of the charged tracks. $\sigma_{E_{\gamma(calc)}}$ can be obtained by using MC because the true photon energy is known for MC data. $\sigma_{\delta E_\gamma}$ is equal to $\sigma_{E_{\gamma(calc)}}$ when we use true photon energy for $E_{\gamma(mes)}$ when calculating δE_γ. Then, the σ_{E_γ} can be obtained as

$$\sigma_{E_\gamma} = \sqrt{\sigma^2_{\delta E_\gamma} - \sigma^2_{E_{\gamma(calc)}}}. \tag{3.15}$$

Figure 3.40(a) shows the $\sigma_{\delta E_\gamma}$ as a function of E_γ for $\gamma p \to K^+\Lambda$ reaction for real data and MC data. Black points are for real data, red points are for MC data, and blue points are for MC data with smearing DC resolution with a factor of 15%, respectively. Figure 3.40(b) shows the δ_{E_γ} as a function of E_γ when red points of Fig.3.40(a) are used as $\sigma_{E_{\gamma(calc)}}$. The σ_{E_γ} becomes larger as photon energy increase. The fact indicates that the momentum resolution of MC is underestimated because the main source of the photon energy resolution comes from the emittance and the energy resolution of the electrons in the storage ring, and hence it does not depends on the photon energy. In order to remove the photon energy dependence, the position resolution of DCs for MC is phenomenologically smeared by a factor of 15%. Figure 3.40(c) shows the δ_{E_γ} as a function of E_γ when blue points of Fig.3.40(a)(DCs are 15% smeared) are used as $\sigma_{E_{\gamma(calc)}}$. The photon energy dependence of the photon energy resolution becomes much smaller. The photon energy resolution is obtained to be 12.6 MeV. Note that the energy resolution for hot fibers region is separately obtained and the result is 14.3 MeV.

To check the validity of the photon energy resolution obtained by the method written above, the photon energy resolution is also estimated by using $\gamma p \to \phi p \to K^+K^-p$ reaction with the detection of K^+ and K^- (ϕ event is selected by the invariant mass of K^+ and K^-). For $\gamma p \to K^+\Lambda$ reaction, the contribution of the momentum resolution of the K^+ to the $\sigma_{\delta E_\gamma}$ is large because the momentum of the K^+ is high ($2.0\,GeV/c$ at the maximum), and hence the momentum resolution is not good. On the other hand, the contribution of the momentum resolution is smaller for $\gamma p \to \phi p$ reaction because momentum of K^+ and K^- is relatively lower than that of $\gamma p \to K^+\Lambda$ reaction ($1.2\,GeV/c$ at the maximum). Therefore, to check the consistency of these two modes is a good test for the validity of the analysis. Figure 3.41 shows the δE_γ for $\gamma p \to \phi p$ reaction. The photon energy resolution for both detection modes are summarized in table 3.5. The consistency is good for the photon energy other than hot fiber region. However, The consistency is not good for hot fiber region. The photon energy resolution for hot fiber region is almost the same as that for the photon energy other than hot fiber region for $\gamma p \to \phi p$ reaction. To check this point further, $\sigma_{\delta_{E_\gamma}}$ is checked for $\gamma p \to \pi^+\pi^-$ reaction which have much higher statistics than $\gamma p \to \phi p$ reaction. Figure 3.44 shows the $\sigma_{\delta E_\gamma}$ for $\gamma p \to \pi^+\pi^-$ reaction as a function of the photon energy. The $\sigma_{\delta E_\gamma}$ is clearly bad for hot fiber region. Therefore, the inconsistency between two modes seen in hot fiber region is thought to be a statistical fluctuation.

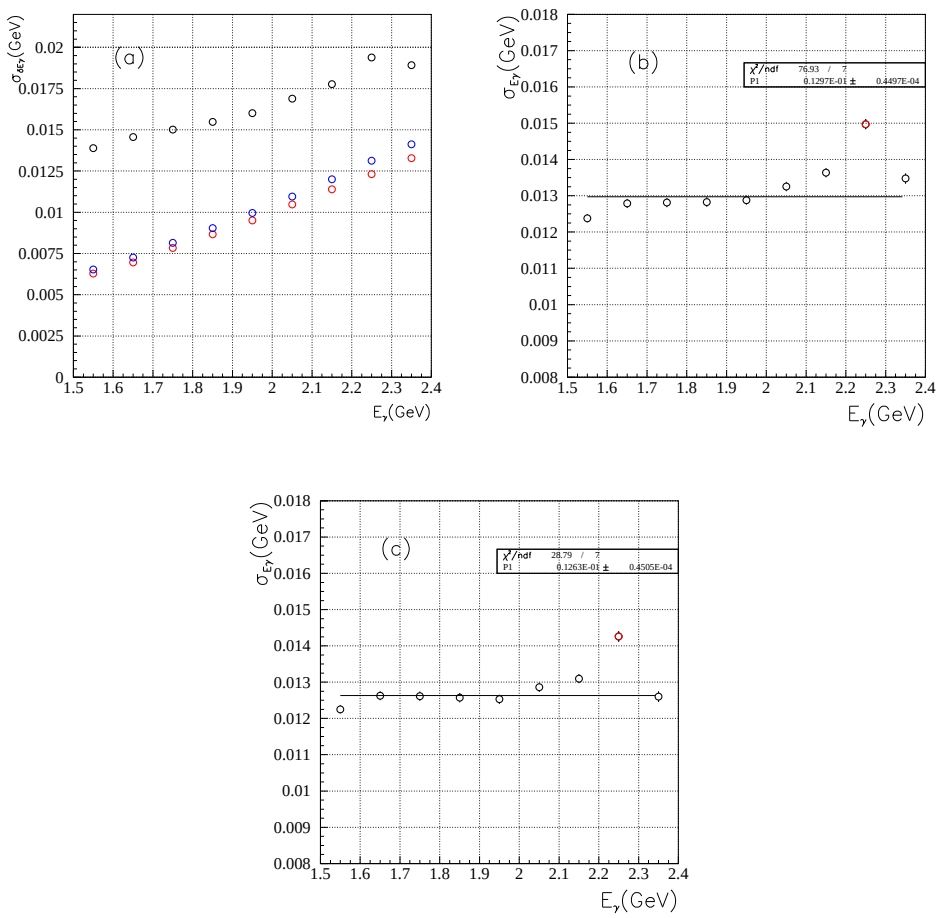

Figure 3.40: (a) $\sigma_{\delta E_\gamma}$ for $\gamma p \to K^+\Lambda$ reaction as a function of the photon energy. Black, red, blue points are for real data, MC data, MC data with a smearing of DCs by a factor of 15%, respectively. (b) σ_{E_γ} as a function of photon energy. Red points in (a) are used as $\sigma_{E_{\gamma(calc)}}$. Red point indicates the hot fiber region. Fitting line is constant. Red point is not used in the fitting. (c) The same as (b) but blue points in (a) are used as $\sigma_{E_{\gamma(calc)}}$.

	σ_{E_γ} from $K^+\Lambda$ mode (MeV)	σ_{E_γ} from ϕ mode (MeV)
not hot fiber	12.6±0.05	12.5±0.2
hot fiber	14.3±0.1	12.7±0.4

Table 3.5: Summary of the photon energy resolution obtained by two reaction modes.

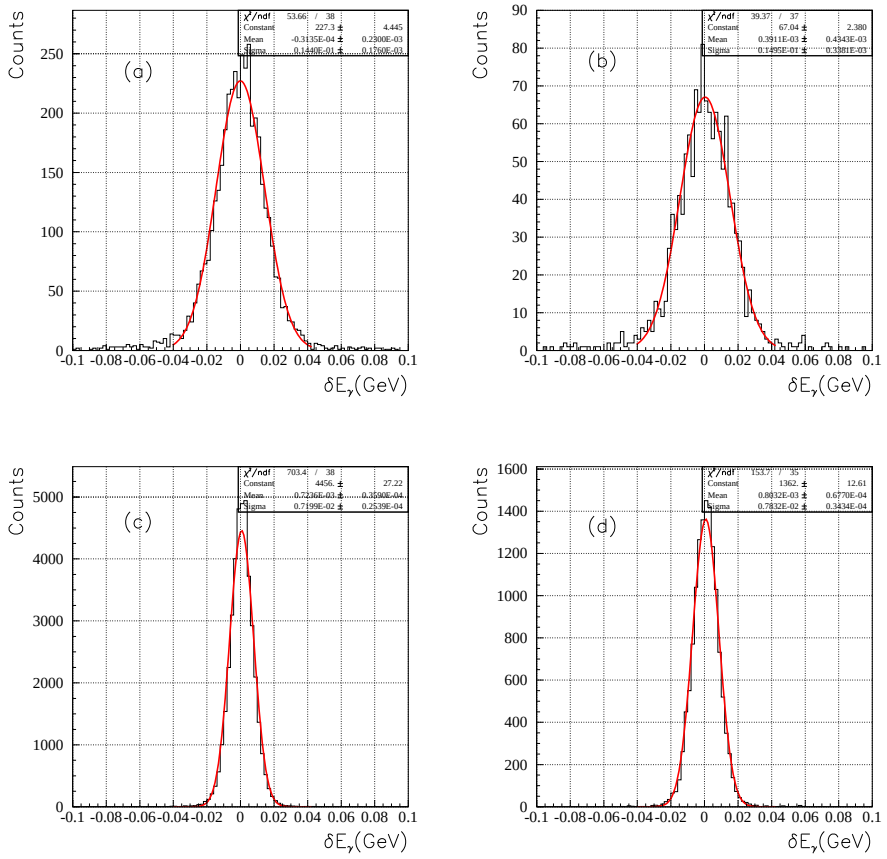

Figure 3.41: δE_γ for $\gamma p \to \phi p$ reaction. (a) Real data. The photon energy is other than hot fiber region. (b) Real data. The photon energy is hot fiber region. (c) MC data. The photon energy is other than hot fiber region. (d) MC data. The photon energy is hot fiber region.

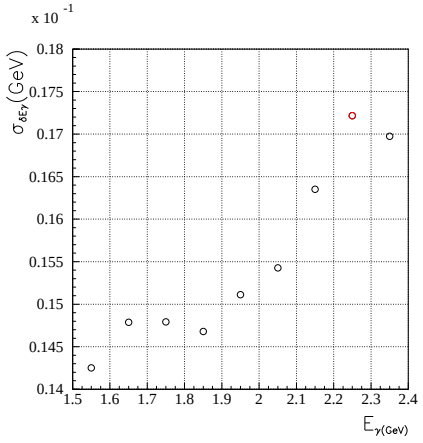

Figure 3.42: $\sigma_{\delta E_\gamma}$ for $\gamma p \to \pi^+\pi^-$ reaction as a function of the photon energy. Red point indicates the hot fiber region.

3.5.7 Correction for the photon energy as a function of x-vertex position

The x-vertex position reflects the angle of an electron in the storage ring which collides with a laser photon. Although the hit position in the tagger is the same, the energy of the photon beam is different if the angle of the electron is different. Figure 3.43 shows the mean of δE_γ for mode1 as a function of x-vertex. Clear correlation is seen. The correction for the photon energy is applied with linear function (vertex correction). Figure 3.44 shows the $\delta_{E\gamma}$ with and without the vertex correction. The σ of $\delta_{E\gamma}$ is improved from 16.5MeV to 16.0MeV. Therefore, the smearing from without vertex correction is $\sqrt{16.5^2 - 16.0^2} = 4.0MeV$. Note that this correction can not be applied for single track detection modes like $\gamma p \to K^+\Lambda$ reaction because the reaction vertex point is obtained from the closest distance of a track and beam axis and the resolution is not good. For the more than two tracks detection modes, the reaction vertex point is obtained by the closest distance of two tracks and position resolution of the vertex point is good. The photon energy resolution for two track detection mode is $\sqrt{12.6^2 - 4.0^2} = 11.9MeV$ for the photon energy other than hot fiber region and $\sqrt{14.3^2 - 4.0^2} = 13.7MeV$ for the hot fiber region.

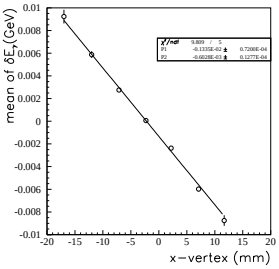

Figure 3.43: Mean of the δE_γ for $\gamma p \to \pi^+\pi^- p$ reaction as a function of x-vertex. The fitting line is the linear function.

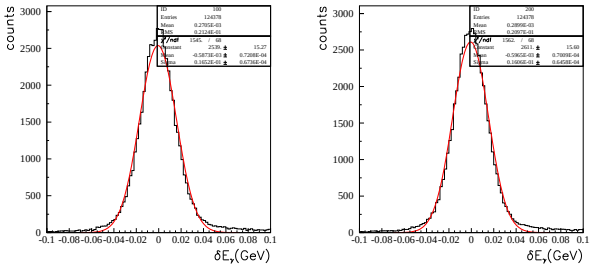

Figure 3.44: δE_γ for $\gamma p \to \pi^+\pi^- p$ reaction. Left plot is without the vertex correction and right plot is with the vertex correction.

3.6 Comparison between two data sets

In this section, the comparison of the data quality between the data taken in 2002-2003 (previous data) and 2006-2007 (new data) in terms of detector performance is described.

3.6.1 Detector resolution

TOF

Figure 3.45 shows the mean and the σ of reconstructed mass square obtained by the TOF and the momentum measurement for two data sets. Both mean and σ are consistent for two data sets.

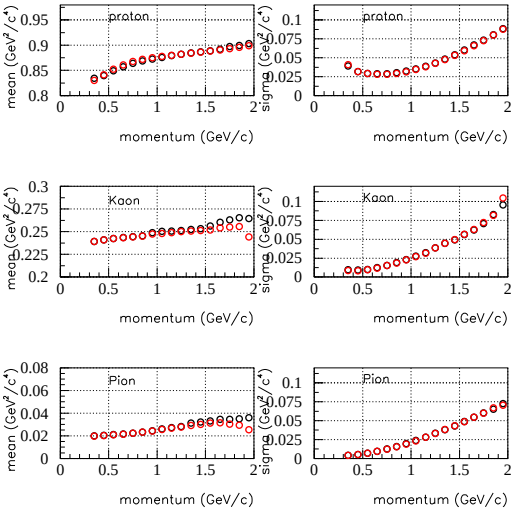

Figure 3.45: Mean and the σ of mass square of Proton, Kaon, and Pion. Black points are for new data and red points are for previous data.

DCs

The position resolution of DCs for two data sets are summarized in table 3.6. The position resolution is much better for new data. There are two reasons for the improvement of the resolution. One is the new timing correction and the modification of the determination of xt-curve. The other is the setting of the maximum number of accepted hits for DCs (depth) for TDC for previous data. The issue is written in [61] in detail.

Photon energy resolution

The photon energy resolution for new data and previous data is summarized in table 3.7. The photon energy resolution for previous data depends on the run# because the electron beam

Plane	resolution of new data (mm)	resolution of previous data (mm)
DC1X	0.143	0.260
DC1U	0.141	0.206
DC1V	0.178	0.266
DC2X	0.146	0.243
DC2U	0.147	0.246
DC2V	0.331	0.403
DC3X	0.153	0.264
DC3U	0.146	0.246
DC3V	0.258	0.390

Table 3.6: Summary of position resolution of DCs.

condition of SPring-8 changed at the middle of data taking. The determination of the photon energy resolution for previous data is written in [67].

run	without vertex correction (MeV)	with vertex correction (MeV)
1/3 of previous data	11.7	10.3
2/3 of previous data	13.3	13.0
new data	12.6 (14.3)	11.9 (13.7)

Table 3.7: Summary of the photon energy resolution. The values in the parenthesis are for hot fiber region.

3.6.2 Missing mass resolution

Figure 3.46 shows the missing mass spectrum for various reaction modes for two sets. The two histograms are normalized by the entries. Therefore, the difference of the height of the spectrum directly represents the difference of the missing mass resolution. The missing mass resolution of the new data is better than that of previous data for all the reaction modes. The improvement of the missing mass resolution mainly comes from the improvement of the position resolution of DCs. The improvement is large for $\gamma p \to K^+\Lambda$ and $\gamma p \to K^+\Sigma$ reactions. This is because the K^+ momentum is high for these modes as already mentioned. The missing mass resolution for two data sets as a function of the photon energy is also shown in Fig. 3.47.

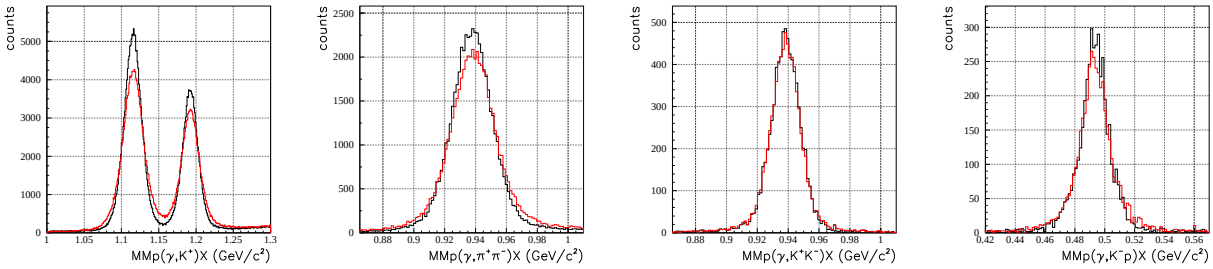

Figure 3.46: Missing mass spectrum. Black histograms are for new data and red ones are for previous data. Two histograms are normalized by the entries.

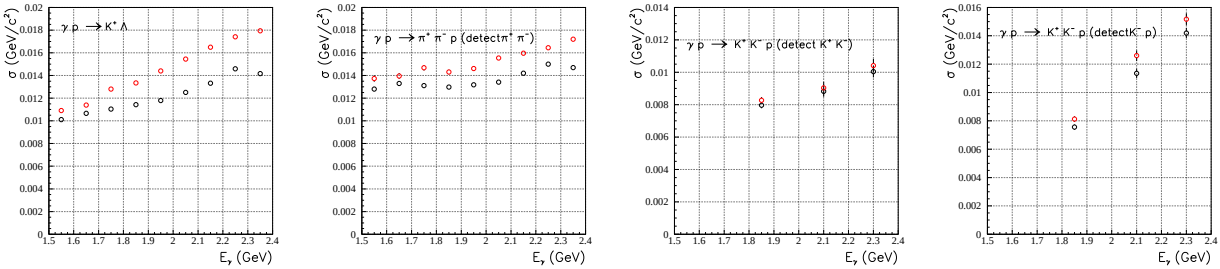

Figure 3.47: Missing mass resolution as a function of the photon energy. Black points are for new data and red points are for previous data

Chapter 4

Analysis for the Θ^+ search

In this chapter, the analysis for the Θ^+ search is described.

4.1 Blind analysis

As described in chapter 1, the purpose of this work is confirmation of the previous result of the Θ^+ search by using data taken in 2002-2003 (previous data) [48]. The previous result shows an evidence of the Θ^+ in $\gamma d \to K^+K^-pn$ reaction with a statistical significance of 5.1 σ. In the analysis of the new data, the blind analysis is applied to remove an artificial bias. The blind analysis means the cut conditions are fixed from the previous data and calibration parameters are tuned without seeing the signal region.

This chapter is organized as follows. First, the studies done in previous results like cut conditions and background estimation are described. Then, the consistency checks of the new data and the previous data are discussed. There are two purpose for the comparison of two data sets. One is to check if there are any problems for the new data (or possibly for the previous data). The other is to check if it is possible to combine two data sets after we open the box by comparing the mass resolutions and acceptances of both data sets are essentially the same.

Several comparison of two data sets for LD2 data other than K^+K^- detection mode can be found in appendix B.

4.2 Selection of the K^+ and K^- pairs from the LD2 target

The Θ^+ search is performed with a event sample in which K^+ and K^- tracks from a LD2 target are detected. In this section, the cut conditions to select the events noted above are discussed.

4.2.1 Number of tracks

The number of charged tracks is required to be greater than 1.

4.2.2 Particle identification

Particle identification is performed using the mass reconstructed by TOF and momentum measurements. The mass resolution is momentum dependent, and parametrized as

$$\sigma^2_{m^2} = 4m^4(1 + (m/p)^2)a_1^2 + 4m^4p^2a_2^2 + 4p^2(p^2 + m^2)((c/L)a_3), \tag{4.1}$$

where a_1, a_2, a_3 are parameters, m is the nominal value of the mass, c is the speed of light, p is the momentum, and L is the path length between start counter and the TOF wall. First term represents the contribution of multiple scattering, second term represents the contribution of the momentum resolution of spectrometer, and last term represents the contribution of TOF resolution, respectively. a_1 and a_2 is obtained from the MC. They are found to be a_1=0.00458 and a_2=0.00323. a_3 is obtained from the TOF resolution and found to be 0.175 [57]. The tracks with reconstructed mass within 3.5σ of the mass resolution are identified as Kaon. The boundary between Pions (Protons) and Kaons is set to be 0.1 GeV^2 (0.55GeV^2). Figure 4.1 shows the reconstructed mass spectrum and the boundaries for the selection of the Kaon.

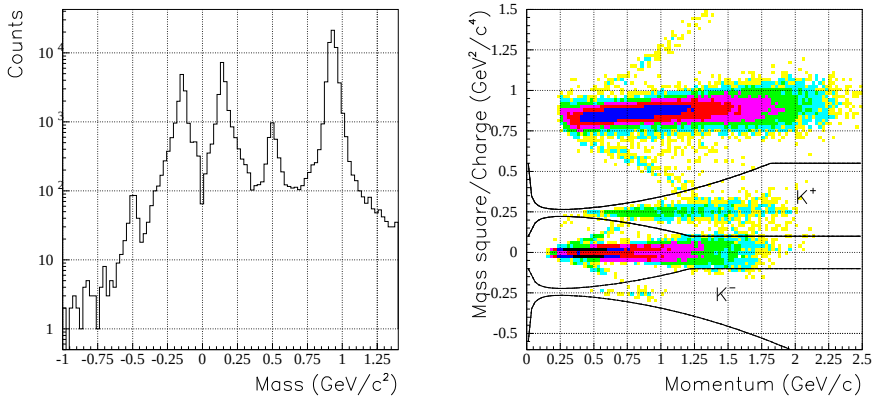

Figure 4.1: Left plot is reconstructed mass spectrum. Right plot is scatter plot of mass-squared/charge vs momentum. Solid lines show the boundaries for the selection of the Kaon.

4.2.3 Rejection of the decay-in-flight events

The event samples are cleaned up by removing the tracks with large track-reconstruction errors due to the decay-in-flight. The decay-in-flight cut are defined as follows.

Consistency of the x-positions at TOF walls

A TOF counters which is predicted to be fired by a track or the adujsent of that counter is actually fired.

Consistency of the y-positions at TOF walls

The difference between y positions measured by the TOF counter and that predicted by the track is required to be less than 80 mm.

χ^2 probability cut

The χ^2 probability of the tracking is required to be larger than 0.02.

Number of outliers cut

If a hit position of DCs is deviated from the position predicted by the track largely, the hit is judged as background hit (outlier) and removed from the tracking. The number of outliers is required to be less than 7.

4.2.4 Vertex cut

Figure 4.2 shows the z-vertex and x-vertex spectrum obtained by the closest distance of K^+ and K^- tracks. The events from the LD2 target are clearly separated from that from the STC. A cut on -1100≤z-vertex≤-900 is applied to select the events from the LD2 target. The cut on -25≤-vertex≤25 is also applied to clean up the event sample.

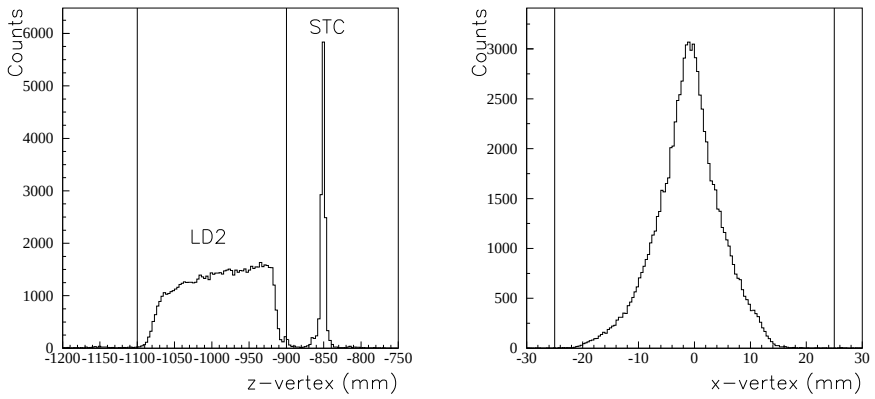

Figure 4.2: Left plot is z-vertex spectrum. Right plot is x-vertex spectrum. Vertical lines show the cut points

4.3 Tagger cut

The events which true tagger track is successfully selected are used for further analysis. (refer section 3.5.1).

4.4 Minimum momentum spectator approximation

4.4.1 Fermi motion correction

The process of interest is quasi-free production of the Θ^+ and $\Lambda(1520)$ and their sequential decay, i.e., $\gamma p \to K^+\Lambda(1520) \to K^+K^-p$ and $\gamma n \to K^-\Theta^+ \to K^-K^+n$.

The nucleons inside the deuterium have the Fermi momentum. Figure 4.3 shows the Fermi momentum obtained by using the Paris potential [69]. The average of the Fermi momentum is approximately 90MeV/c and the RMS is approximately 70MeV. The value is much larger than the momentum and photon energy resolution of the LEPS detectors. Therefore, simple missing mass of a Kaon assuming that a struck nucleon is at rest do not give a good mass resolution. MC study shows that the mass resolution of Θ^+ with this assumption is approximately 30MeV.

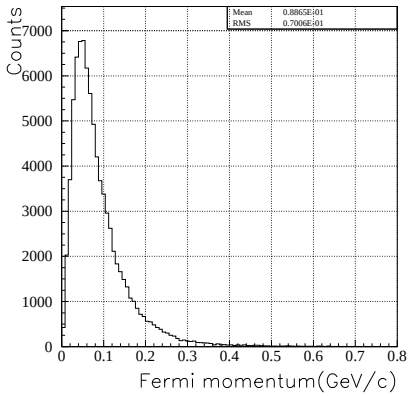

Figure 4.3: Fermi momentum of nucleons inside the deuterium obtained by using the Paris potential.

The minimum momentum spectator approximation(MMSA) has been developed in order to improve the mass resolution. The nucleon which is not associated with quasi-free process is called a spectator. In the MMSA, the spectator is assumed to have a possible minimum momentum for given momentum and energy of the pn pair. The momentum and energy of pn pair (E_{pn} and $\vec{p}_{pn}$) is given by missing momentum/energy of K^+ and K^- for $\gamma d \to K^+K^-pn$ reaction. The assumption is a good approximation because the Fermi momentum (momentum of the spectator) is much smaller than the momentum of photon beam and K^+ and K^- detected by spectrometer. The minimum momentum is given when the momentum vector of the spectator is anti-parallel to that of the missing momentum. Therefore, The momentum of the spectator ($\vec{p}_{min}$) is given by

$$M_{pn} = \sqrt{E_{pn}^2 - |\vec{p}_{pn}|^2} \tag{4.2}$$

$$|\vec{p}_{cm}| = \frac{\sqrt{(M_{pn}+M_p+M_n)(M_{pn}-M_p+M_n)(M_{pn}+M_p-M_n)(M_{pn}-M_p-M_n)}}{2M_{pn}} \tag{4.3}$$

$$\vec{p}_{cm} = |\vec{p_{cm}}| \cdot \vec{p}_{pn}/|\vec{p}_{pn}| \tag{4.4}$$

$$E_{cm} = \sqrt{M_{p(n)}^2 + |\vec{p}_{cm}^2|} \tag{4.5}$$

$$\beta = |\vec{p}_{pn}| E_{pn} \tag{4.6}$$

$$\gamma = E_{pn}/M_{pn} \tag{4.7}$$

$$p_{min} = \gamma(\beta E_{cm} - |\vec{p}_{cm}|), \tag{4.8}$$

$$\vec{p}_{min} = p_{min} \cdot \vec{p}_{pn}/|\vec{p}_{pn}| \tag{4.9}$$

where $\vec{p}_{cm}$, E_{cm} is the momentum and energy of nucleons in pn rest frame, γ is Lorentz factor, β is a velocity of pn system in laboratory frame in a unit of speed of light, respectively. Consequently, the momentum of struck nucleon in the final state ($\vec{p}_{res}$) is

$$p_{res} = \gamma(\beta E_{cm} + \vec{p}_{cm}). \tag{4.10}$$

$$\vec{p}_{res} = p_{res} \cdot \vec{p}_{pn}/|\vec{p}_{pn}| \tag{4.11}$$

Figure 4.4 shows the MC study of the validity of MMSA. The clear correlation is seen for true neutron momentum and that obtained by MMSA. The neutron momentum resolution by MMSA is 28MeV. This is much smaller than the RMS of the Fermi momentum (80MeV/c).

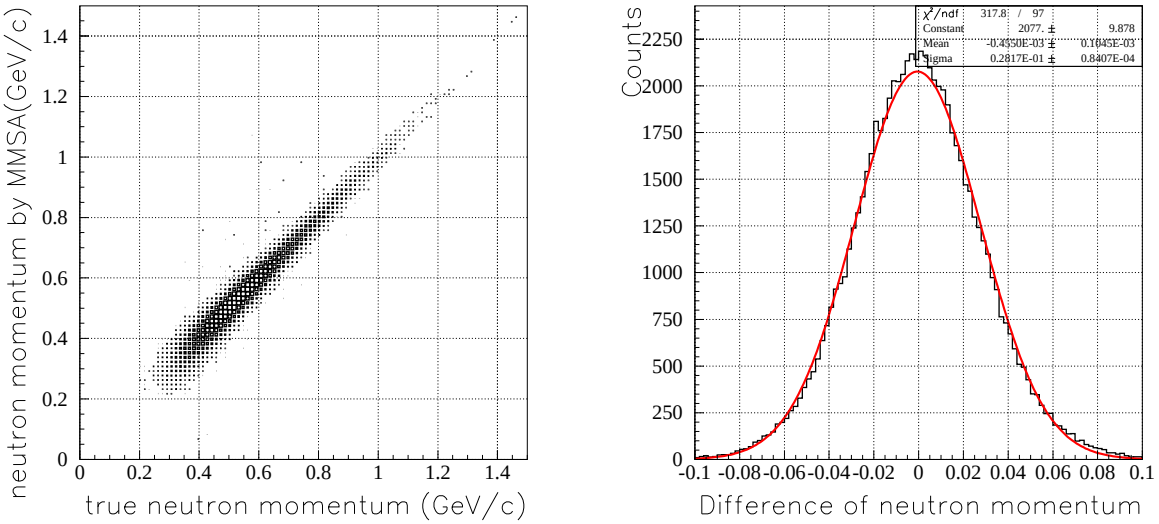

Figure 4.4: Left plot: The scatter plot of the true neutron momentum VS the neutron momentum obtained by MMSA in $\gamma n \to K^- \Theta^+ \to K^- K^+ n$ reaction using MC. Right plot: The difference of the true neutron momentum and the neutron momentum obtained by MMSA.

The nK^+ invariant mass can be obtained by using $\vec{p}_{res}$ as a momentum of the neutron. Figure 4.5 shows MC study of the simple missing of K^- and invariant mass of the nK^+ ($M(nK^+)$ by using MMSA in $\gamma n \to K^- \Theta^+ \to K^- K^+ n$ reaction. The invariant mass resolution by using MMSA is about $11 MeV/c^2$.

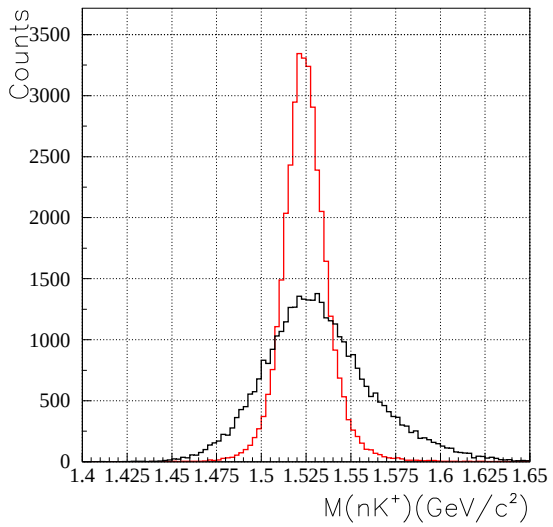

Figure 4.5: The MC study of the mass resolution of Θ^+ in $\gamma n \to K^-\Theta^+ \to K^-K^+n$ reaction. Black plot is simple missing mass of the K^-. Red plot is invariant mass of the nK^+ by using MMSA.

4.4.2 Rejection of the events other than quasi-free process.

The MMSA is useful not only for obtaining the good mass resolution but also for the rejection of the background events other than quasi-free process, $\gamma d \to K^+K^-pn$. Following reactions are considered as the background events other than quasi-free process.

- The coherent process which a deuteron exist in the final state, i.e, $\gamma d \to K^+K^-d$.
- The quasi-free production of $K^+K^-\pi$, i.e, $\gamma p(n) \to p(n)K^+K^-\pi$.

Figure 4.6 (a) shows the p_{min} distribution for the previous data. The negative value of the p_{min} means that the momentum vector is anti-parallel to that of pn system. The process (1) is characterized by large positive value of the p_{min} because the proton and the neutron effectively have the same momentum and hence possible minimum momentum becomes large. The process (2) is characterized by large negative value of the p_{min}. Figure 4.6 (b) shows the missing mass of the K^+K^- with assuming that the target is deuteron at rest. By requiring $p_{min} \geq 0.1GeV/c$, the peak corresponds to the coherent process can be selected. Figure 4.6 (c) shows the missing mass of the K^+K^- with assuming that the target is proton at rest. By requiring $p_{min} \leq -0.1GeV/c$, the tail component corresponds to the event associated with Pion is selected. The cut condition of $|p_{min}| \leq 0.1GeV/c$ is applied to reject background events.

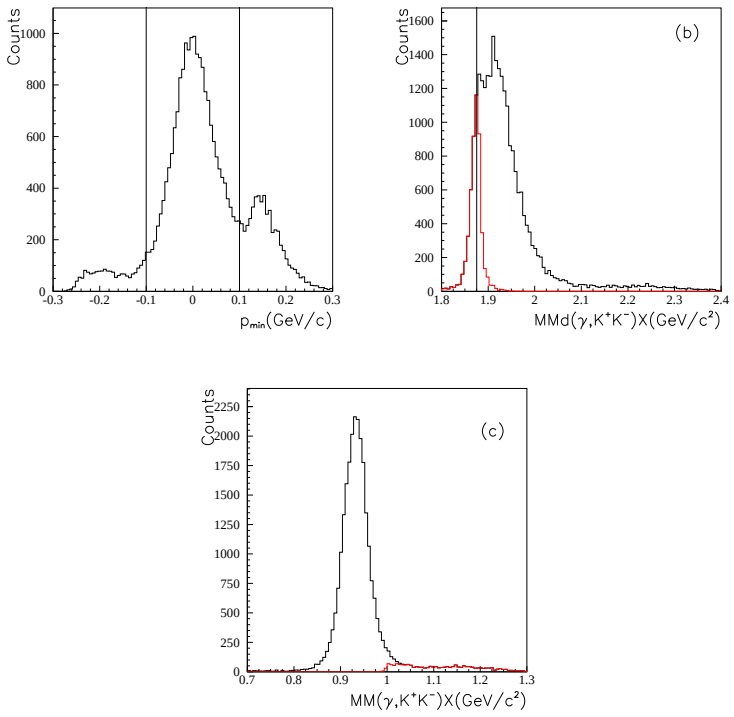

Figure 4.6: (a) The p_{min} distribution for the previous data. Vertical lines shows the cut points. (b) $MMd(\gamma, K^+K^-)X$. Black plot is without p_{min} cut, red plot is for $p_{min} \geq 0.1$, respectively. Vertical line shows the mass of the deuteron. (c) $MMp(\gamma, K^+K^-)X$. Black plot is without p_{min} cut, red plot is for $p_{min} \leq -0.1$, respectively.

4.4.3 Effective photon energy

The photon energy in target nucleon rest frame is also smeared by the Fermi motion. The photon energy in the frame is also obtained by MMSA (E_γ^{eff}) as

$$E_\gamma^{eff} = \frac{s - M_N}{2M_N}, \tag{4.12}$$

where s is the total center-of-mass energy of KKN system obtained by MMSA and M_N is mass of the nucleon. The improvement of the photon energy resolution in target nucleon rest frame is from 100MeV to 58MeV [61].

Figure 4.7 shows the invariant mass of the K^+ and K^- ($M(K^+K^-)$) for the previous data. Clear peak corresponds to ϕ meson is seen. Approximately 75% of the events are concentrated in the region of $1.01 \leq M(K^+K^-) \leq 1.03(GeV/c^2)$ (mass of the ϕ meson is $1.0194GeV/c^2$). Therefore, the rejection of the quasi-free ϕ meson photo-production events is very important for the Θ^+ search. When the E_γ^{eff} is close to the production threshold of the K^+ and K^-, both $M(K^+K^-)$ and M(NK) distributions are concentrated on their threshold. So it is hard to separate ϕ meson from Θ^+ or $\Lambda(1520)$ for low E_γ^{eff} region. Figure 4.8 shows the scatter plot of $M(K^+K^-)$ and $M(nK^+)$ for simulated quasi-free non-resonant KKn production for each E_γ^{eff} region. A large number of events are in the region where mass of ϕ meson and Θ^+ is overlapped for low E_γ^{eff} region (Fig. 4.8-(a),(b)). To reject the overlap region, Figure 4.9 shows the scatter plot of $M(pK^-)$ and $M(nK^+)$ for simulated quasi-free non-resonant KKn production for each E_γ^{eff} region. Again, a large number of events are in the region where mass of $\Lambda(1520)$ and Θ^+ is overlapped for low E_γ^{eff} region (Fig. 4.8-(a),(b)) To reject overlap region, a cut condition of $2.0 \leq E_\gamma^{eff}$ is applied.

The events which have large E_γ^{eff} also have a problem. They are dominated by coherent events or particle misidentification. Figure 4.10 shows the $MMd(\gamma, K^+K^-)X$ for the event with $E_\gamma^{eff} \geq 2.5$ GeV. The peak corresponds to coherent events and tail corresponds to K/π misidentification events are seen To reject such events, a cut condition of $E_\gamma^{eff} \leq 2.5$ GeV is also applied.

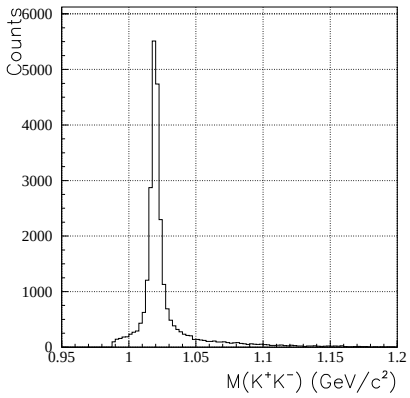

Figure 4.7: $M(K^+K^-)$ distribution for the previous data.

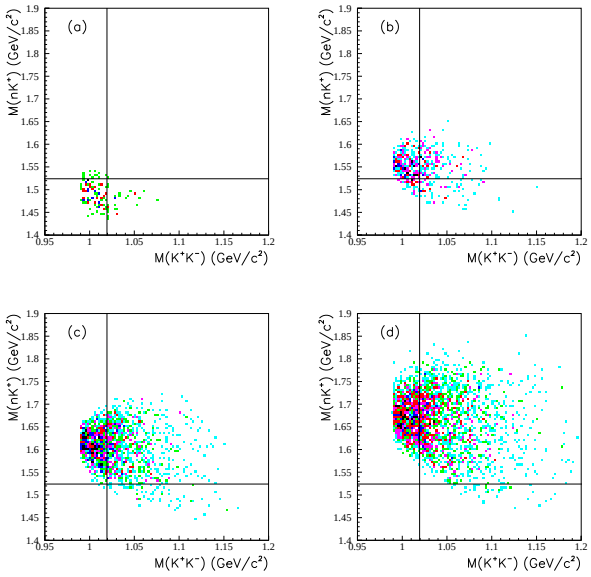

Figure 4.8: Scatter plot of $M(K^+K^-)$ and $M(nK^+)$ for simulated quasi-free non-resonant KKN production. (a) $E_\gamma^{eff} \leq 1.8$, (b) $1.8 \leq E_\gamma^{eff} \leq 2.0$, (c) $2.0 \leq E_\gamma^{eff} \leq 2.2$, (d) $2.2 \leq E_\gamma$, respectively. Vertical (horizontal) line shows the mass of the ϕ meson (Θ^+).

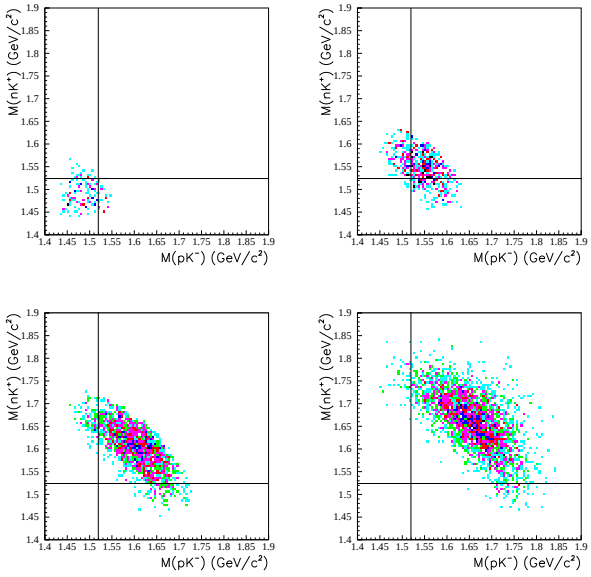

Figure 4.9: Scatter plot of $M(pK^-)$ and $M(nK^+)$ for simulated quasi-free non-resonant KKN production. (a) $E_\gamma^{eff} \leq 1.8$, (b) $1.8 \leq E_\gamma^{eff} \leq 2.0$, (c) $2.0 \leq E_\gamma^{eff} \leq 2.2$, (d) $2.2 \leq E_\gamma$, respectively. Vertical (horizontal) line shows the mass of the $\Lambda(1520)$ and the (Θ^+).

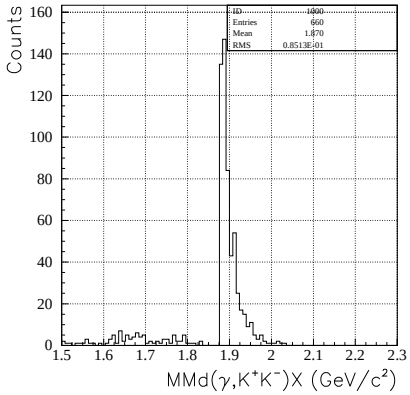

Figure 4.10: $MMd(\gamma, K^+K^-)X$ for the event with $E_\gamma^{eff} \geq 2.5$ GeV.

4.5 ϕ exclusion cut

As shown in Fig.4.7, the dominant contribution in selected K^+K^- detected sample is quasi-free ϕ photo-production, which is a background for the Θ^+ search. In this section, ϕ exclusion cut is discussed.

The analysis of the quasi-free production of the $\Lambda(1520)$, $\gamma p \to K^+\Lambda(1520)$ is closely related to the analysis of the quasi-free production of the Θ^+, $\gamma n \to K^-\Theta^+$ from following reasons.

- The acceptance of the LEPS spectrometer is the same for positive and negative charged particles.
- By interchanging the role of K^+ and K^-, $M(pK^-)$ becomes $M(nK^+)$, and acceptance of the LEPS spectrometer is symmetric for K^+ and K^-.
- The mass of the $\Lambda(1520)$ is very close to that of the Θ^+.
- For the ϕ photo-production, the $M(pK^-)$ and nK^+ spectra show the same shape.

The ϕ exclusion cut condition which are optimized for $\Lambda(1520)$ peak is expected to be also good for the Θ^+ search. Therefore, the ϕ exclusion cut condition is determined with checking $\Lambda(1520)$ peak in $M(pK^-)$ distribution. The cut conditions are determined based on two requirements.

- A high signal acceptance at the optimal cut point, and no large change of the signal acceptance when the cut is relaxed.
- A high rejection of the background at the optimal cut point, and the no large change of the S/N ratio when the cut point is tightened.

The ϕ events are rejected by following cut condition:

$$M(K^+K^-) > Offset + Slope \times (E_\gamma^{eff} - 2.0), \tag{4.13}$$

$$M(K^+K^-) > Const, \tag{4.14}$$

where Offset=1.02, Slope=0.09, and Const=1.03. Figure 4.11(a) shows the boundary of the ϕ exclusion cut. The ϕ exclusion cut is loose for low energy region because the $\Lambda(1520)$ and Θ^+ production events have an acceptance at low invariant mass region as shown in Fig.4.8. In contrast, the cut condition is tight for high energy region where the $\Lambda(1520)$ and Θ^+ production events have no acceptance in low invariant mass region. The yield and S/N of the $\Lambda(1520)$ peak as a function of ϕ exclusion cut parameters will be given in section 4.10.2 together with consistency check between the new data. Figure 4.11(b) shows the $M(nK^+)$ distribution before and after the ϕ exclusion cut for non-resonant KK MC sample. The acceptance for ϕ exclusion cut is high for threshold region where the momentum of K^+ and K^- are asymmetric while the acceptance is low for medium or high mass region where the momentum of K^+ and K^- are symmetric. However, the $M(nK^+)$ dependence of the acceptance is not large. The $M(nK^+)$ distribution after the ϕ exclusion does not show a sharp peak.

The $M(pK^-)$ and $M(nK^+)$ distributions before and after the ϕ exclusion cut for real data are shown in Fig. 4.12. For $M(pK^-)$, the peak corresponds to the $\Lambda(1520)$ is seen after the ϕ exclusion cut. For $M(nK^+)$, the peak corresponds to the Θ^+ is seen after the ϕ exclusion cut.

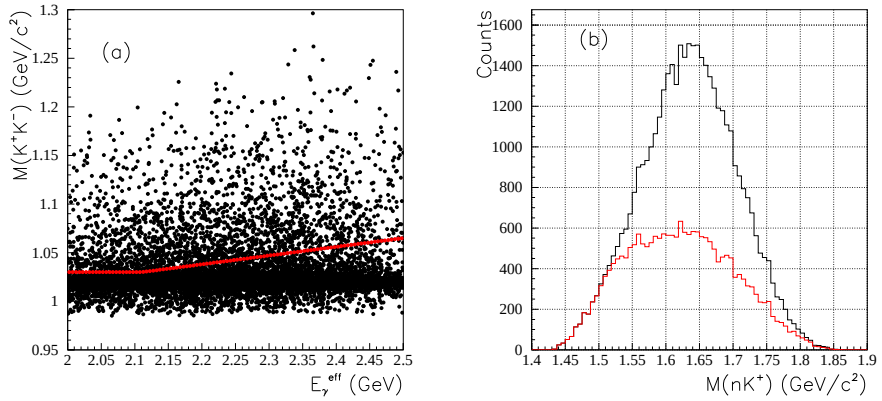

Figure 4.11: (a) Scatter plot of $M(K^+K^-)$ and E_γ^{eff} for the previous data. Red line shows the boundary of ϕ exclusion cut. (b) $M(nK^+)$ distribution for non-resonant KK MC. Black histogram is before the ϕ exclusion cut and red histogram is after the ϕ exclusion cut.

4.6 Rejection of the three tracks events.

Figure 4.13 (a) shows the number of tracks detected by the spectrometer after all the selection cut written above are applied. There are some events which three tracks exist. Most of the third tracks are proton. The lower bound of the momentum acceptance of the LEPS spectrometer is around 0.3 GeV/c, which is much larger than the average of the Fermi-momentum. Therefore, the event with three tracks are expected to be the quasi-free process from a proton. Figure 4.13 (b) and (c) shows the $M(pK^-)$ and $M(nK^+)$ distribution for three tracks events. A clear peak structure corresponds to $\Lambda(1520)$ is seen in $M(pK^-)$ distribution while no structure is seen in $M(nK^+)$ distribution. Because we are interested in the quasi-free process from a neutron, the

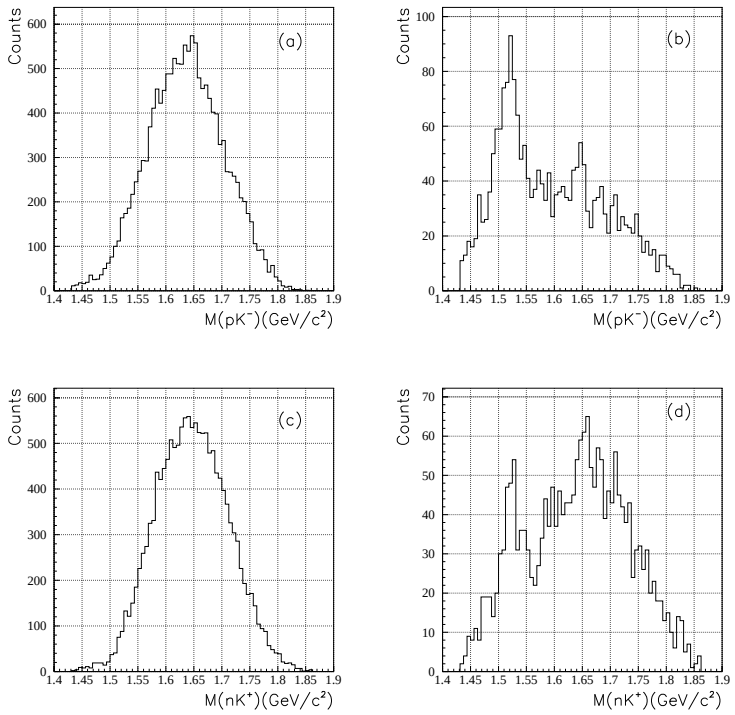

Figure 4.12: (a) $M(pK^-)$ before the ϕ exclusion cut. (b) $M(pK^-)$ after the ϕ exclusion cut. (c) $M(nK^+)$ before the ϕ exclusion cut. (d) $M(nK^+)$ after the ϕ exclusion cut.

three track events are rejected. Figure 4.13 (d) shows the $M(nK^+)$ distribution after rejecting three tracks events.

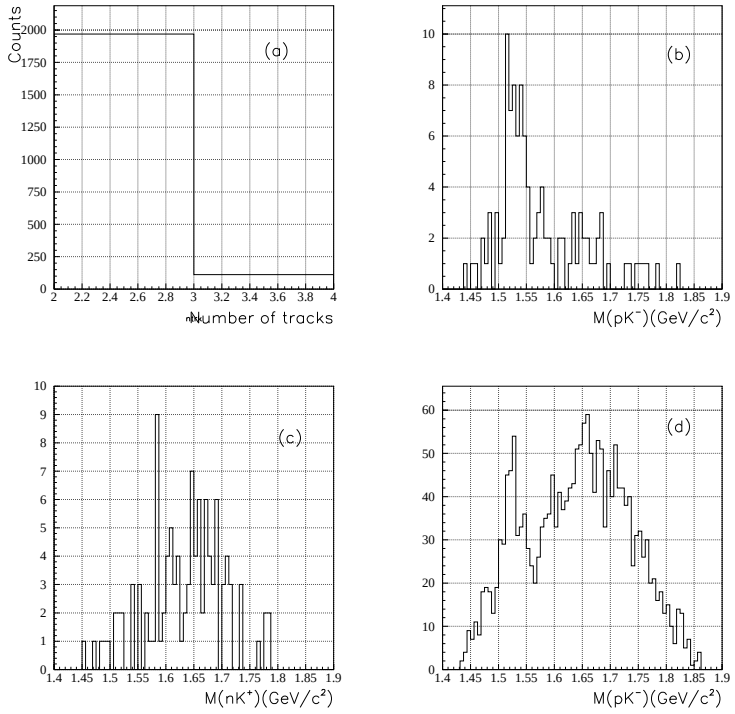

Figure 4.13: (a) The number of tracks after all the selection cut are applied. (b) $M(pK^-)$ distribution for three tracks events. (c) $M(nK^+)$ distribution for three tracks events. (d) $M(nK^+)$ distribution after rejecting three tracks events.

4.7 Randomized minimum momentum (RMM) method for the background estimation

In this section, the method to estimate the $M(nK^+)$ distribution for background events based on measured K^- missing mass $MMn(\gamma, K^-)X$ (RMM method) and its application to the the previous data are described.

4.7.1 Explanation of the RMM method

Figure 4.14 shows the scatter plots of p_{min} and $MMn(\gamma, K^-)X$ for MC simulated signal events and non-resonant KKn production events. Because the p_{min} represents the approximated Fermi-momentum, there is a strong correlation between p_{min} and $MMn(\gamma, K^-)X$ for signal (Θ^+ production) events while the correlation is very weak for the background events. The background events are characterized by the absence of the correlation.

Figure 4.15(a) shows the scatter plot of the mass correction ((δM=$M(nK^+)$-$MMn(\gamma,K^-)X$)) and p_{min}. A clear correlation is seen. The first step of the RMM method is to approximate δM by a 2nd order polynomial function of p_{min} ($=\delta M'$). The approximation is rather good. Figure 4.15(b) shows the $M(nK^+)$ and $M'(nK^+)$=($MMn(\gamma,K^-)X$+$\delta M'$) and $MMn(\gamma,K^-)X$ for signal MC events. The mass resolution of $M'(nK^+)$ is 12 MeV/c^2 while that for $M(nK^+)$ is 11 MeV/c^2. In this approximation, the invariant mass can be obtained from $MMn(\gamma,K^-)X$ and p_{min}.

The p_{min} for the background events have a random nature due to the Fermi-motion. The next step of RMM method is to replace the p_{min} with computer generated randomized one for many times (10^4 times). Then, the randomized p_{min} are combined with the $MMn(\gamma,K^-)X$ to obtain the $M'(nK^+)$. The obtained $M'(nK^+)$ distribution is called RMM spectrum, which represents the $M(nK^+)$ distribution for background events. In the randomization, the p_{min} distribution is assumed to be Gaussian. Because there is a weak correlation between mean, RMS of the p_{min} and $MMn(\gamma,K^-)X$ at the tail region of the $MMn(\gamma,K^-)X$, they are varied as a function of the $MMn(\gamma,K^-)X$. The origin of the correlation is mainly due to the difference of the kinematic domain between $MMn(\gamma,K^-)X$ and $M(nK^+)$. To make the $MMn(\gamma,K^-)X$ much smaller than the threshold of nK^+, Fermi-momentum must be very large. Figure 4.15(c) shows a scatter plot of $MMn(\gamma,K^-)X$ and mean of the $p_{min}\pm 1\sigma$. The validity of the RMM method is checked by MC. Figure 4.15 shows the $M(nK^+)$ distribution and RMM spectrum for non-resonant KKn events. The number of events for RMM spectrum is normalized to the number of events for $M(nK^+)$ distribution. The RMM spectrum reproduce the $M(nK^+)$ distribution reasonably well. The same method can be applied to estimate the $M(pK^-)$ distribution from $MMp(\gamma,K^+)X$.

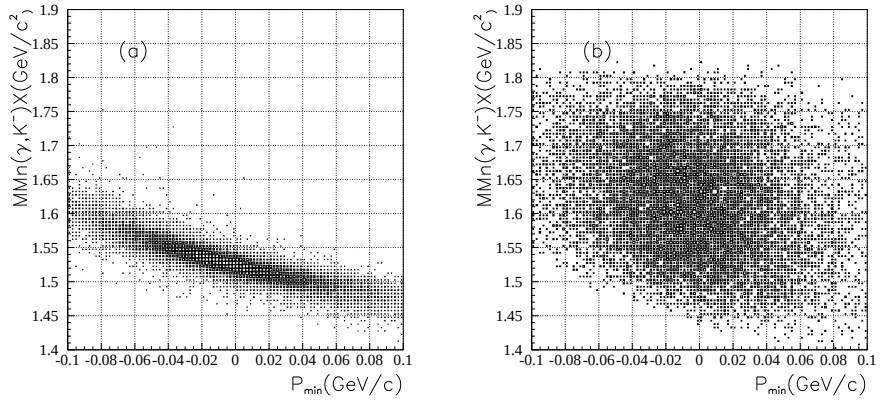

Figure 4.14: The scatter plots of p_{min} and $MMn(\gamma,K^-)X$ for MC events. (a) Signal event. (b) Non-resonant KKn production.

The RMM method is similar to the mixed event technique which is used to estimate the combinatorial background. The common problem for two methods is signal contamination. In the case of RMM, the signal contamination cause the overestimation of the background level if the entries in the histograms for RMM spectrum and reconstructed mass spectrum are the same.

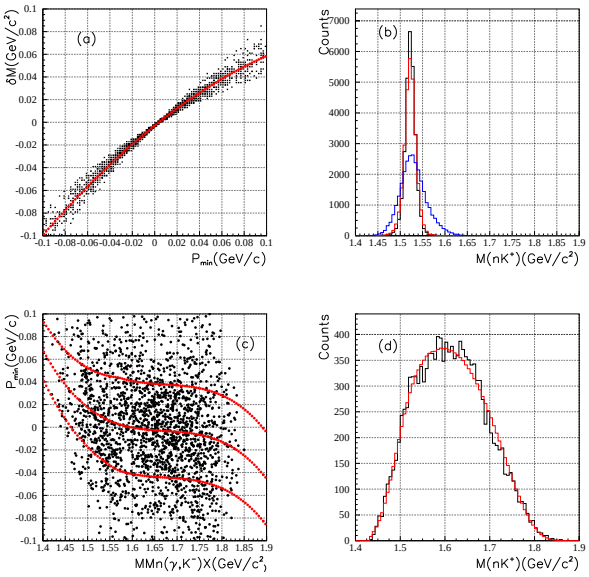

Figure 4.15: (a) A scatter plot of δM=$M(nK^+)$-$MMn(\gamma, K^-)X$ and p_{min}. Red line is result of the fitting by a 2nd order polynomial function. (b) Various mass calculation for signal MC event. Black:$M(nK^+)$. Red:$M'(nK^+)$. Blue: $MMn(\gamma, K^-)X$. (c) A scatter plot of $MMn(\gamma, K^-)X$ and p_{min}. Red lines show the mean of the $p_{min} \pm 1\sigma$. (d) Black histogram is $M(nK^+)$ distribution and red one is RMM spectrum for non-resonant KKn events.

The final step of the RMM method is to divide the $M(nK^+)$ or $M(pK^-)$ into several subsets. We call them seed sets. The boundaries for the one of the seed sets are selected to cover the signal region. The RMM spectrum for signal seed set is very similar to the background events even when the region is very narrow because the RMM spectrum can not be narrower than 30 MeV/c^2. The background spectrum is represented by the sum of the RMM spectra for all seed sets. The relative weight for each subsets are treated as fitting parameters. The effect of the signal contamination is absorbed by decreasing the weight parameter for the signal seed set.

The statistical significance of the signal is calculated from the difference in log likelihood between fits with and without the signal contribution represented by a gaussian. the width of the gaussian is fixed to be the value obtained by mc. they are 11 mev/c^2 for θ^+ peak and 16 mev/c^2 for $\lambda(1520)$ peak. the change in the number of the degree of freedom is 2, which is taken into account for the significance calculation.

4.7.2 application of the rmm method to previous data.

figure 4.16 (a) shows the $m(nk^+)$ distribution for the previous data after all the selection cut with a fit with rmm spectrum taken from [48]. three seed sets of $m(nk^+) < 1.50$ gev/c^2, $1.50 < m(nk^+) < 1.55$ gev/c^2, $m(nk^+) > 1.55$ gev/c^2 are used for the background estimation. the -2lnl value of the fit changed from 104.7 (for ndf=66), to 73.64 (for ndf=64) by including a gaussian function. the statistical significance of the signal estimated from δ(-2lnl) is 5.2 σ.

the peak position for the best fit is $1.524 \pm 0.002 + 0.003$ gev/c^2, where the systematic shift of the peak position of $+3$ mev/c^2 due to the fermi-motion correction by mmsa and ϕ exclusion cut is given as the systematic uncertainty. the signal yield was estimated to be 116±21 events obtained from the gaussian height and its uncertainty.

the relatively large value of -2lnl in the fitting of the $m(nk^+)$ is due to the reflection of the $\lambda(1520)$ events. for $\lambda(1520)$ events, there exists correlation between $mmn(\gamma, k^-)x$ and p_{min}. to avoid the possible effect due to the reflection, an additional cut of $m(pk^-) > 1.55$ gev/c^2 is applied and the fitting region is restricted to be 1.65 gev/c^2 as shown in figure 4.16 (b). the fit qualities are improved, giving -2lnl/ndf=55.2/33 and -2lnl/ndf=24.8/31 for the case with and without the θ^+ contribution, respectively. however, the significance is almost unchanged because the change of δ(-2lnl) is unchanged.

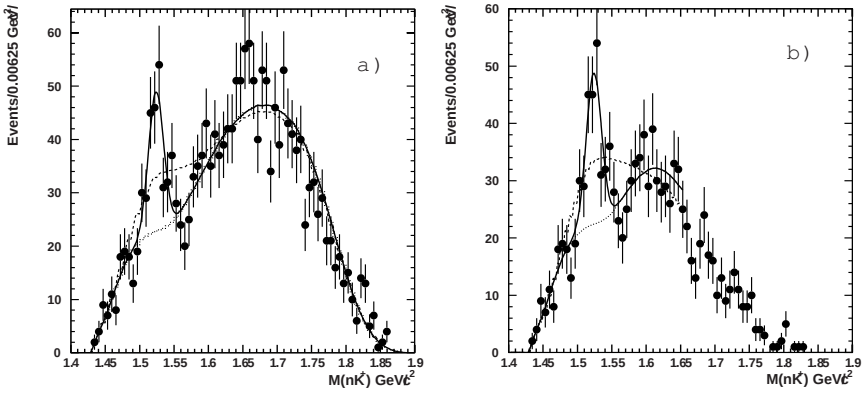

Figure 4.16: (a)the $m(nk^+)$ distribution for the previous data with a fit with rmm spectrum only (dashed line) and with a gaussian function (solid line) taken from [48]. the dotted line is the background. (b) the $m(nk^+)$ distribution with a cut condition of $m(pk^-) > 1.55$ gev/c^2.

4.8 comparison of the expected nk^+ invariant mass resolution

from this section, several comparisons between the previous data and the new data are described. there are two purpose for the comparison of two data sets. one is to check if there are any problems for the new data (or possibly for the previous data). the other is to determine whether it is possible to combine two data sets after we open the box or not. that means to check if the mass resolution and acceptance for two data sets are essentially the same.

as written in section 3.6, the dc resolution is better for the new data and photon energy resolution is slightly better for the previous data. the effect of these differences on the invariant mass resolution is studied by mc. figure 4.17 shows the $m(nk^+)$ distribution for signal mc samples. the resolution and efficiency parameters of the detectors for each data set are used. the $m(nk^+)$ resolution is 10.9 ± 0.1 mev/c^2 for the previous data and 10.8 ± 0.1 mev/c^2 for the new data. the mass resolution is almost the same for two data sets. this is because the invariant mass resolution is dominated by the fermi-motion correction.

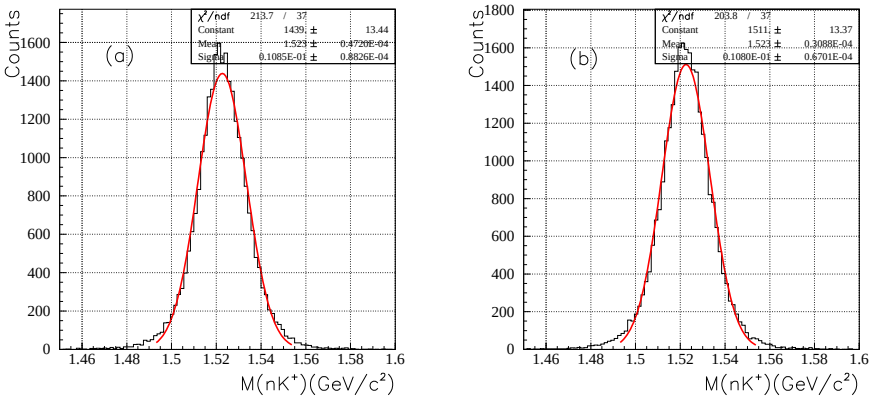

Figure 4.17: $m(nk^+)$ distribution for signal mc sample. (a) the parameters for the previous data are used. (b) the parameters for the new data are used.

4.9 comparison of the ϕ events.

as written in section 4.5, the dominant contribution in the k^+ and k^- detected sample is ϕ meson production. because the statistics of the ϕ meson production is high and they are rejected in the θ^+ search, ϕ meson production is a good probe to check the consistency of the calibration and the acceptance between two data sets without seeing the signal samples. in this section, several plots for ϕ events are compared.

4.9.1 masking θ^+ region

to keep the blind analysis, θ^+ region is masked at this stage. in the lepsana, events which satisfy the condition $m(k^+k^-) > 1.03\ gev/c^2$, $mmn(\gamma, k^-)x < 1.6\ gev/c^2$, and # of tracks=2 simultaneously are not filled in the ntuple. figure 4.18 shows the $m(nk^+)$ distribution for masked sample. almost no events exists in the θ^+ mass region.

4.9.2 minimum momentum distribution

as written in section 4.4, the minimum momentum spectator approximation (mmsa) and the minimum momentum (p_{min}) play a key role in the θ^+ search. in this section, consistency of the p_{min} distribution of ϕ events for two data sets are checked. ϕ events are selected by a cut condition of $1.01 < m(k^+k^-) < 1.03\ gev/c^2$. to reduce the effect of difference of the photon energy distribution for two data sets due to using different lasers as written in section 2.2.2, a cut condition of $2.0 < e_\gamma < 2.35\ gev$ is applied.

figure 4.19 (a) shows the p_{min} distributions for two data sets. two data sets are normalized by number of events. figure 4.19 (b) shows the ratio of two histograms in fig. 4.19 (a) with a fitting by a constant value. the χ^2/ndf of the fitting is 121.6/90, which is not so good. to check the consistency further, the kolmogorov-smirnov (k.s) test, which is widely used to test whether the distribution of two histograms are different [71]. the result of k.s test is 0.013%, (which

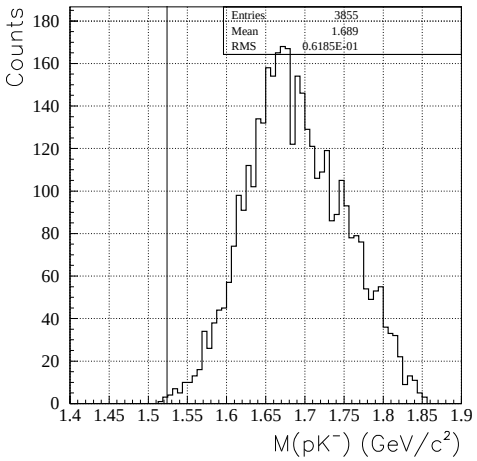

Figure 4.18: $m(nk^+)$ distribution after all the selection cut are applied with masked sample. vertical line shows the mass of θ^+ obtained by previous result ($1.524\,gev/c^2$)[48].

means that if two histograms have the same probability density function, the probability that the consistency becomes worse than this case is 0.013%) which is not good again.

we investigated if the consistency become good by changing the momentum scale of the new data. figure 4.19 (c) shows the same as fig. 4.19 (a) but the momentum scale factor is changed from 1.006 to 1.007 (the determination of momentum scale factor of 1.006 is written in section 3.5.3). figure 4.19 (d) shows the ratio of two histograms in fig. 4.19 (c) with a fitting by a constant value. the χ^2/ndf of the fitting is 96.6/90, which rather good. the result of the k.s test is 52.4%, which is again much better. these results indicate that the scales of momentum are different for two data sets with a factor of 0.1%.

the momentum scale factor of 1.008 is also tried (fig. 4.19 (e),(f)). the consistency of two data sets are better for the case of 1.007. the consistency of the p_{min} distribution is summarized in table 4.1.

momentum scale	1.006	1.007	1.008
χ^2/ndf	121.6/90	96.6/90	105.8/90
k.s test	0.01%	52.4%	0.1%

Table 4.1: summary of the consistency check of p_{min} distribution

4.9.3 $mmd(\gamma, k^+k^-)x$ distribution

in the missing mass of the k^+ and k^- assuming that the target is a deuteron at rest, $mmd(\gamma, k^+k^-)x$, the coherent process, $\gamma d \to \phi$d, makes a peak at the deuteron mass. on the other hand, for the incoherent process, $\gamma d \to \phi pn$, the missing mass is distributed at the higher mass region because one of the nucleons is struck and hence the pn invariant mass becomes large. because

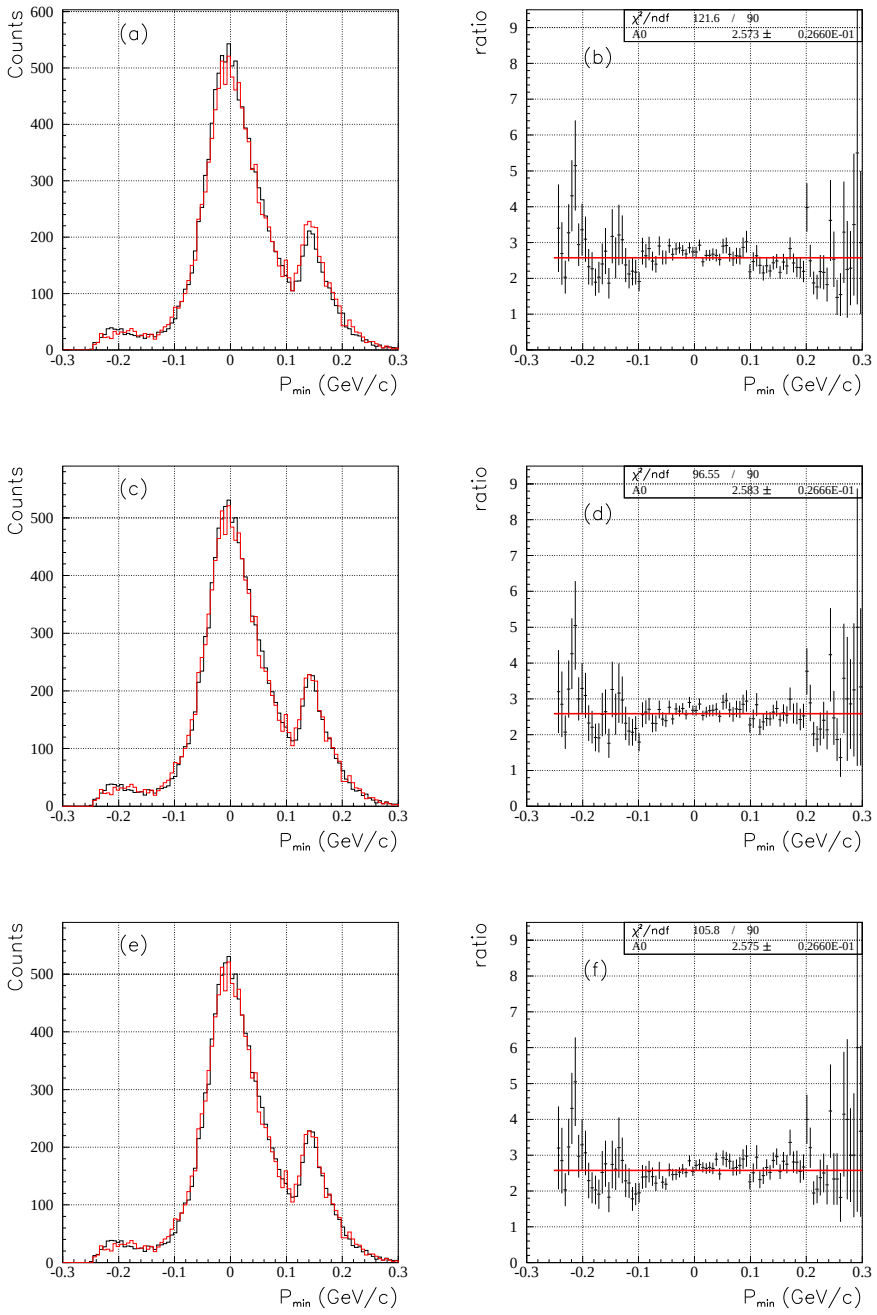

Figure 4.19: (a) the p_{min} distribution. black histogram is for the new data and red histogram is for the previous data. two histograms are normalized by the number of events. the momentum scale factor for the new data is 1.006. (b) the ratio of black and red histograms of plot (a). the fitting line is constant. (c) the same as plot (a) but the momentum scale factor for the new data is 1.007. (d) the ratio of black and red histograms of plot (c). (e) the same as plot (a) but the momentum scale factor for the new data is 1.008. (f) the ratio of black and red histograms of plot (e).

the fermi-motion correction is not necessary to observe the peak corresponds to the coherent process, the $mmd(\gamma, k^+k^-)x$ is a good probe to check the calibration. figure 4.20 shows the comparison of $mmd(\gamma, k^+k^-)x$ for various momentum scale factors. the fitting region by a constant value is limited to [1.85:2.1] because large tail component exists for the previous data. the origin of the tail component is setting of the maximum number of accepted hits for dcs (depth) for the previous data as written in section 3.6.1. the consistency of the $mmd(\gamma, k^+k^-)x$ is summarized in table 4.2. again, the momentum scale factor of 1.007 for the new data gives the good consistency.

momentum scale	1.006	1.007	1.008
χ^2/ndf	107.0/83	90.4/83	103.5/90
k.s test	0.1%	63.8%	7.7%

Table 4.2: summary of the consistency check of $mmd(\gamma, k^+k^-)x$ distribution.

4.10 comparison of the $\lambda(1520)$ peak in the k^+ k^- detection modes.

4.10.1 $m(pk^-)$ distribution with all the selection cut

figure 4.21 shows the $m(pk^-)$ distribution for each data set. as written in section 4.9.1, in addition to the standard cut conditions, the cut condition $mmn(\gamma, k\ -)x > 1.6\ gev/c^2$ is applied to keep the blind analysis for both data sets. no big difference between two histograms is seen. figure 4.21 shows the $m(pk^-)$ distribution for each data set. figure 4.22 shows the same as figure 4.21 but the peak is fitted with gaussian and linear background. gaussian σ is fixed to be 16 mev/c^2, which is obtained by mc. figure 4.23 shows the same as figure 4.21 but the peak is fitted with gaussian and linear background. gaussian σ is also a free parameter. the evaluation of the peak is summarized in table 4.3. note that the values other than gaussian σ is taken from the fitting result with fixing gaussian σ to reduce the fluctuation. s/n ratio is obtained by dividing the gaussian height by the height of background at the mean of the gaussian. the gaussian mean, gaussian σ, s/n ratio are consistent for two data sets. the consistency of the peak position between two data sets is better for the scale factor of 1.006. however, the error bar is too large to conclude which momentum scale is better.

	previous	new (1.006)	new (1.007)
gaussian mean (mev/c^2)	1517.6±1.6	1517.8±1.0	1518.8±1.0
gaussian σ (mev/c^2)	18.5±2.2	16.8±1.6	16.8±1.6
gaussian height	53.0±5.2	128.3±8.2	125.4±8.1
s/n ratio	1.73 ±0.22	1.55±0.15	1.51±0.15

Table 4.3: summary of the evaluation of $\lambda(1520)$ peak.

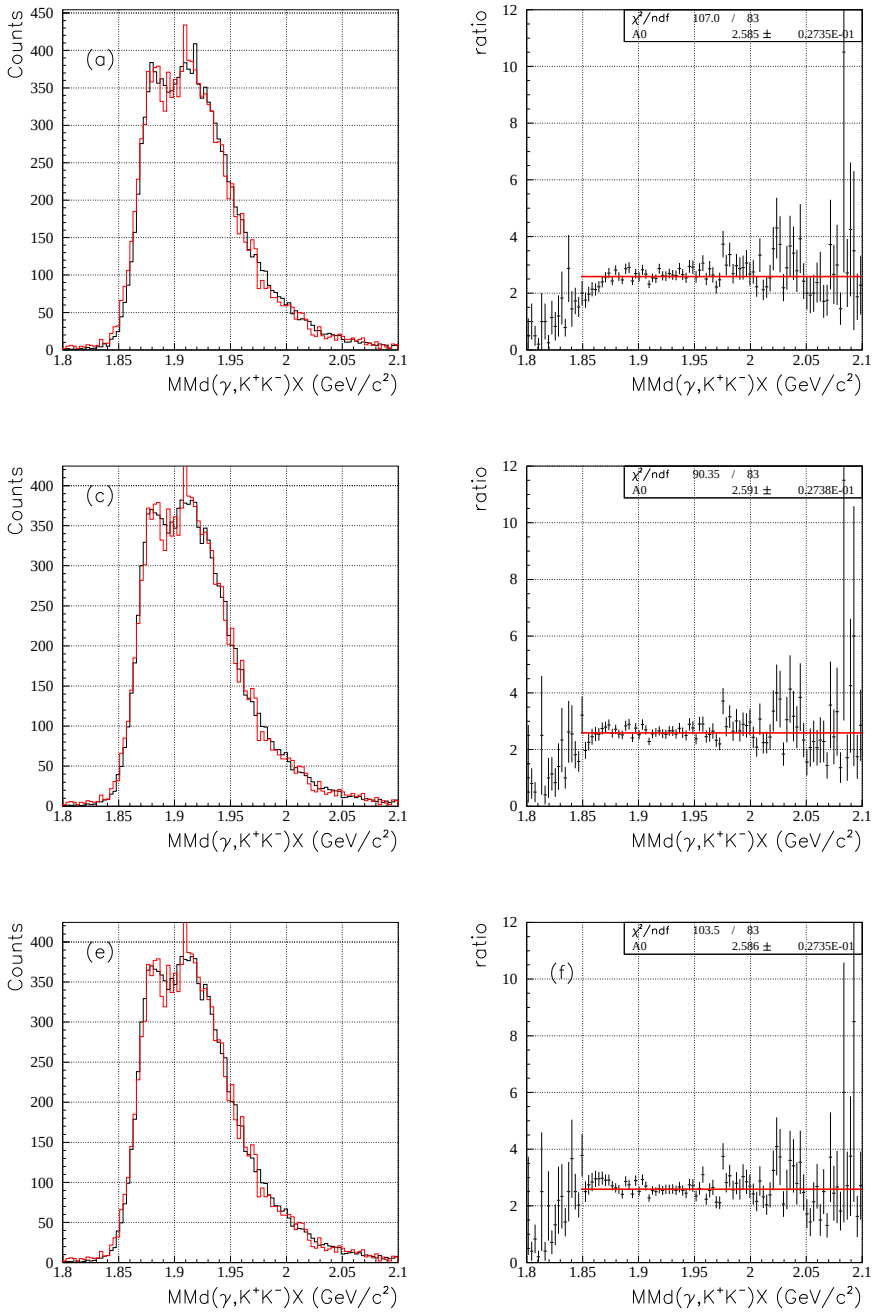

Figure 4.20: (a) the $mmd(\gamma, k^+k^-)x$ distribution. black histogram is for the new data and red histogram is for the previous data. two histograms are normalized by the number of events. the momentum scale factor for the new data is 1.006. (b) the ratio of black and red histograms of plot (a). the fitting line is constant. (c) the same as plot (a) but the momentum scale factor for the new data is 1.007. (d) the ratio of black and red histograms of plot (c). (e) the same as plot (a) but the momentum scale factor for the new data is 1.008. (f) the ratio of black and red histograms of plot (e).

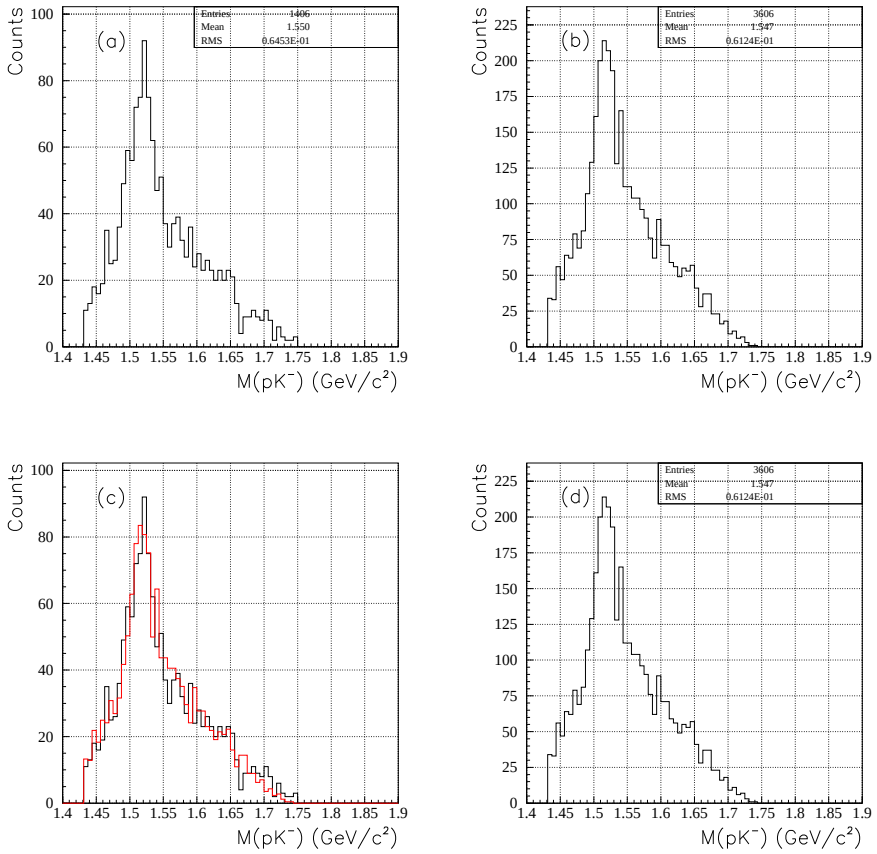

Figure 4.21: $m(pk^-)$ distribution. (a) the previous data. (b) the new data with a scale factor of 1.006. (c) plot (a) and (b) are superimposed. two histograms are normalized by the number of events. black is histogram is for the previous data and red histogram is for the new data. (d) the new data with a scale factor of 1.007.

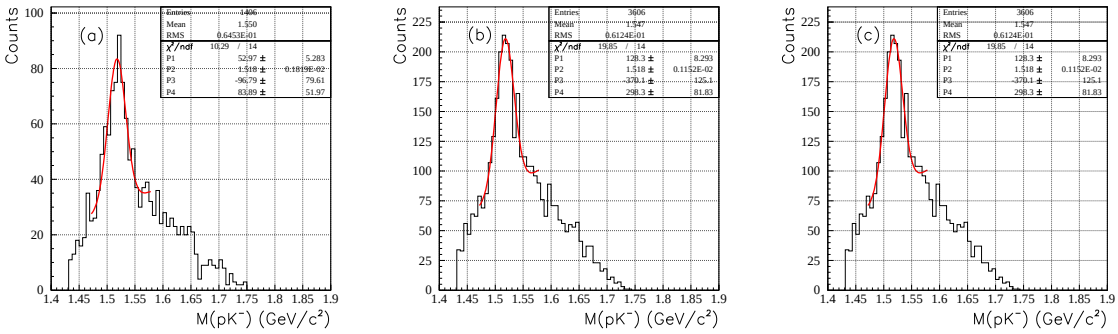

Figure 4.22: $m(pk^-)$ distribution. fitting function is gaussian plus a linear background. gaussian σ is fixed to be 16 mev/c^2. (a) previous data. (b) the new data with a momentum scale factor of 1.006. (c) the new data with a momentum scale factor of 1.007.

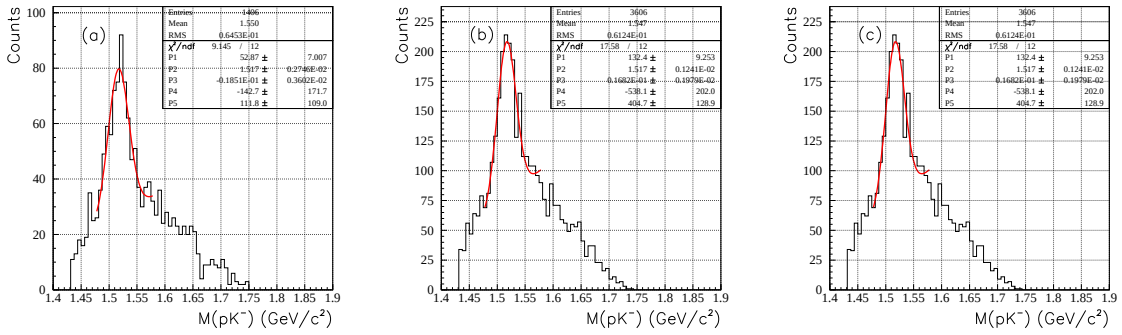

Figure 4.23: $m(pk^-)$ distribution. fitting function is gaussian plus linear background. gaussian σ is also a free parameter. (a) previous data. (b) the new data with a momentum scale factor of 1.006. (c) the new data with a momentum scale factor of 1.007.

4.10.2 ϕ exclusion cut parameter dependence of the $\lambda(1520)$ peak

as written in section 4.5, the ϕ exclusion cut condition was determined by checking $\lambda(1520)$ peak. it is important to check if the ϕ exclusion cut condition optimized for the previous data is also good for the new data.

when the ϕ exclusion cut is loosened, the s/n ratio of the $\lambda(1520)$ peak becomes worse due to the contamination from ϕ events. in such a case, fitting by assuming background is linear function does not give a correct result. the rmm is more suitable for the estimation of the background than the simple linear function when the s/n ratio is not good. however, the rmm method cannot be used when the mask condition $mmn(\gamma, k-)x > 1.6\ gev/c^2$ is applied because the relation between simple missing mass and minimum momentum is disturbed and correlation between these variables appears. to keep the blind analysis without the masking condition, we created ntuple which contains only limited kinematic variables like $m(pk^-)$. the kinematic variables filled in the ntuple are summarized in table 4.4. the $m(pk^-)$ distribution for the new data without masking condition is shown in 4.24.

$mmp(\gamma, k^+)x$
$m(pk^-)$
$m(k^+k^-)$
e_γ^{eff}
p_{min}
e_γ
$\#\ of\ tracks$

Table 4.4: list of the variables filled in the special ntuple.

as written in section 4.5, three parameters (offset, slope, const) are used. when a certain parameter for the ϕ exclusion cut is changed, the remaining two parameters are fixed at the optimized point. figure 4.25 shows the slope dependence of the peak height of the $\lambda(1520)$

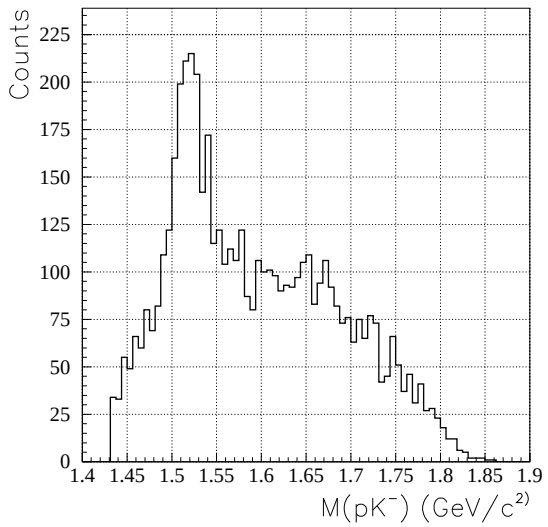

Figure 4.24: the $m(pk^-)$ distribution for the new data without masking condition.

and fig.4.26 shows the slope dependence of the s/n ratio of the $\lambda(1520)$ for two data sets. vertical lines show the optimized cut point (0.09). the cut is tighter for larger slope values, and relaxed for smaller values. figure 4.27 shows the offset dependence of the peak height of the $\lambda(1520)$ and fig.4.26 shows the offset dependence of the s/n ratio of the $\lambda(1520)$ for two data sets. vertical lines show the optimized cut point (1.02). the cut is tighter for larger slope values, and relaxed for smaller values. the peak height does not increase much when the cut is relaxed from optimized point and the s/n ratio does not become better largely when the cut is tightened from optimized point for both data sets. however, the parameter dependence of the peak height and s/n ratio is more steep for the new data. they are summarized in table 4.5. the error bars in table 4.5 are obtained by using mc. the quasi-free $\lambda(1520)$ production, ϕ photo production, and non-resonant kkp events generated by mc are combined. the number of generated events for each mode were tuned so that the number of events which pass all the cut conditions and characteristic spectrum like $m(k^+k^-)$ and $m(pk^-)$ are consistent with real data. then, such combinations are created many times. peak height and s/n ratio normalized by the optimized points are obtained for each combinations. then, the r.m.s of the many trials are identified as the error bar. the difference of the two data sets in Table 4.5 exceed the error bar. Although we could not identified the reason for the inconsistency, we decided to use the same ϕ exclusion cut condition for the new data because the cut point itself seems to be also good for the new data.

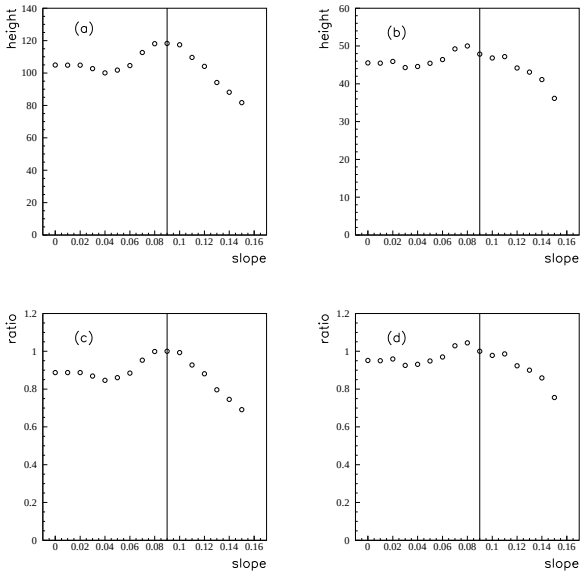

Figure 4.25: The slope parameter dependence of the peak height of the $\Lambda(1520)$ peak. Vertical line shows the optimized point. (a) The new data. (b) the previous data. (c) The new data. Normalized by optimized point. (d) previous data. Normalized by optimized point.

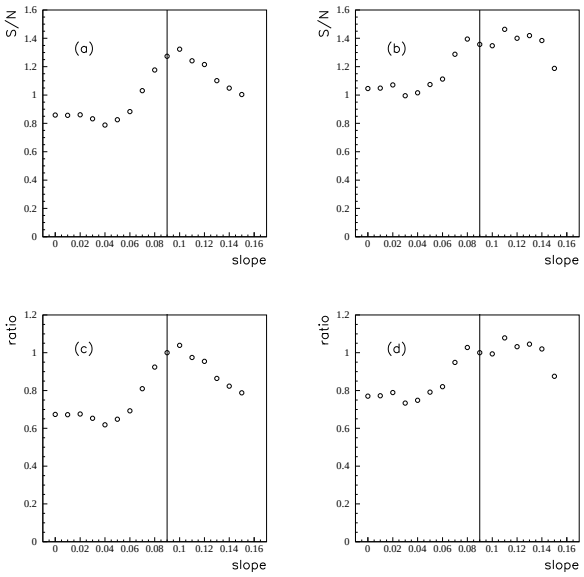

Figure 4.26: The slope parameter dependence of the S/N ratio of the $\Lambda(1520)$ peak. Vertical line shows the optimized point. (a) The new data. (b) the previous data. (c) The new data. Normalized by optimized point. (d) the previous data. Normalized by optimized point.

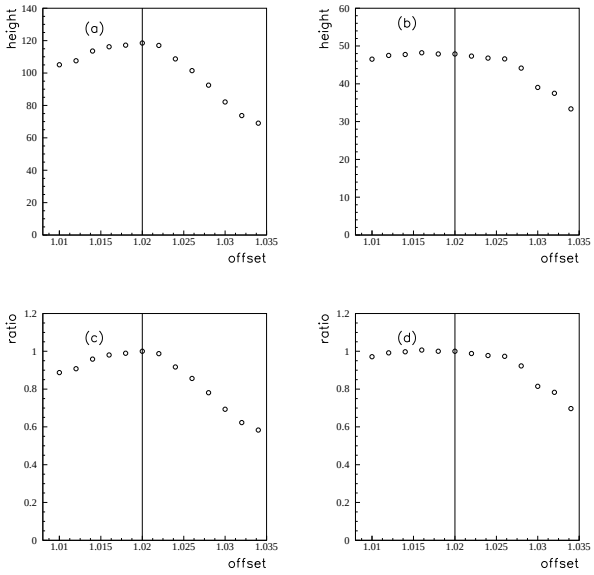

Figure 4.27: The offset parameter dependence of the peak height of the Λ(1520) peak. Vertical line shows the optimized point. (a) The new data. (b) the previous data. (c) The new data. Normalized by optimized point. (d) the previous data. Normalized by optimized point.

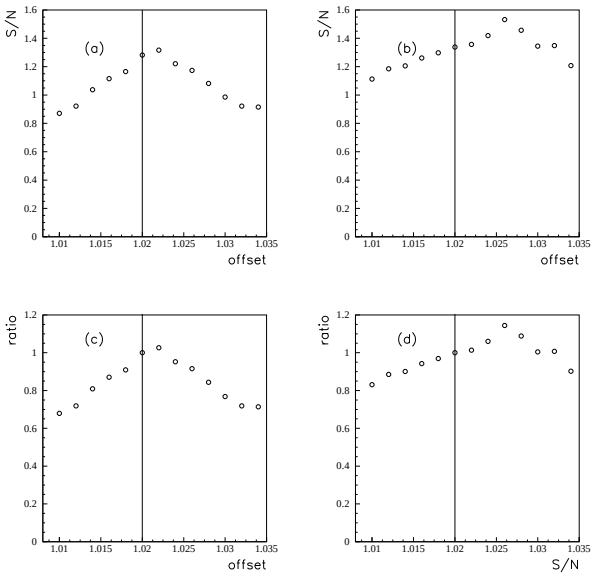

Figure 4.28: The offset parameter dependence of the S/N ratio of the Λ(1520) peak. Vertical line shows the optimized point. (a) The new data. (b) the previous data. (c) The new data. Normalized by optimized point. (d) the previous data. Normalized by optimized point.

	slope=0.0	slope=0.15	offset=1.01	offset=1.034
peak height (new data)	0.89 ±0.02	0.69±0.02	0.89±0.02	0.58±0.02
peak height (previous data)	0.95 ±0.04	0.76±0.04	0.97±0.03	0.69±0.04
S/N ratio (new data)	0.67 ±0.02	0.79±0.04	0.68±0.02	0.71±0.05
S/N ratio (previous data)	0.77 ±0.03	0.87±0.07	0.83±0.04	0.90±0.08

Table 4.5: Summary of the ϕ exclusion cut parameter dependence of the $\Lambda(1520)$ peak. The peak height and the S/N ratio normalized by optimized value are listed.

4.11 Comparison of the $MMn(\gamma, K^-)X$ distribution for final sample

The simple missing mass of the K^-, $MMn(\gamma, K^-)X$, is a good probe to check the acceptance and global consistency of the final sample without violating the policy of the blind analysis. To keep the condition of blind analysis, in the LEPSana, the $MMn(\gamma, K^-)X$ is filled in the histogram and no kinematic information are filled in the NTUPLE. Figure 4.29 shows the $MMn(\gamma, K^-)X$ for two data sets. The χ^2/ndf is 56.3/56 and K.S test gives the probability of 70.4 %, which are good.

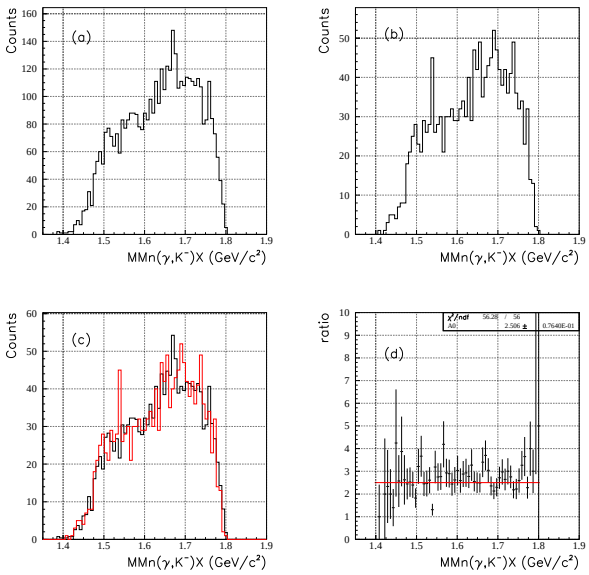

Figure 4.29: The $MMn(\gamma, K^-)X$ distribution with all the selection cut. (a) For the new data. (b) For the previous data with all the selection cut. (c) Plots (a) and (b) are superimposed. Two histograms are normalized by number of entries. (d) The ratio of plot (a) and plot (b) with a fitting by a constant value.

4.12 Rejection of the unphysical background

Figure 4.30(a) shows the $MMp(\gamma, K^+K^-)X$ for the new data after all the selection cut are applied. There exist some events in low mass region where physical events can not reach. These events are seen only in the new data. Figure 4.30(b) shows the mass squared reconstructed by momentum and TOF measurement which are identified as K^+ or K^-. For the unphysical events, the mass squared for either or both of tracks are low. Therefore, unphysical events are π/K miss identification. To reject these events, a cut condition of $MMp(\gamma, K^+K^-)X \geq 0.8\,GeV/c^2$ is imposed, which has no acceptance for the signal events.

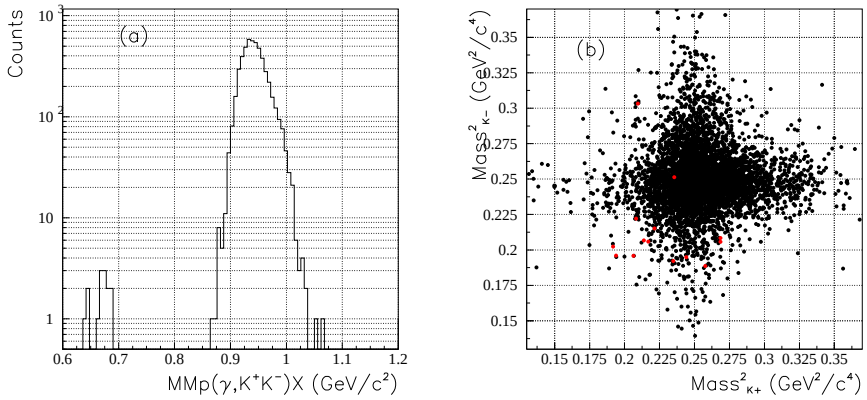

Figure 4.30: (a)$MMp(\gamma, K^+K^-)X$ after all the selection cut are applied for the new data. (b)A scatter plot of mass squared for K^+ and K^-. Black (red) points are for $MMp(\gamma, K^+K^-)X \geq 0.8\,(GeV/c^2)$ ($MMp(\gamma, K^+K^-)X \geq 0.8\,(GeV/c^2)$)

4.13 Summary of the cut statistics

Cut statistics for the two data sets are summarized in table 4.6 (previous data) and table 4.7 (new data).

Cut	Examined	passed	Rejection
K^+K^- ID	—	37172	—
Vertex	37172	30838	1.20
Decay-in-flight	30838	27059	1.14
Tagger	27059	25818	1.05
p_{min}	25818	18569	1.39
E_γ^{eff}	18569	14912	1.24
ϕ exclusion cut	14912	2080	7.17
Number of tracks	2080	1969	1.06
Unphysical BG	1969	1969	1.0

Table 4.6: Summary of the cut statistics for the previous data.

Cut	Examined	passed	Rejection
K^+K^- ID	—	103336	—
Vertex	103336	86233	1.20
Decay-in-flight	86233	80755	1.07
Tagger	80755	65750	1.23
p_{min}	65750	49070	1.34
E_γ^{eff}	49070	39226	1.25
ϕ exclusion cut	39226	5388	7.28
Number of tracks	5388	5106	1.06
Unphysical BG	5106	5092	1.003

Table 4.7: Summary of the cut statistics for the new data.

Chapter 5

Results

5.1 Box open

Figure 5.1 (a) shows the $M(nK^+)$ distribution for the new data after all the selection cut are applied. Figure 5.1 (b) shows the $M(nK^+)$ distribution with an additional $\Lambda(1520)$ cut ($M(pK^-) \geq 1.55\ GeV/c^2$). No strong narrow peak structure is seen. For the estimation of the significance, only the plot with $\Lambda(1520)$ cut is used because the reflection of the $\Lambda(1520)$ can not be neglect for high statistics data and RMM method can not be applied if we include the high mass region for the fitting. Figure 5.2 (a), (b) show the $M(nK^+)$ distribution with a fitting of RMM spectrum only and RMM spectrum plus Gaussian with a fixed width of 11 MeV/c^2. The Δ(-2lnL) is 4.3, which corresponds to the statistical significance of 1.6 σ. The peak position is 1513 $\pm$ 5 MeV/c^2, which is lower than the result of the previous data (1524 $\pm$ 2 MeV/c^2). The Gaussian height is 13 $\pm$ 7. The RMM method is tried with several fitting ranges. The fitting range of 1.47-1.65 GeV/c^2 gives the highest statistical significance of 1.9 σ (Fig.5.2 (c), (d)).

5.2 Consistency of two data sets

The statistical test of the consistency of the $M(nK^+)$ distribution for the two data sets are performed. Figure 5.3 (a) shows the $M(nK^+)$ distribution for two data sets. The momentum scale factor of 1.007 is used for the new data. Two histograms are normalized by the entries. The result of χ^2 test is shown in Fig.5.3 (b). The χ^2/ndf is 115.4/66, which is not good. The origin of the bad χ^2 value is high mass region. Actually, if the fitting region is restricted to below the 1.8 GeV/c^2, the χ^2/ndf is 54.0/58, which is good as shown in Fig. 5.3 (c). The origin of the inconsistency in high mass region is difference in the photon energy spectrum for two data sets. Figure 5.3 (d) shows the $M(nK^+)$ distribution with a photon energy cut of $2.0 \leq E_\gamma \leq 2.35$. As shown in Fig. 5.3 (e), the χ^2/ndf after the photon energy cut is 56.39/66, which is good. The result shows that the no big differences of acceptance exists between two data set as expected. However, there is a clear difference in the signal region for two data sets. To check the consistency between two data sets in the signal region, the χ^2 of the fitting in the space of mean and height of the Gaussian is investigated. Figure 5.4 (a) shows the contour of the increment of the χ^2 from the best fit in the space of mean and height of the Gaussian for

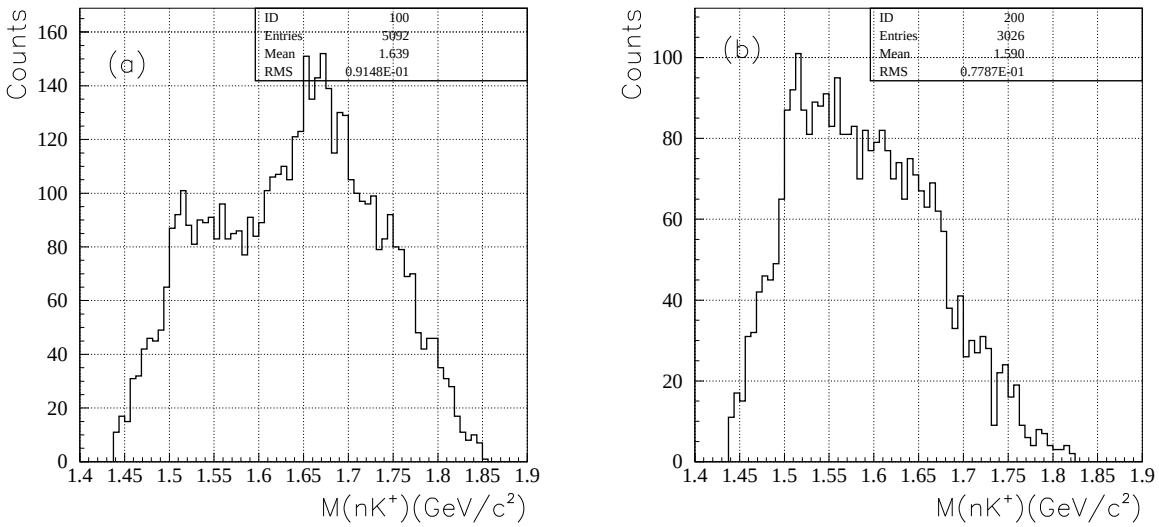

Figure 5.1: $M(nK^+)$ distribution for the new data after all the selection cut are applied. (a) Without $\Lambda(1520)$ cut. (b) With $\Lambda(1520)$ cut.

two data sets. For the evaluation of the new data, peak height of the Gaussian was scaled by ratio of entries for two data sets. At the closest point, the result of the fittings are deviated almost 3 σ from two data sets. To check the effect of the fluctuation of the background shape, the RMM spectrum produced from summed data is tried for both data sets. The result is shown in Fig. 5.4 (b). No big difference is observed.

5.3 Summing two data sets

Although the difference of the peak height and position of the Θ^+ between the two data sets is large, from the analysis of ϕ events (section 4.9), $\Lambda(1520)$ events (section 4.10) , simple K^- missing mass (section 4.11), and global consistency of the final $M(nK^+)$ distribution (previous section), no essential difference between two data sets was observed. Therefore, we summed two data sets and signal significance has been evaluated. From the analysis of the ϕ events (in section 4.9), it was found that the global scale of the momentum is different for two data sets by a factor of 0.1%. It is necessary to tune it. Two ways are tried. They are increasing (decreasing) the momentum scale factor for the new data (previous data) by a factor of 0.1%. Figure 5.5 (a), (b) shows the $M(nK^+)$ distribution for summed data with (without) the $\Lambda(1520)$ cut. The momentum scale of the new data was increased by a factor of 0.1 %. Figure 5.5 (c), (d) are the same as (a), (b) but the momentum scale of the previous data was decreased by a factor of 0.1 %. The $\Delta(\chi^2)$ for each scale factor is 16.0, 16.5, which corresponds to the statistical significance of 3.6, 3.7 σ, respectively. The peak position is 1519.0 $\pm$2.0 GeV/c^2, 1518.0 $\pm$, respectively. The RMM method is tried with several fitting ranges. The fitting range of 1.47-1.68 GeV/c^2 with decreasing the scale factor of the previous data gives the highest statistical

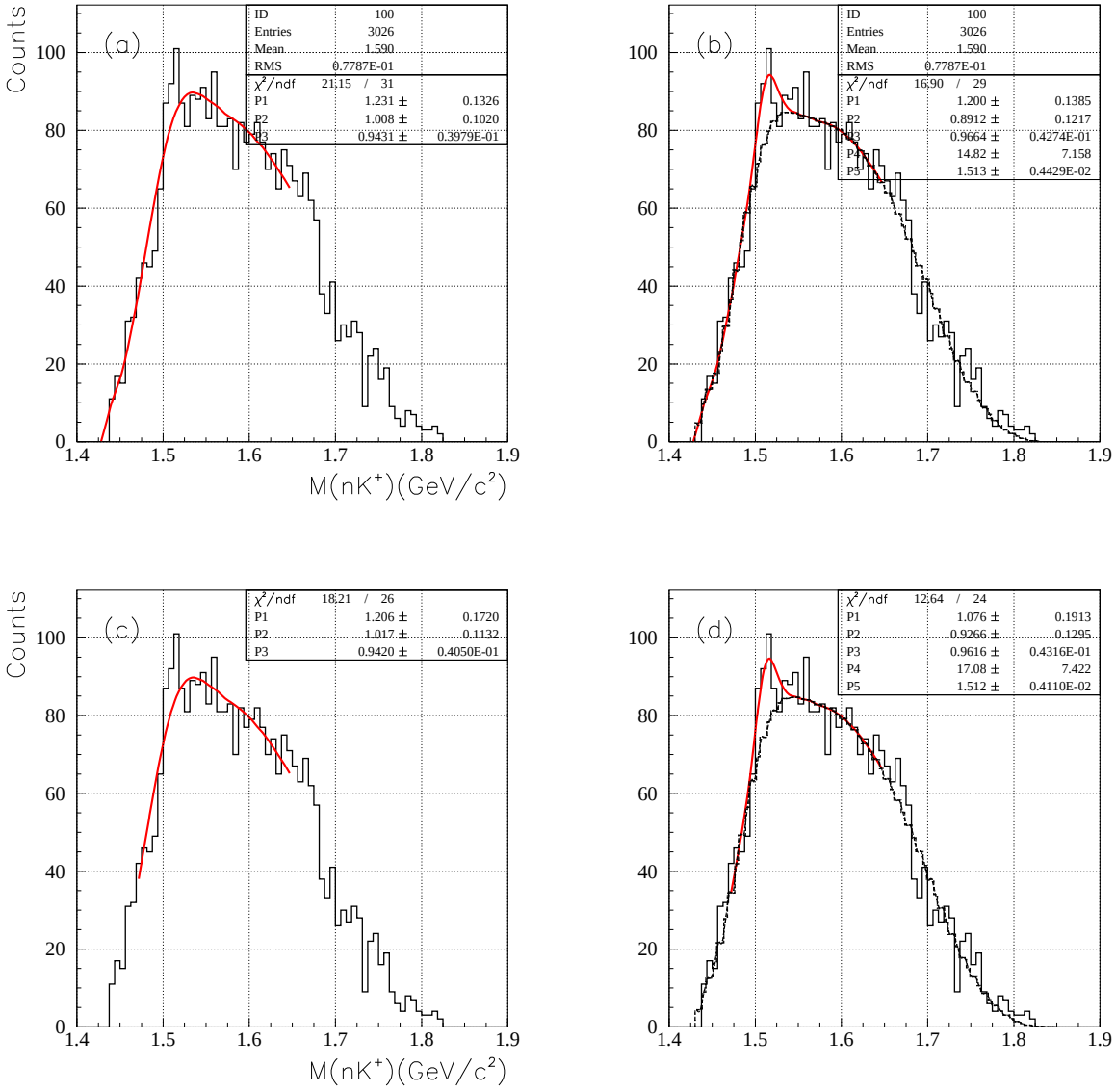

Figure 5.2: Fitting $M(nK^+)$ distribution by RMM method. Fitting range for (a),(b) is 1.43-1.65 GeV/c^2. Fitting range for (c),(d) is 1.47-1.65 GeV/c^2.

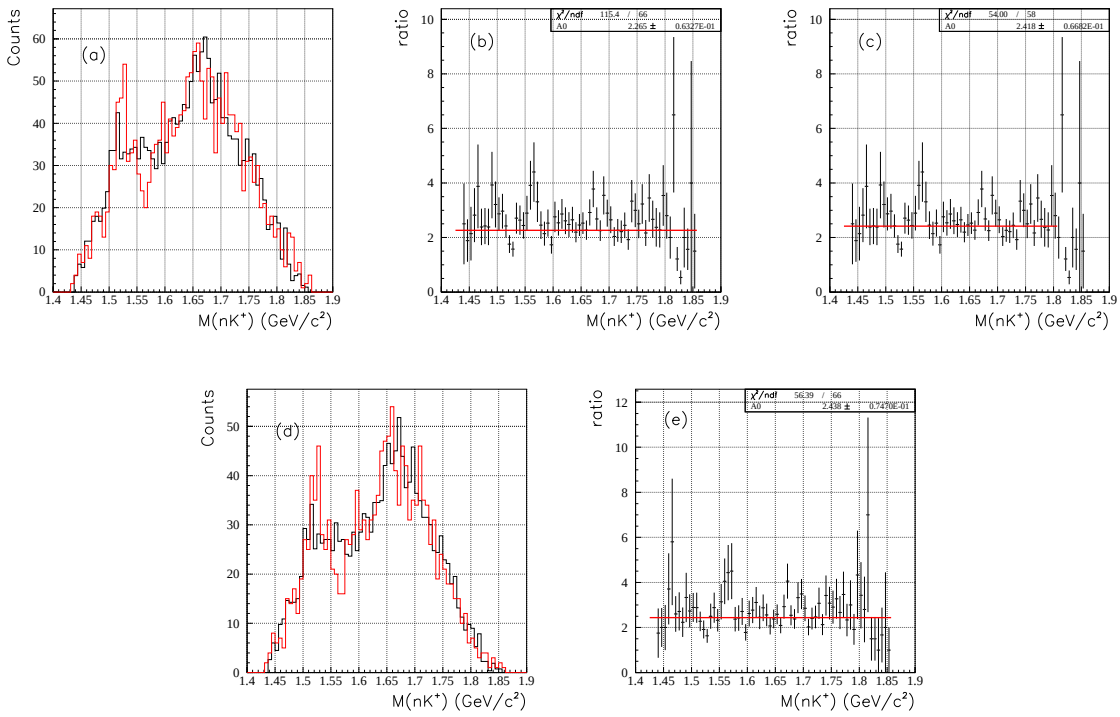

Figure 5.3: (a) $M(nK^+)$ distribution for two data sets. Black histogram is for the new data and red histogram is for the previous data. Two histograms are normalized by the entries. (b) Ratio of black and red histogram of (a). (c) The same as (b). Fitting region is restricted to below 1.8 GeV/c^2. (d) The same as (a) but photon energy cut of $2.0 \leq E_\gamma \leq 2.35$ is applied. (e) Ratio of black and red histogram of (d).

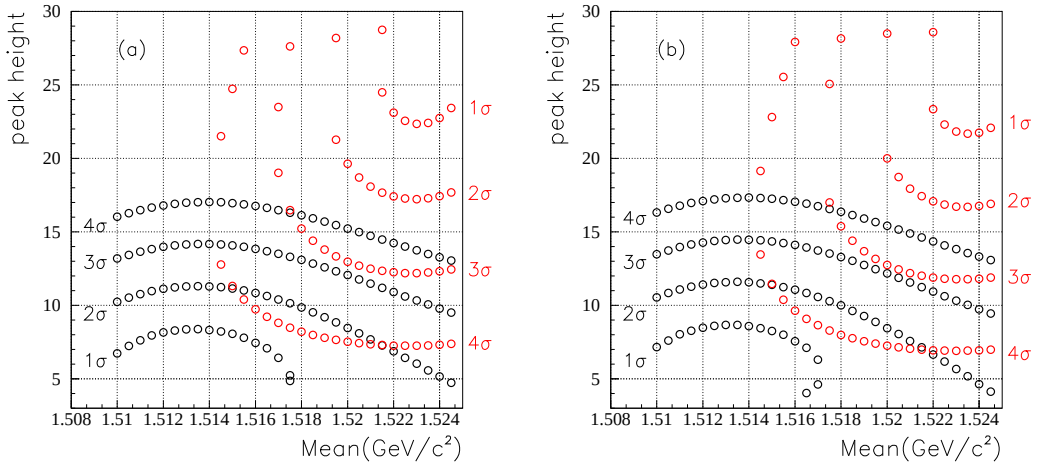

Figure 5.4: Contour of the χ^2 of fitting in the space of mean and peak height of the Gaussian. Black points are for the new data and red points are for the previous data. (a) RMM spectrum for each data set are used. (b) RMM spectrum for summed data are used for both data sets.

significance of 3.8 σ (Fig.5.6 (e), (f)).

5.4 Discussions

The final $M(nK^+)$ distribution for the new data does not show a strong narrow peak structure, which is inconsistent with the previous data. We performed further study to clarify the origin of the inconsistency. Then, it was found that further identification of the background process which comes from quasi-free production of KK from proton (KKp) events using pulse height information of the trigger counter (TRG) is possible. Figure 5.7 (a) shows the ADC spectrum of the TRG normalized by the MIP for summed data. We can see a peak around 2.5 which corresponds to the events which only K^+ and K^- fired the TRG. There is a large bump above around 4.5 which corresponds the the events which K^+ and K^- and proton fire the TRG. Because the TRG covers the largest solid angle among all the detectors, we can further identify KKp events by using pulse height information of TRG. By assuming that missing momentum of the K^+ and K^- is equal to the proton momentum, we can obtain the expected pulse height in the TRG when K^+ and K^- and proton fire the TRG. If the pulse height in the TRG is larger than the sum of the expected pulse height of K^+ and K^- and half of the expected pulse height of the proton, the event is identified as KKp event. Figure 5.7 (b) shows the pulse height in the TRG subtracted by the expected pulse height of KK and half of the expected pulse height of the proton. The separation is clear. The red histogram in Figure 5.7 (a) shows the events which are identified as KKp events. Figure 5.7 (c), (d) show the $M(pK^-)$ distribution of summed data for large (small) pulse height events. The S/N ratio of the $\Lambda(1520)$ peak is clearly better for large pulse height events. This is because the quasi-free KK production from neutron (KKn) events are almost completely rejected by selecting large ADC events. Note that even when we select small ADC events, the KKp events can not be completely rejected because of the limited acceptance of the TRG. This will be discussed later.

Figure 5.8 (a), (b) show the $M(nK^+)$ distribution of the previous data for large (small) ADC events. Figure 5.8 (c), (d) show the $M(nK^+)$ distribution of the new data for large (small) ADC events. There seems a small peak structure at the signal region when large ADC events are selected for the previous data while no peak structure is seen for the new data. Consequently, the strength of the signal for small ADC events dropped when compared with the spectrum with no ADC cut for the previous data. Because the KKp events can not make a peak in $M(nK^+)$ spectrum, it suggests that part of the origin of the peak structure in the previous data is due to the statistical fluctuation. Furthermore, there seems a enhancement at the signal region when small ADC events are selected for the new data.

To study this enhancement further, the $M(nK^+)$ distribution for summed data with small ADC events are checked. Figure 5.9 (a) (b) show the $M(nK^+)$ distribution for small ADC events for summed data with/without $\Lambda(1520)$ cut. The acceptance of the TRG for proton become smaller as the z-vertex position becomes upstream. Figure 5.10 (a) shows the z-vertex distribution for LH2 data. Figure 5.10 (b) shows the acceptance of the TRG for the proton as a function of the cut position of the z-vertex (z-vertex position is required to be larger than the cut point). The acceptance for the proton to fire the TRG exceed 90 % at the z-vertex position of -960 mm. A drop of the acceptance at -920 mm is due to the contamination of the capton sheet in the target chamber. Figure 5.10 (c) shows the ADC spectrum of TRG

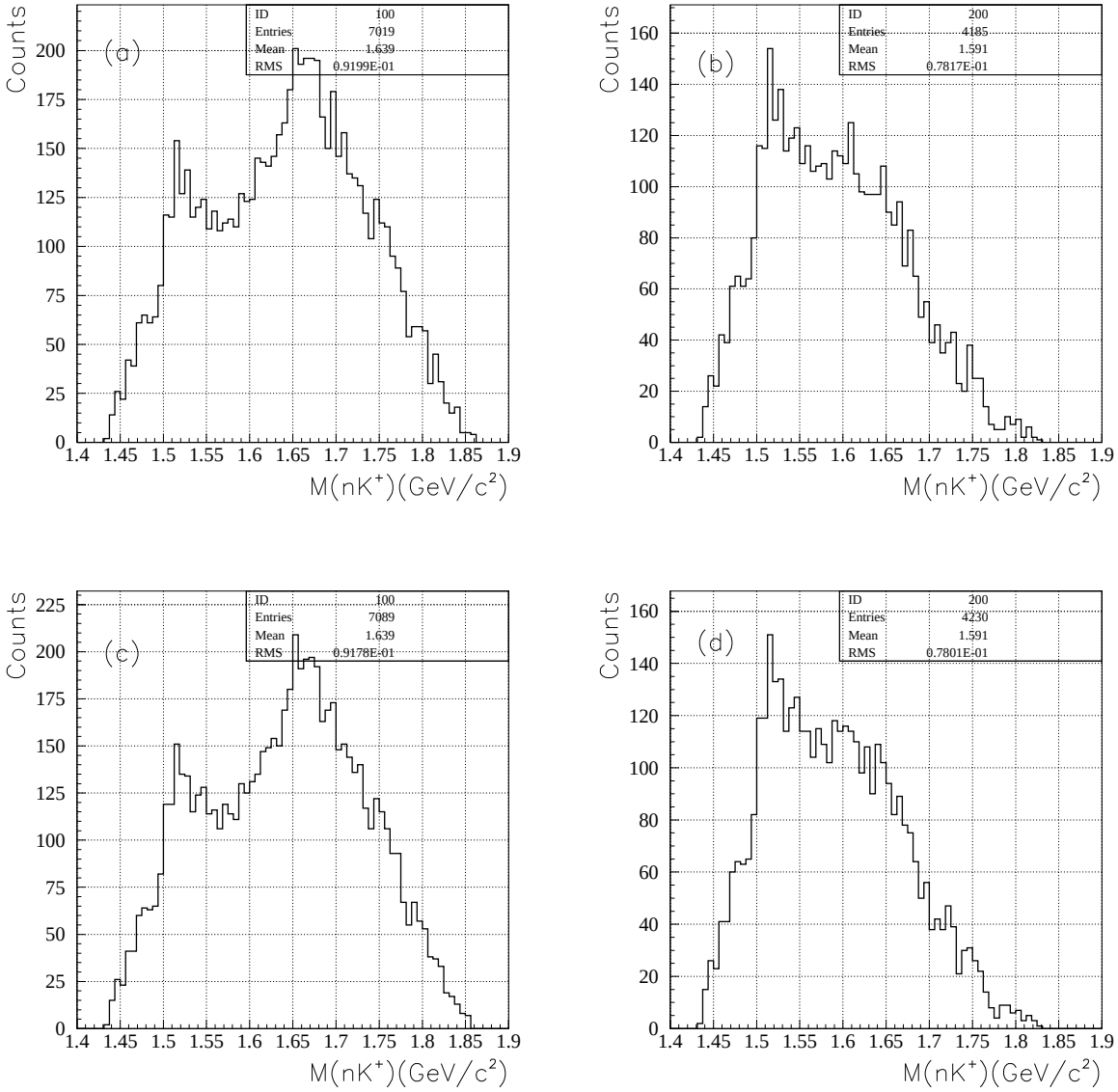

Figure 5.5: $M(nK^+)$ distribution for summed data after all the selection cut are applied. (a) Without $\Lambda(1520)$ cut. The momentum scale of the new data was increased by a factor of 0.1 %. (b) With $\Lambda(1520)$ cut. The momentum scale of the new data was increased by a factor of 0.1 %. (c) Without $\Lambda(1520)$ cut. The momentum scale of the previous data was decreased by a factor of 0.1 %. (d) With $\Lambda(1520)$ cut. The momentum scale of the previous data was decreased by a factor of 0.1 %.

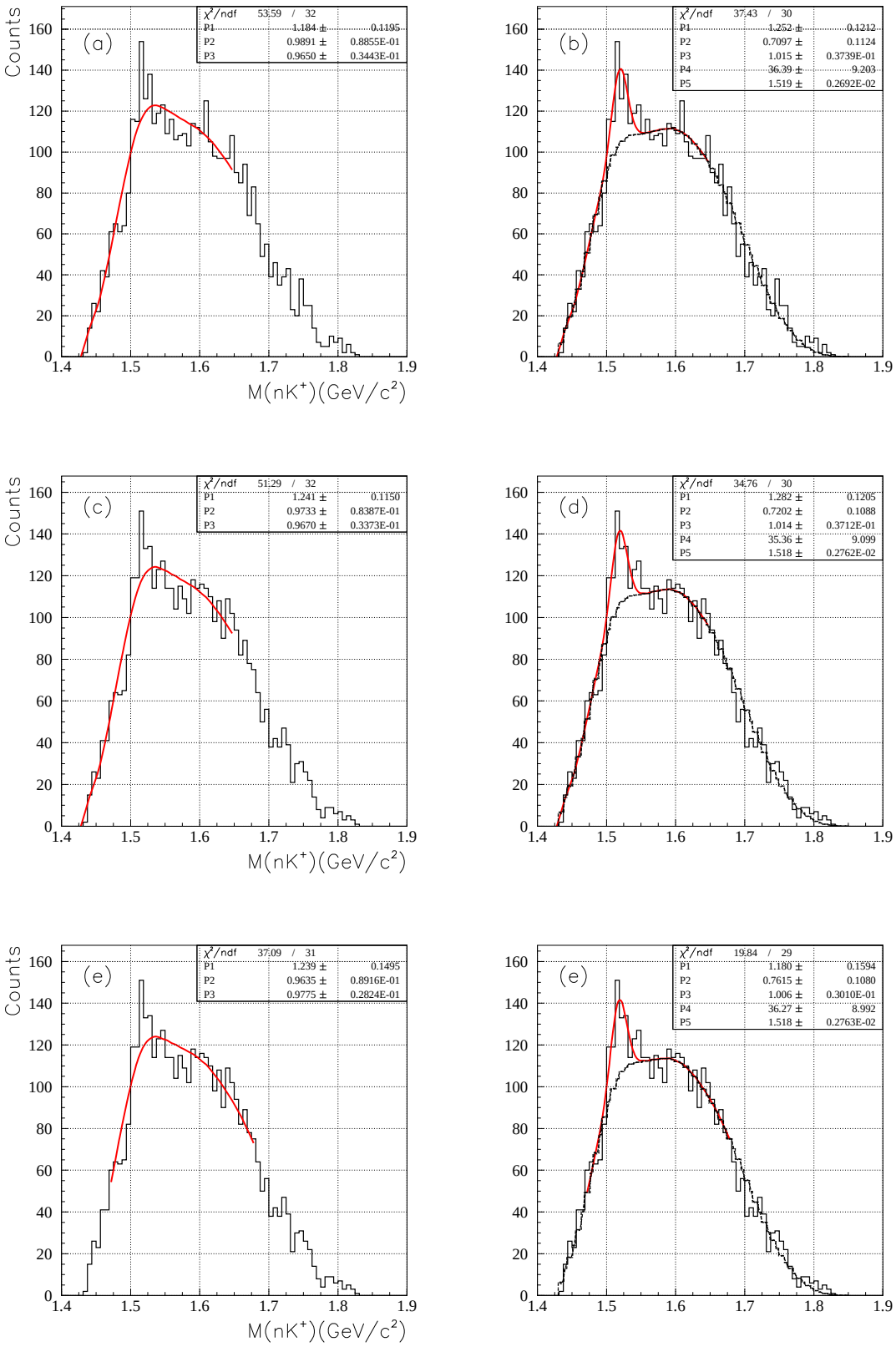

Figure 5.6: Fitting $M(nK^+)$ distribution for summed data by RMM method. (a),(b) The momentum scale of the new data was increased by a factor of 0.1 %. The fitting range is 1.43-1.65 GeV/c^2. (c),(d) The momentum scale of the previous data was decreased by a factor of 0.1 %. The fitting range is 1.43-1.65 GeV/c^2. (e),(f) The momentum scale of the previous data was decreased by a factor of 0.1 %. The fitting range is 1.47-1.68 GeV/c^2.

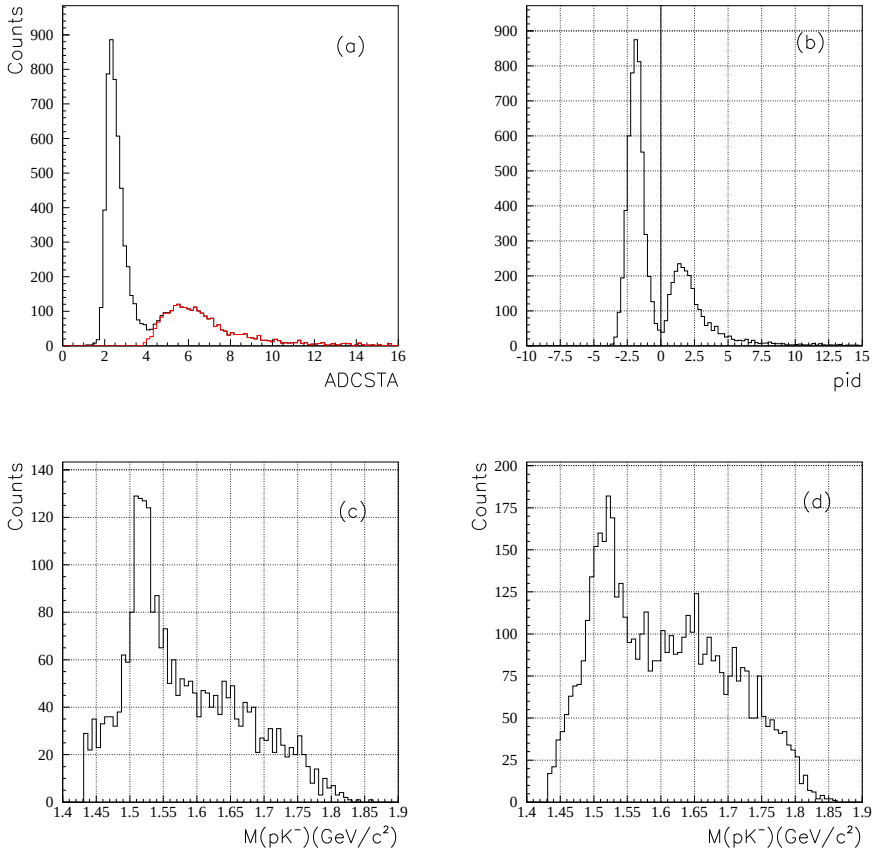

Figure 5.7: (a) ADC spectrum of TRG normalized by MIP value for summed data. (b) Pulse height in the TRG subtracted by the expected pulse height of KK and half of the expected pulse height of the proton. (c) $M(pK^-)$ distribution for large ADC events. (d) $M(pK^-)$ distribution for small ADC events.

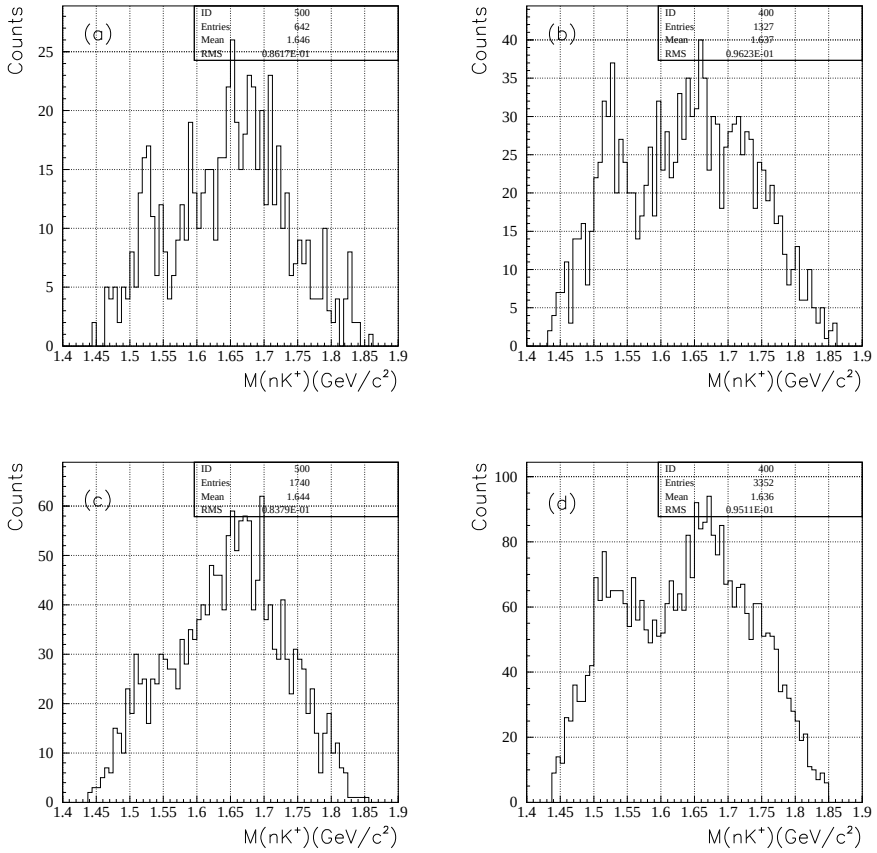

Figure 5.8: $M(nK^+)$ distribution. (a) For large ADC events for the previous data. (b) For small ADC events for the previous data. (c) For large ADC events for the new data. (d) For small ADC events for the new data.

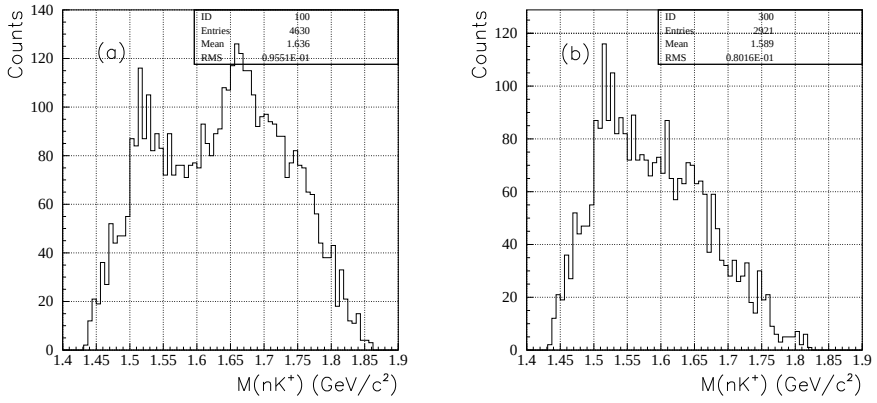

Figure 5.9: $M(nK^+)$ distribution for small ADC events for summed data. (a) Without $\Lambda(1520)$ cut. (b) With $\Lambda(1520)$ cut.

with a cut condition of z-vertex $\leq$ -960 mm. The number of events which KKp fired the TRG is small. Figure 5.10 (d) shows the ADC spectrum of TRG with a cut condition of z-vertex $\geq$ -960 mm. To reject the KKp events efficiently, a further cut condition of z-vertex $\geq$ -960 mm is applied. Figure 5.11 (a), (b) show the $M(nK^+)$ distribution for the previous data for small ADC events with an additional z-vertex cut. Because the statistics becomes low when we apply the z-vertex cut, the histogram with half binning (12.5 MeV/bin) is also shown. Figure 5.11 (c), (d) show the $M(nK^+)$ distribution for the new data and Fig. 5.11 (e), (f) show the $M(nK^+)$ distribution for the summed data. The enhancement remains and S/N ratio becomes better, which means that the enhancement surely comes from KKn events.

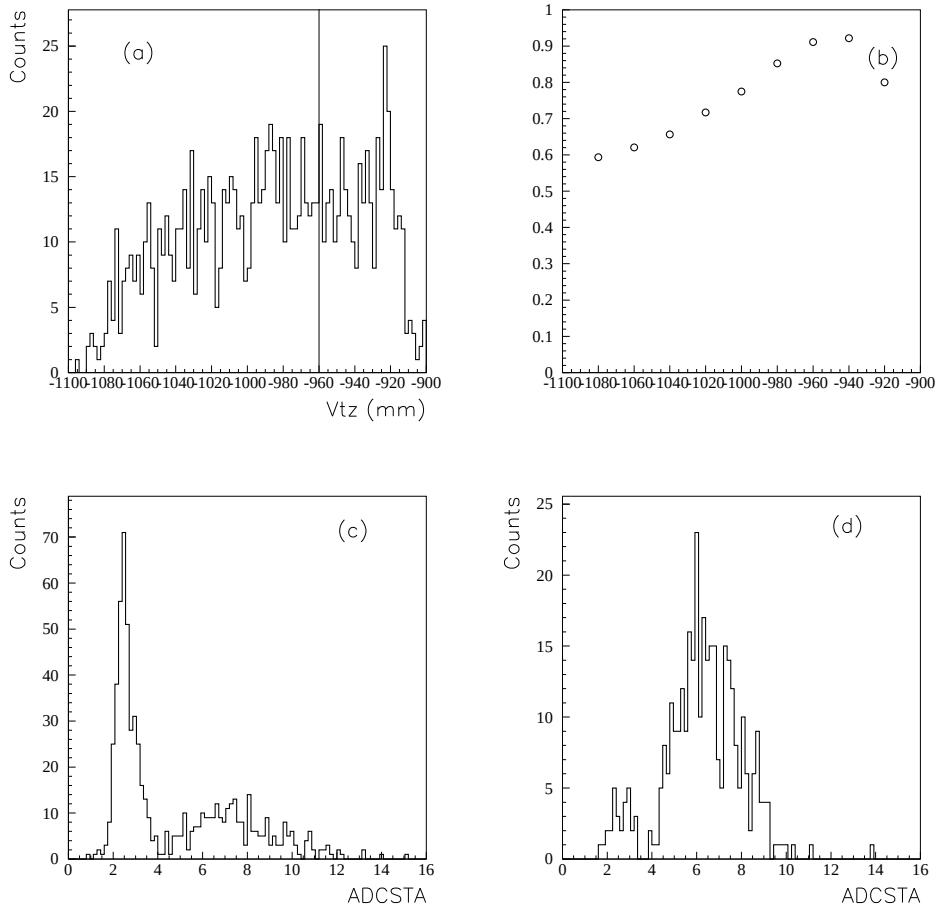

Figure 5.10: (a) z-vertex distribution for LH2 data. Vertical line (-960 mm) shows the cut point. (b) The acceptance of the TRG for the proton as a function of the z-vertex. (c) ADC spectrum of TRG for LH2 data with a cut condition of the z-vertex $\leq$ -960 mm. (d) ADC spectrum of TRG for LH2 data with a cut condition of the z-vertex $\geq$ -960 mm.

It is also interesting to see the polarization of the photon beam dependence of the $M(nK^+)$ distribution. Figure 5.12 (a), (b) show the $M(nK^+)$ distribution for data with vertically photon beam and (c), (d) show the one for the data with horizontally polarized photon beam.

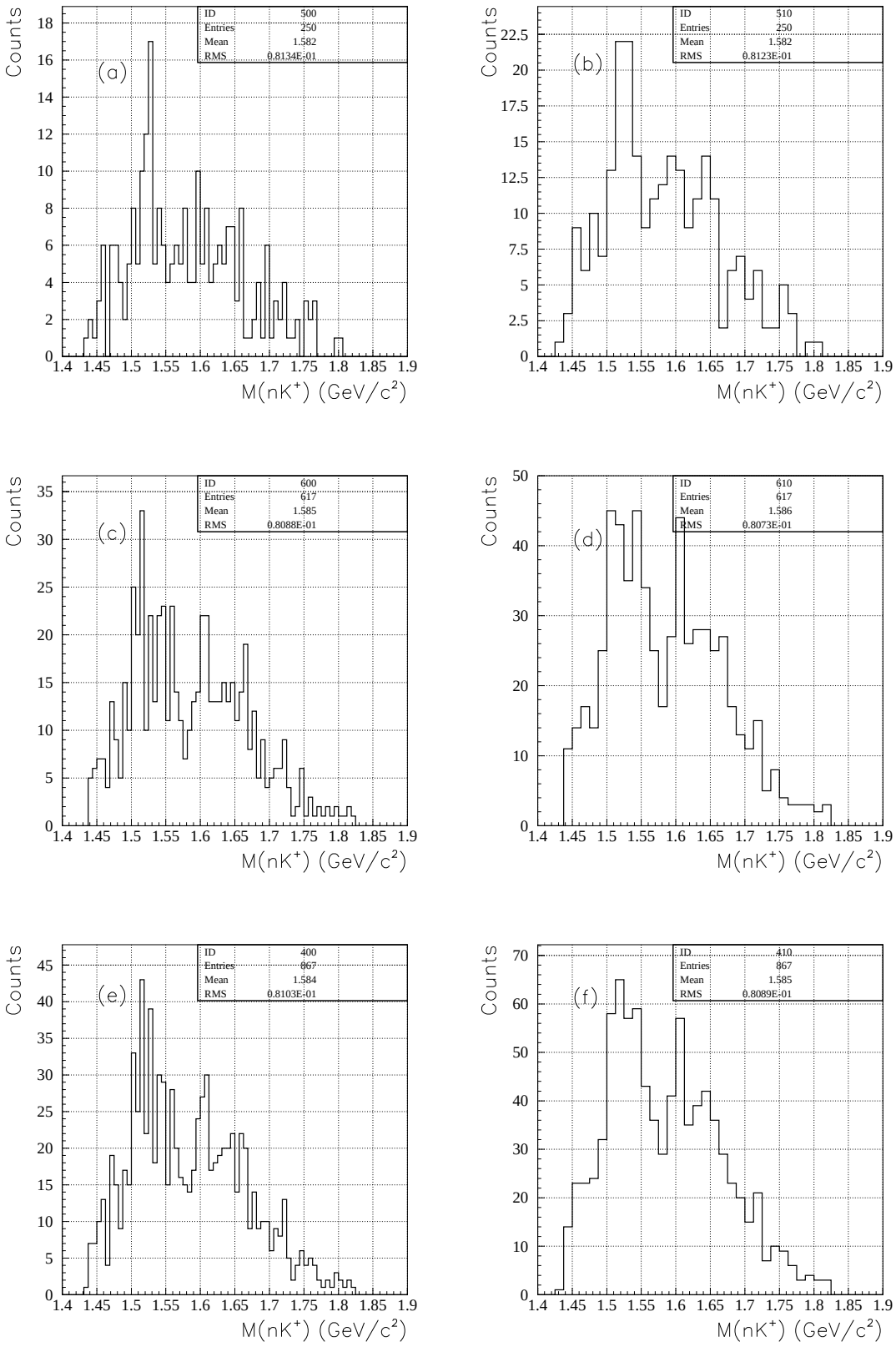

Figure 5.11: $M(nK^+)$ distribution for small ADC events with a further cut condition of z-vertex $\geq$ -960 mm and $\Lambda(1520)$ cut. (a) For the previous data. (b) For the previous data with half binning (12.5 MeV/bin). (c) For the new data. (d) For the new data with half binning (12.5 MeV/bin). (e) For the summed data. (f) For the summed data with half binning (12.5 MeV/bin).

The enhancement is larger for data with vertically polarized photon beam than data with horizontally polarized photon beam. Actually, not the signal region but the background shape has large polarization dependence.

The analysis using pulse height information of the TRG is in progress in the LEPS collaboration. The LEPS collaboration also plans to take new high statistics data with larger trigger counter to reject KKp events effectively.

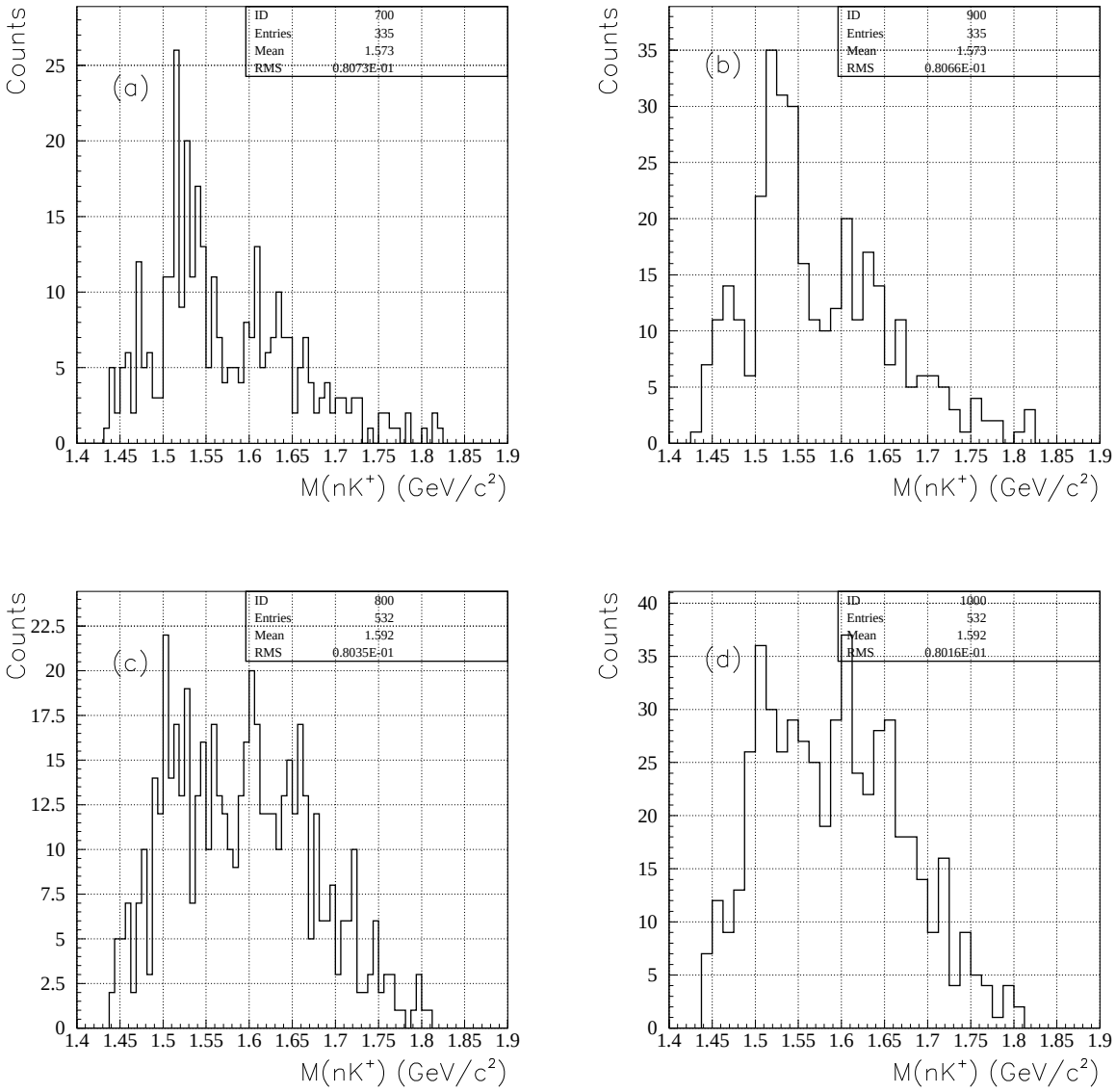

Figure 5.12: $M(nK^+)$ distribution for small ADC events with a further cut condition of z-vertex $\geq$ -960 mm. (a) Data with vertically polarized photons. (b) Data with vertically polarized photons (half binning). (c) Data with horizontally polarized photons. (d) Data with horizontally polarized photons (half binning).

Chapter 6

Summary

The pentaquark state, Θ^+ was searched via $\gamma d \to K^+K^-$ with high statistics data at SPring-8/LEPS facility. Since the LEPS collaboration reported the first evidence in 2003 [1], the studies for the Θ^+ has been widely performed from both experimentally and theoretically. Because of its low mass and narrow width which are difficult to be explained by conventional hadron models, Θ^+ is expected to bring us a new knowledge about the hadron physics. The most important task for the experimentalist now is to confirm whether Θ^+ really exists or not. There are a number of positive and negative evidences of the Θ^+ and situation is still controversial. The LEPS collaboration reported a further evidence in $\gamma d \to K^+K^-$ from the LD2 target data taken in 2002-2003 [48]. To confirm the result further, the LEPS collaboration took about 2.6 times higher statistics data with almost the same setup as the previous data. For the data taking, a two laser injection system was developed to increase the beam intensity. It successfully worked and achieved a tagger rate of 2.0 Mcps at the maximum.

In the analysis of the new data, the blind analysis is applied to remove the human bias. The cut conditions are fixed from the previous data and calibration is tuned without checking signal samples. Because there is no good 'anchor' reaction for the calibration of negative charged particles, several new calibration methods are developed. The corrections for timing and xt-curve of the DCs are implemented. As a result, a good position resolution of 140 μm was achieved. The alignment including rotation of the DCs and SVTX are performed with no magnetic field run. The way to solve left-right ambiguity of the DCs are modified to reduce the misidentification. The photon energy and global momentum scale was determined with checking several reactions simultaneously. The peak position of the missing mass is within 1 MeV/c^2 for all the reactions. The value is much smaller than the typical missing mass resolution of about 10 MeV/c^2.

Before opening the box, the comparison of ϕ photo-production events and $\Lambda(1520)$ photo-production between two data sets are performed with masking the signal region. The spectrum of important variables such as p_{min} and $M(pK^-)$ are found to be consistent for the two data sets by changing the global momentum scale by a factor 0.1 %. Because no essential difference are found, we decided to sum two data sets after opening the box.

The $M(nK^+)$ distribution for the new data did not show a strong narrow peak structure. The fitting by RMM method gives a statistical significance of 1.6-1.9 σ depending on the fitting range. The peak position is 1513 ± 5 MeV/c^2, which is lower than the result of the previous data (1524 ± 2 MeV/c^2). The χ^2 test of $M(nK^+)$ distribution for two data sets gives

a 54.0/58, which is reasonably good, suggesting that the acceptance for the two data sets are essentially the same within the statistics. To check the consistency between the two data sets in the signal region, the χ^2 of the fitting in the space of mean and height of the Gaussian is investigated. At the closest point, the χ^2 of the fittings are deviated almost 3 σ from both of data sets. Previous result is not reproduced.

Summed data show a statistical significance of 3.6-3.8 σ with a peak position of 1518, 1519 ± 2.0 MeV/c^2 depending on the tuning of the momentum scale factor and fitting range.

The origin of the inconsistency for two data sets are investigated. It was found that further identification of the background process comes from quasi-free production of KK from proton (KKp) events using pulse height information of the trigger counter (TRG) is possible. For the previous data, the peak structure is seen even when we select the KKp events while no structure is seen in the new data. Because the KKp events can not make a narrow peak in the $M(nK^+)$ spectrum and actually it is not seen in the new data, part of the peak structure seen in the previous data come from the statistical fluctuation.

Furthermore, after rejecting the KKp events, an enhancement at the signal region is seen for the new data and summed data. After applying further cut for the z-vertex point to enlarge the acceptance of the TRG, the enhancement remains and the S/N ratio becomes better, which shows that the enhancement surely comes from KKn events. The enhancement is larger for data with vertically polarized photon beam than the data with horizontally polarized photon beam. The analysis using pulse height information of the TRG is in progress by the LEPS collaboration. The LEPS collaboration also plans to take the new data with large trigger counter to reject KKp events effectively.

Appendix A

The Alignment parameters of DCs and SVTX

The rotation parameters of DCs in z-axis are summarized in table A.1.

The shift parameters of SVTX are summarized in table A.2. The rotation parameters of SVTX are summarized in table A.3. Note that module 9-12 are for measurement of the position of y-direction.

plane	$\sigma_z(radian)$
DC1X1	-0.000363
DC1X2	-0.000408
DC1U1	-0.000230
DC1U2	-0.000273
DC1V	-0.000339
DC1X3	-0.000401
DC2X1	0.000252
DC2X2	0.000255
DC2U1	0.000059
DC2U2	0.000032
DC2V	0.000167
DC3X1	-0.000200
DC3X2	-0.000189
DC3U1	-0.000228
DC3U2	-0.000228
DC3V	-0.000213

Table A.1: Summary of rotation parameter of DCs.

module ID	x-direction(mm)	y-direction(mm)	z-direction(mm)
1	0.487	-	1.441
2	0.339	-	-0.145
3	-0.409	-	0.689
4	0.930	-	0.033
5	0.216	-	0.271
6	0.483	-	0.463
7	-0.558	-	-0.189
8	0.625	-	0.065
9	-	0.330	2.490
10	-	-0.108	-1.956
11	-	-0.461	-1.392
12	-	-1.267	2.322

Table A.2: Summary of shift parameter of SVTX

module ID	$\sigma_x(radian)$	$\sigma_y(radian)$	$\sigma_z(radian)$
1	0.00587	-0.00556	-0.00250
2	0.01453	0.00000	0.00336
3	-0.00474	0.00000	0.00181
4	0.01176	0.00000	0.00458
5	-0.00824	-0.00176	0.00897
6	0.00906	0.00000	-0.00250
7	-0.00586	0.00000	-0.00109
8	-0.00817	0.00000	0.00037
9	0.00000	-0.01288	0.00216
10	0.00000	0.02415	0.00335
11	0.00000	-0.02763	0.00424
12	0.00000	0.01293	0.00358

Table A.3: Summary of rotation parameters of SVTX

Appendix B

Various comparisons between new and previous data using LD2 data.

B.1 Analysis of the K^+ K^- p detection mode

By using the additional information on detected proton, we can directly calculate the invariant mass $M(pK^+)$ and $M(pK^-)$. By taking the difference of Fermi-motion corrected invariant mass and directly calculated invariant mass event by event, we can check the Fermi-motion corrected invariant mass resolution. Figure B.1 shows the difference of $M(pK^-)$ for each data. Figure B.2 shows the difference of $M(pK^+)$ for each data. The fitting function is single Gaussian. The cut condition $|p_{min}| < 0.1\ GeV/c$ is applied to reject events large Fermi-momentum.

Furthermore, the peak of the neutron in missing mass of the K^+ K^- p assuming that the target is a deuteron at rest ($MMd(\gamma, K^+K^-p)n$) is a good probe to check the calibration because the Fermi-motion correction is not necessary. Figure B.3 shows the $MMd(\gamma, K^+K^-p)X$ distribution for each data set. The analysis of K^+ K^- p detection mode is summarized in table B.1. The mean of the difference of the $M(pK^+)$ and the $M(pK^-)$ is consistent for two data sets. The σ of the $M(pK^+)$ and the $M(pK^-)$ is better for new data. The peak position of the $MMd(\gamma, K^+K^-p)n$ is inconsistent for two data sets but that for new data is more close to the PDG value of the mass of the neutron than that of previous data. The σ of the $MMd(\gamma, K^+K^-p)n$ is better for new data.

	2002-2003	2006-2007
Mean of pK^-	1.7±0.6	2.0±0.3
σ of pK^-	10.3±0.6	9.3±0.3
Mean of pK^+	1.0±0.6	1.7±0.3
σ of pK^+	10.5±0.7	9.5±0.3
Mean of $MMd(\gamma, K^+K^-p)n$	937.5±0.8	939.7±0.2
σ of $MMd(\gamma, K^+K^-p)n$	16.2±0.7	13.7±0.3

Table B.1: Summary of the analysis of K^+ K^- p detection mode. All the units are MeV/c^2.

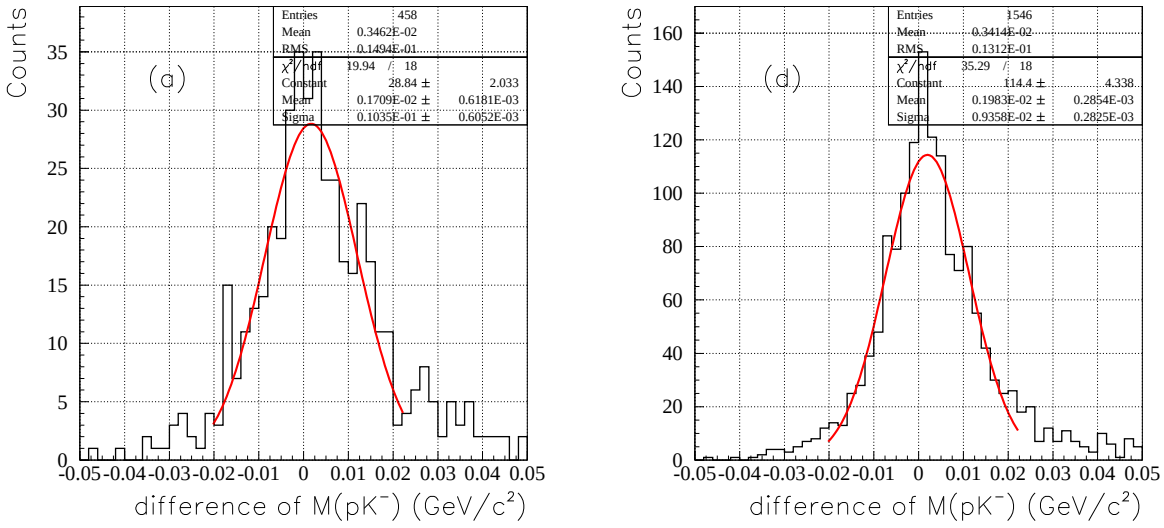

Figure B.1: The difference of $M(pK^-)$. (a) Previous data.(b) New data.

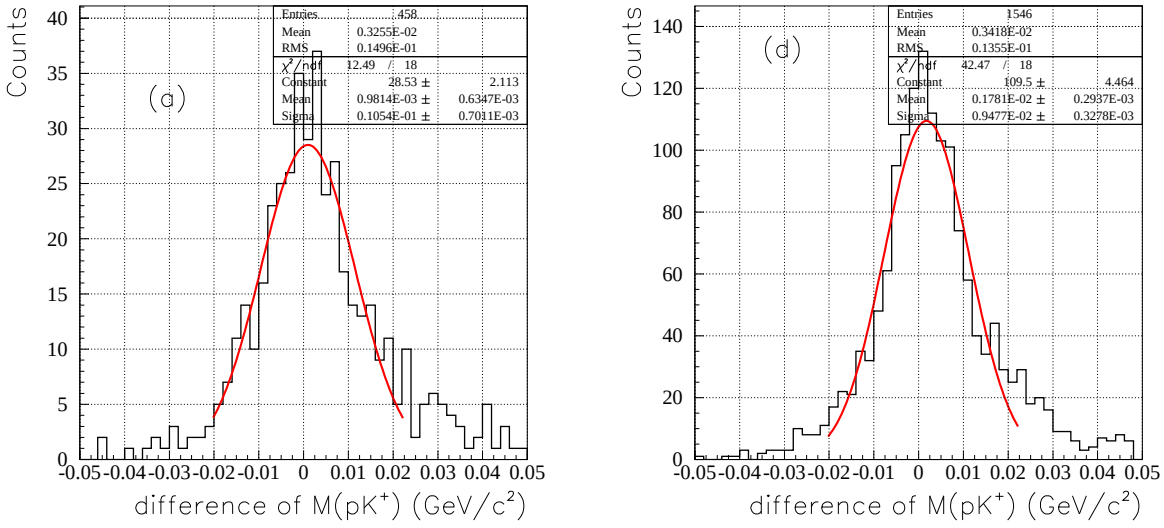

Figure B.2: The difference of $M(pK^+)$. (a) Previous data (b) New data.

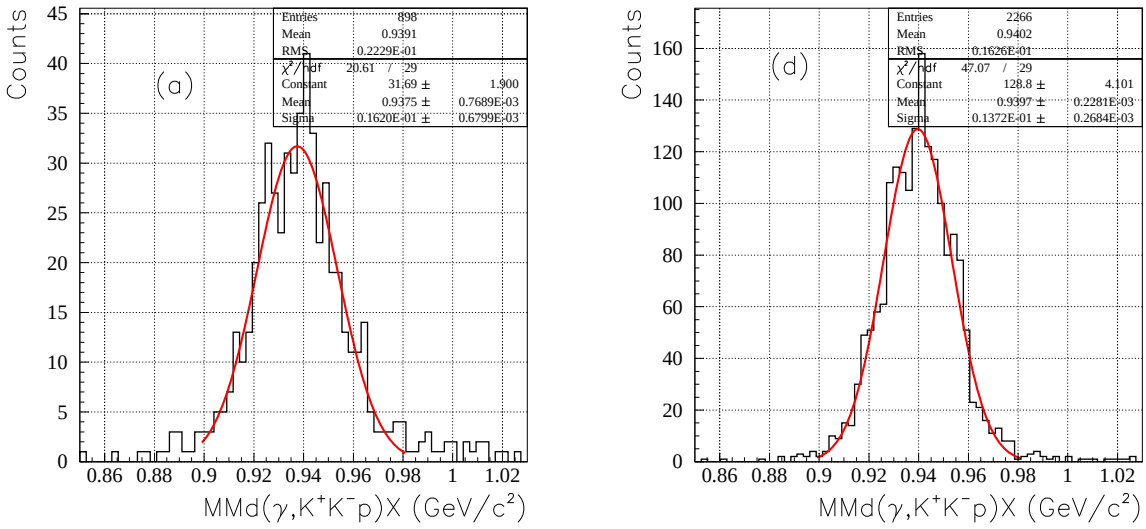

Figure B.3: $MMd(\gamma, K^+K^-p)X$. (a) Previous data. (b) New data.

B.2 $\gamma n \to K^+\Sigma^- \to K^+\pi^- n$ reaction

The $\gamma n \to K^+\Sigma^- \to K^+\pi^- n$ reaction has a similar event topology to the $\gamma p \to K^+\Lambda(1520) \to K^+K^-p$ reaction. By interchanging the K^- and π^-, the MMSA for the $M(K^-p)$ can be applied for $M(\pi^-n)$. This reaction has three advantages for the check of the calibration comparing with $\Lambda(1520)$ production.

- The statistics is higher than $\Lambda(1520)$ production.
- The background level is lower than $\Lambda(1520)$ production.
- The natural width of the Σ^- is very narrow because it decays via the weak interaction. Therefore, the mass resolution directly reflects the quality of the calibration.

Figure B.4 shows the scatter plot of the $MMn(\gamma, K^+\pi^-)X$ and the $MMn(\gamma, K^+)X$. The red points show the selection of $\gamma n \to K^+\Sigma^-$ events. Figure B.5 shows the $M(\pi^-n)$ for each data set. The mean and the σ of each histogram are summarized in table B.2. The resolution is better for new data than that of previous data. The peak position is statistically consistent.

	2002-2003	2006-2007
Mean (MeV/c^2)	1198.8±0.4	1198.4±0.2
σ (MeV/c^2)	12.3±0.4	11.1±0.2

Table B.2: Summary of $\gamma n \to K^+\Sigma^-$ reaction.

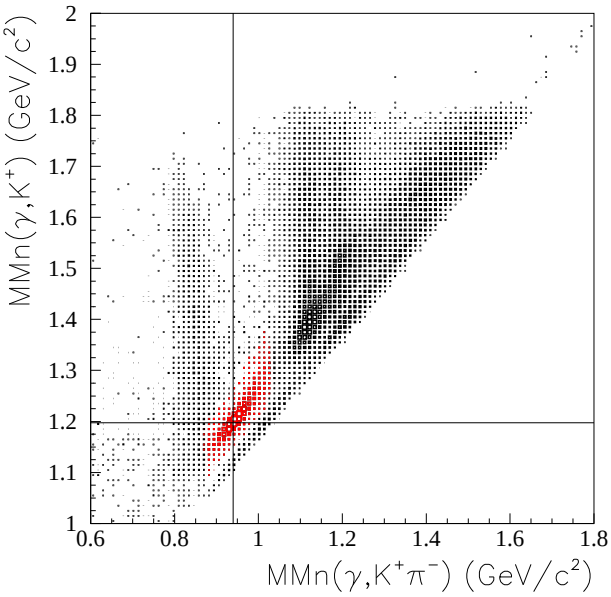

Figure B.4: Scatter plot of the $MMn(\gamma, K^+\pi^-)X$ and the $MMn(\gamma, K^+)X$. Vertical (horizontal) line shows the mass of the neutron (Σ^-). Red points show the selected $\gamma n \to K^+\Sigma^-$ events.

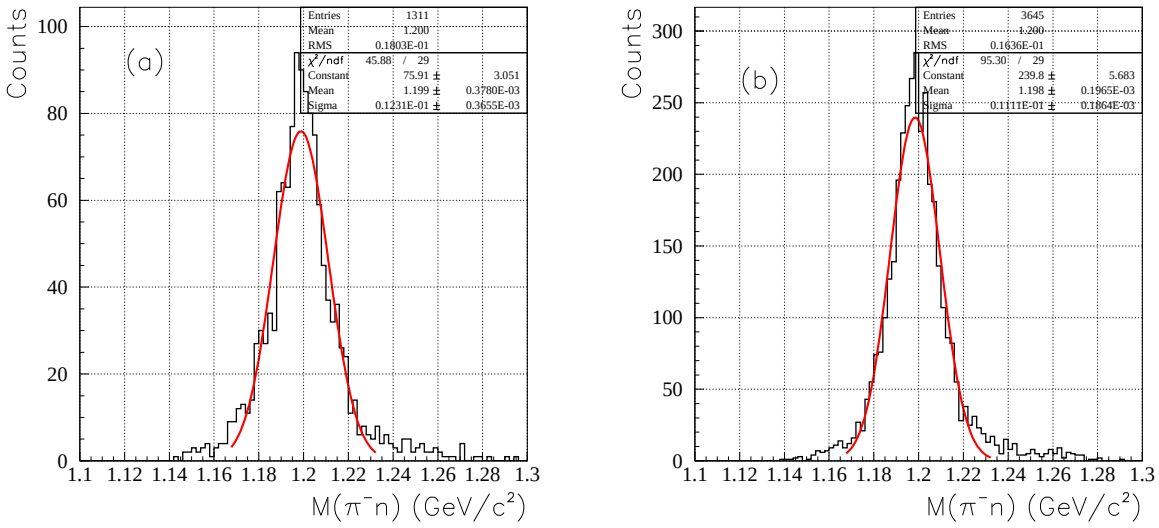

Figure B.5: $M(\pi^- n)$. Fitting function is single Gaussian. E_γ is required to be greater than 2.0 GeV. (a) Previous data. (b) New data.

B.3 $\gamma d \to pn$ reaction

The $\gamma d \to pn$ reaction is a good prove to check the momentum resolution of LD2 data for two reasons. One is that the Fermi-motion correction is not necessary. The other is that the proton momentum is very high (averaged momentum of the proton is 2.3 GeV/c). Figure B.6 shows the $MMd(\gamma, p)X$ for each data set. The neutron peak is clearly sharper for new data than that of previous data.

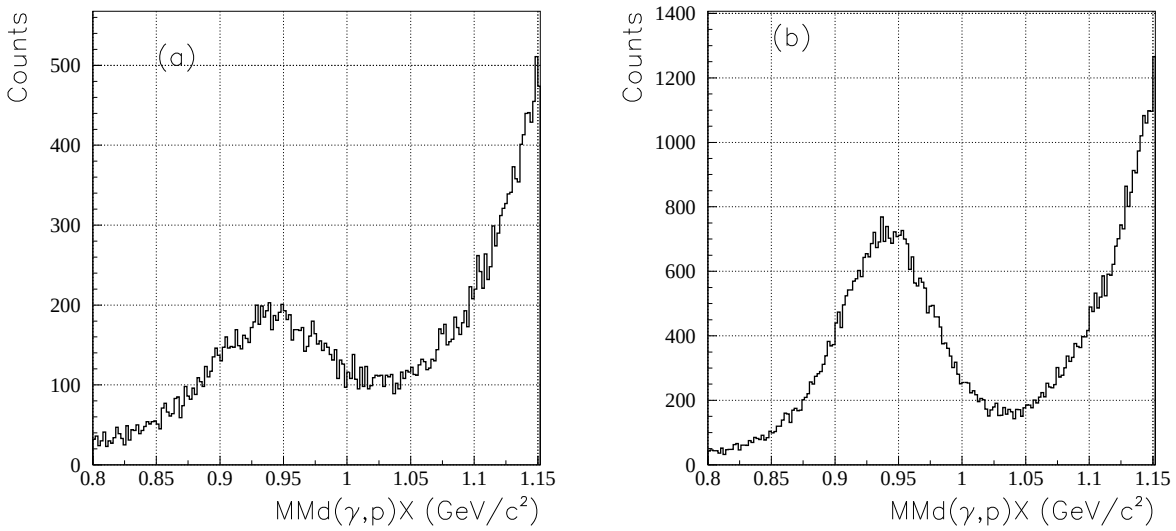

Figure B.6: $MMd(\gamma, p)X$. (a) Previous data.(b) New data.

Bibliography

[1] T. Nakano *et al.* [LEPS Collaboration], Phys. Rev. Lett. **91**, 012002 (2003) [arXiv:hep-ex/0301020].

[2] D. Diakonov, V. Petrov and M. V. Polyakov, Z. Phys. A **359**, 305 (1997) [arXiv:hep-ph/9703373].

[3] F. Huang, Z. Y. Zhang, Y. W. Yu and B. S. Zou, Phys. Lett. B **586**, 69 (2004) [arXiv:hep-ph/0310040].

[4] D. Diakonov, JETP Lett. **90**, 407 (2009) [arXiv:0812.3418 [hep-ph]].

[5] R. L. Jaffe and F. Wilczek, Phys. Rev. Lett. **91**, 232003 (2003) [hep-ph/0307341].

[6] T. Kishimoto and T. Sato, Prog. Theor. Phys. **116**, 241 (2006) [hep-ex/0312003].

[7] T. Hyodo, D. Jido and A. Hosaka, Phys. Rev. D **75**, 034002 (2007) [hep-ph/0611004].

[8] N. Kaiser, P. B. Siegel and W. Weise, Nucl. Phys. A **594**, 325 (1995) [arXiv:nucl-th/9505043].

[9] M. Danilov and R. Mizuk, arXiv:0704.3531 [hep-ex].

[10] V. V. Barmin *et al.* [DIANA Collaboration], Phys. Atom. Nucl. **66**, 1715 (2003) [Yad. Fiz. **66**, 1763 (2003)] [hep-ex/0304040].

[11] V. V. Barmin *et al.* [DIANA Collaboration], Phys. Atom. Nucl. **70** (2007) 35 [hep-ex/0603017].

[12] R. N. Cahn and G. H. Trilling, Phys. Rev. D **69**, 011501 (2004) [hep-ph/0311245].

[13] C. J. S. Damerell *et al.*, Nucl. Phys. B **94** (1975) 374.

[14] V. V. Barmin *et al.* [DIANA Collaboration], Phys. Atom. Nucl. **73** (2010) 1168 [arXiv:0909.4183 [hep-ex]].

[15] K. Abe *et al.* [Belle Collaboration], Phys. Lett. B **632**, 173 (2006) [hep-ex/0507014].

[16] A. E. Asratyan, A. G. Dolgolenko and M. A. Kubantsev, Phys. Atom. Nucl. **67**, 682 (2004) [Yad. Fiz. **67**, 704 (2004)] [arXiv:hep-ex/0309042].

[17] A. Airapetian *et al.* [HERMES Collaboration], Phys. Lett. B **585**, 213 (2004) [hep-ex/0312044].

[18] S. Chekanov *et al.* [ZEUS Collaboration], Phys. Lett. B **591**, 7 (2004) [hep-ex/0403051].

[19] P. Z. .Aslanyan, V. N. Emelyanenko and G. G. Rikhkvitzkaya, Nucl. Phys. A **755**, 375 (2005) [hep-ex/0403044].

[20] Y. .A. Troyan, A. V. Beljaev, A. Y. .Troyan, E. B. Plekhanov, A. P. Jerusalimov, G. B. Piskaleva and S. G. Arakelian, hep-ex/0404003.

[21] A. Aleev *et al.* [SVD Collaboration], Phys. Atom. Nucl. **68**, 974 (2005) [Yad. Fiz. **68**, 1012 (2005)] [hep-ex/0401024].

[22] A. Aleev *et al.* [SVD Collaboration], hep-ex/0509033.

[23] J. Z. Bai *et al.* [BES Collaboration], Phys. Rev. D **70** (2004) 012004 [arXiv:hep-ex/0402012].

[24] B. Aubert *et al.* [BABAR Collaboration], hep-ex/0408064.

[25] K. Abe *et al.* [BELLE Collaboration], hep-ex/0409010.

[26] I. Abt *et al.* [HERA-B Collaboration], Phys. Rev. Lett. **93**, 212003 (2004) [hep-ex/0408048].

[27] Yu. M. Antipov *et al.* [SPHINX Collaboration], Eur. Phys. J. A **21** (2004) 455 [arXiv:hep-ex/0407026].

[28] M. J. Longo *et al.* [HyperCP Collaboration], Phys. Rev. D **70**, 111101 (2004) [arXiv:hep-ex/0410027].

[29] I. V. Gorelov [CDF Collaboration], hep-ex/0408025.

[30] K. Stenson [FOCUS Collaboration], Int. J. Mod. Phys. A **20**, 3745 (2005) [hep-ex/0412021].

[31] C. Pinkenburg [PHENIX Collaboration], J. Phys. G **30**, S1201 (2004) [arXiv:nucl-ex/0404001].

[32] S. R. Armstrong, Nucl. Phys. Proc. Suppl. **142**, 364 (2005) [hep-ex/0410080].

[33] M. Zavertyaev [WA89 and COMPASS Collaboration], Nucl. Phys. A **755** (2005) 387.

[34] S. R. Armstrong, Nucl. Phys. Proc. Suppl. **142**, 364 (2005) [hep-ex/0410080].

[35] M. A. Reyes et al proceedings of HADRON SPECTROSCOPY Nucl. Phys. A **755** (2005) 387.

[36] J. Napolitano, J. Cummings and M. Witkowski, hep-ex/0412031.

[37] K. Miwa, S. Dairaku, D. Nakajima, S. Ajimura, J. Arvieux, H. Fujimura, H. Fujioka and T. Fukuda *et al.*, Phys. Rev. C **77**, 045203 (2008) [arXiv:0712.3839 [nucl-ex]].

[38] K. Miwa *et al.* [KEK-PS E522 Collaboration], Phys. Lett. B **635**, 72 (2006) [nucl-ex/0601032].

[39] M. Abdel-Bary *et al.* [COSY-TOF Collaboration], Phys. Lett. B **595** (2004) 127 [arXiv:hep-ex/0403011].

[40] M. Abdel-Bary, S. Abdel-Samad, K. -T. .Brinkmann, R. Castelijns, H. Clement, J. Dietrich, S. Dshemuchadse and E. Dorochkevitch *et al.*, Phys. Lett. B **649**, 252 (2007) [hep-ex/0612048].

[41] J. Barth *et al.* [SAPHIR Collaboration], Phys. Lett. B **572**, 127 (2003) [arXiv:hep-ex/0307083].

[42] S. Stepanyan *et al.* [CLAS Collaboration], Phys. Rev. Letbt. **91**, 252001 (2003) [hep-ex/0307018].

[43] V. Kubarovsky *et al.* [CLAS Collaboration], Phys. Rev. Lett. **92** (2004) 032001 [Erratum-ibid. **92** (2004) 049902] [arXiv:hep-ex/0311046].

[44] R. De Vita *et al.* [CLAS Collaboration], Phys. Rev. D **74**, 032001 (2006) [hep-ex/0606062].

[45] B. McKinnon *et al.* [CLAS Collaboration], Phys. Rev. Lett. **96**, 212001 (2006) [hep-ex/0603028].

[46] S. Niccolai *et al.* [CLAS Collaboration], Phys. Rev. Lett. **97**, 032001 (2006) [hep-ex/0604047].

[47] M. J. Amaryan, G. Gavalian, C. Nepali, M. V. Polyakov, Y. .Azimov, W. J. Briscoe, G. E. Dodge and C. E. Hyde *et al.*, arXiv:1110.3325 [hep-ex].

[48] T. Nakano *et al.* [LEPS Collaboration], Phys. Rev. C **79**, 025210 (2009) [arXiv:0812.1035 [nucl-ex]].

[49] M. Sumihama *et al.* [LEPS Collaboration], Phys. Rev. C **73**, 035214 (2006) [arXiv:hep-ex/0512053].

[50] B. A. Mecking *et al.* [CLAS Collaboration], Nucl. Instrum. Meth. A **503** (2003) 513.

[51] M. Amarian, D. Diakonov and M. V. Polyakov, Phys. Rev. D **78**, 074003 (2008) [hep-ph/0612150].

[52] S. -I. Nam, A. Hosaka and H. -C. Kim, Phys. Lett. B **633**, 483 (2006) [hep-ph/0505134].

[53] N. Muramatsu *et al.*, Phys. Rev. Lett. **103** (2009) 012001 [arXiv:0904.2034 [nucl-ex]].

[54] SPring-8 annual report (1998) 132.

[55] A. D'Angelo, O. Bartalini, V. Bellini, P. Levi Sandri, D. Moricciani, L. Nicoletti and A. Zucchiatti, Nucl. Instr. Meth. **A455** (2000) 1.

[56] O.Toker, S. Masciocchi, E. Nygard, A. Rudge and P. Weilhammer, Nucl. Instr. Meth. **A340** (1994) 572.

[57] M. Sumihama PhD thesis, Osaka University (2003).

[58] T. Ishikawa PhD thesis, Kyoto University (2005).

[59] H. Kohri et al., RCNP annual report (2002).

[60] H. Kohri LEPS Technical Note 15 (unpublished).

[61] M. Miyabe PhD thesis, Osaka University (2010).

[62] T. Ishikawa, T. Mibe, N. Muramatsu, T. Nakano, M.Sumihama, and R.G.T Zegers, LEPS Technical Note 1 (unpublished).

[63] Web: http://paw.web.cern.ch/paw/.

[64] Web: http://cernlib.web.cern.ch/cernlib/.

[65] Web: http://wwwasd.web.cern.ch/wwwasd/geant/index.html.

[66] W.C. Chang, LEPS Technical Note 2 (unpublished).

[67] Y. Kato LEPS Technical Note 44 (unpublished).

[68] Y. Kato LEPS Technical Note 34 (unpublished).

[69] M. Lacombe, B. Loiseau, J. M. Richard, R. Vinh Mau, J. Cote, P. Pires and R. De Tourreil, Phys. Rev. C **21**, 861 (1980).

[70] R. Suda, M. Watanabe, R. Enomoto, T. Iijima, I. Adachi, H. Hattori, T. Kuniya, T. Ooba, T. Sumiyoshi and Y. Yoshida, Nucl. Instr. Meth. **A406** (1998) 213.

[71] Frederic James, statistical Methods in Experimental Physics (World Scientific)